Remote Sensing of Drizzle Onset and Cloud Microphysical Properties in Marine Stratocumulus

Jasmine Rémillard

Doctor of Philosophy

Department of Atmospheric and Oceanic Sciences

McGill University

Montréal, Québec

December 2012

A thesis submitted to McGill University in partial fulfillment of the requirements of the degree of Doctor of Philosophy.

Acknowledgements

I would like to thank my supervisor, professor Pavlos Kollias, without whom this project wouldn't have been possible. His expertise in remote sensing and microphysics, and his vast network of acquaintances in the broad community of the atmospheric science were very helpful. Through enlightening discussions and stimulating ideas, this project was a great experience and a success. I especially appreciated his great patience and his unwavering support and understanding through life's ordeals.

I wish to extend my thanks to our various collaborators for their enthusiasm about the project and its results: Ed Luke for being so eager to share his own results and so quick to obtain them; Rob Wood for instigating the Azores field campaign that provided the main dataset for this project; and Christine Chiu for sharing her cloud optical depth time series with us and willingly reviewing her estimates for us.

Many thanks go to all the members of the cloud radar group, past and present, for their comments and support throughout the project. Special thanks go to Wanda Szyrmer for sharing her great knowledge of the microphysics and helping me with the modeling side of the project, and to Véronique Meunier for being my French buoy in this English world.

Discussions and comments from attendees of the various conferences I participated in, as well as the department's student seminars, were also greatly appreciated, providing an outside point of view that was sometimes much needed to refocus our work, placing it in a broader context.

The Ultimate community from McGill and the greater Montreal area provided an outlet for my sometimes overflowing energies, helping me stay focused and productive through all these years.

Finally, the unconditional encouragement from my family throughout these many years of hard work was very appreciated. Even when they could not understand what I was doing or why I was doing it, they were always there for me and willing to help in any way they could, despite the distance.

Funding was provided by the Fonds québécois de la recherche sur la nature et les technologies, the department of Atmospheric and Oceanic Sciences, McGill University, and the U.S. Department of Energy's Atmopheric Radiation Measurement program.

Statement of Originality

Most of the research done for this thesis makes use of data collected during the field campaign that took place in the Azores between April 2009 and December 2010. Using such a recent data set means that the collection of results presented here represents the fruits of some of the earliest work effort done with those data. In particular, an objective classification of radar observations into simple cloud and precipitation categories was missing in order to roughly identify periods of interest.

The deployment of a vertically pointing millimeter Doppler radar on a small island in the middle of the ocean permitted the study of vertical motions in marine stratocumulus clouds for the first time with such high resolutions. Moreover, the extension of the campaign over more than a year, with most instruments working together, allowed a seasonal cycle to emerge. Consequently, the results obtained for this thesis about the stratocumulus clouds in the Azores are unprecedented.

In addition, this thesis includes several aspects that are new contributions to the field of millimeter radar observations and studies. These can be summarized as follows:

- New theoretical relationships are introduced to relate the radar measurements to the microphysics and dynamics of the clouds. These relations include the effects of truncating the drop size distributions and of Gaussian turbulent motions, providing a theoretical reference to compare with.
- A Doppler spectra simulator is described for the first time. It is a forward model linking microphysical models' output back to the radar observations. It takes the size distributions as input to simulate what a particular millimeter radar would see under chosen dynamics and atmospheric

conditions. The characteristics of the radar system can be adjusted to test their effects on the hydrometeors detection.

- A sensitivity study is performed on the characteristics needed to detect the presence of early drizzle drops, which is unprecedented to the best of our knowledge. Two main characteristics of the Doppler radar measurements are examined: the signal-to-noise ratio, and the velocity resolution.
- The drizzle growth in maritime and continental stratocumulus clouds is investigated using a simple 1-D model and the Doppler spectra simulator. It emphasizes the possibilities of simple microphysical models to highlight the main processes responsible for the radar observations, as well as the learning process needed to improve models and our understanding of the atmosphere.
- Improvements are introduced to retrieve the cloud droplets' size distribution more accurately. A condensational growth model is added, with the assumption of steady-state supersaturation reached inside the cloud. This allows the retrieval of the three parameters of a lognormal size distribution, with two of them varying with height. The errors on the original measurements bring relatively small uncertainties on the retrieved parameters.
- The retrieval technique also presents a way to estimate the supersaturation at high temporal and spatial resolutions, which had not been achieved before. Even in situ measurements of that variable are rarely available, despite its important role in the droplets growth.

Contributions of Authors

The work presented in this thesis was carried out by myself, under the supervision of Pavlos Kollias, who played a normal supervisory role and edited the various manuscripts that make up this thesis. Other co-authors provided invaluable help and input as follows:

- Chapter 3 presents a paper published in the Journal of Climate, and co-authored by Pavlos Kollias, Edward Luke, and Robert Wood. The analysis was performed by me, based on existing methods. The presentation of some results was suggested by the co-authors, who provided editing comments on the original manuscript. The final, published version is included here, reflecting the suggestions and comments made on the original manuscript by three anonymous reviewers.
- Chapter 4 is based on a two-part paper published in the Journal of Geophysical Research by Pavlos Kollias, for which I am a co-author along with Edward Luke and Wanda Szyrmer. Only the portions where my contribution is relevant are included here. It introduces a forward simulator (originating from Pavlos Kollias, which I modified), as well as theoretical relations between the radar measurements and the cloud's dynamics and microphysics (that I developed). The cases were selected with Edward Luke, and the observations were investigated using a drizzle growth model (developed and ran by Wanda Szyrmer).
- Chapter 5 presents the manuscript to be submitted for publication. It is co-authored by Wanda Szyrmer and Pavlos Kollias. The new method described here was developed in collaboration with Wanda Szyrmer, and I performed the error analysis.

Abstract

Low-level stratiform clouds remain one of the wildcards in future climate simulations. Despite their important role in the earth's radiation budget and the large number of dedicated field campaigns, several cloud-scale processes in marine stratocumulus clouds remain misrepresented. The 19-month-long deployment of the Atmospheric Radiation Measurement Program Mobile Facility in the Azores provided the longest and most comprehensive ground-based observational dataset of marine boundary layer clouds to date.

The first objective of this project was the documentation of the frequency of occurrence of different cloud and precipitation systems in the Azores using a combination of passive and active measurements. The analysis indicates that, even though clouds were often observed (close to 80 % of the time), especially in the boundary layer (∼50 %), a single-layer stratocumulus coverage rarely persisted more than a day. In fact, many stratocumulus clouds were observed to have cumulus clouds underneath them. This is linked to the nearly constant decoupled state of the boundary layer in the Azores, contrary to what has been observed in the Pacific decks. 35 cases of mostly single-layer persisting stratocumulus coverage were selected for further analysis. Results include similarities with other studies (e.g., maximum coverage at night, thicker clouds needed to drizzle, and importance of cloud-top radiative cooling at night), as well as differences (e.g., coherent structures account for a smaller fraction of the updraft mass flux).

The second objective of this project was to revisit the detection of drizzle-size particles in stratocumulus clouds using radar observations. First, the cloud and drizzle size distributions are related theoretically to the radar measurements, including the effects of the dynamics. Then, a forward radar Doppler

spectra model was developed to test the sensitivity of the radar measurements to modifications of the drizzle contribution. Finally, a simple 1-D steady-state model was exploited to simulate drizzle growth as it falls in a cloud, using the forward model to link the output back to the radar observations. Using that combination of models, some observed features of the drizzle evolution inside continental and maritime stratocumulus clouds were successfully investigated. Overall, it was found that the skewness of a radar Doppler spectrum is a good indicator of the presence of early drizzle droplets, while a reflectivity or Doppler velocity threshold indicates the change in dominance in the Doppler spectrum occurring when drizzle is well developed.

The third and final objective of this project was to revisit another long-standing challenge: the retrieval of cloud microphysical properties using a combination of radar-radiometer measurements. A new technique was developed to retrieve the cloud particle size distribution in stratocumulus clouds, adding a microphysical condensational model under steady-state supersaturation conditions to a common retrieval method. The results appear reasonable in two nondrizzling marine stratocumulus clouds, and the derived cloud optical depth compares well with the one derived independently with another instrument. The errors of the retrievals were also estimated, demonstrating the added value of the new technique.

Abrégé

Les nuages stratiformes de basse altitude restent un des facteurs imprévisibles dans les simulations du climat futur. Malgré leur rôle important dans le budget radiatif terrestre et le grand nombre de campagnes de terrain dédiées, plusieurs procédés à l'échelle nuageuse dans les stratocumulus marins demeurent mal représentés. Le déploiement dans les Açores d'un laboratoire mobile du programme « Atmospheric Radiation Measurement » pendant 19 mois a fourni l'ensemble de données d'observation au sol sur les nuages de couche limite marine le plus long et le plus complet à ce jour.

Le premier objectif de ce projet fut la documentation de la fréquence d'apparition de différents systèmes de nuages et de précipitations dans les Açores en utilisant une combinaison de mesures passives et actives. L'analyse indique que, même si des nuages étaient souvent observés (près de 80 % du temps), en particulier dans la couche limite (∼50 %), une couverture de stratocumulus seul persistait rarement plus d'une journée. En fait, de nombreux stratocumulus furent observés avec des cumulus en dessous. Ceci est lié à l'état découplé de la couche limite quasi-constant dans les Açores, contrairement à ce qui a été observé dans les stratocumulus du Pacifique. 35 cas de couverture d'un stratocumulus persistant principalement seul furent sélectionnés pour une analyse approfondie. Les résultats incluent des similarités avec d'autres études (par exemple, une couverture maximale durant la nuit, un besoin de nuages plus épais pour bruiner et l'importance du refroidissement radiatif au haut des nuages durant la nuit), ainsi que des différences (par exemple, les structures cohérentes représentent une plus petite fraction du flux ascendant de masse).

Le deuxième objectif de ce projet fut de revisiter la détection des particules de bruine dans les stratocumulus en utilisant les observations radar. Tout

d'abord, les distributions de tailles des gouttelettes de nuage et de bruine sont liées théoriquement aux mesures radar, en incluant les effects dynamiques. Ensuite, un modèle direct de spectres Doppler radar fut développé pour tester la sensibilité des mesures radar à des modifications de la contribution de la bruine. Finalement, un simple modèle 1-D à l'état d'équilibre fut exploité pour simuler la croissance de la bruine pendant sa descente dans un nuage, en utilisant le modèle direct pour relier de nouveau les données sortantes avec les observations radar. En utilisant cette combinaison de modèles, quelques caractéristiques de l'évolution de la bruine observées à l'intérieur de nuages stratocumulus continental et maritime furent examinées avec succès. Dans l'ensemble, il fut déterminé que l'asymétrie d'un spectre Doppler radar est un bon indicateur de la présence de jeunes gouttelettes de bruine, alors qu'un seuil de réflectivité ou de vitesse Doppler indique le changement de domination dans le spectre Doppler se produisant quand la bruine est bien développée.

Le troisième et final objectif de ce projet fut de revisiter un autre défi de longue date : le recouvrement de propriétés microphysiques des nuages en utilisant une combinaison de mesures radar et radiométriques. Une nouvelle technique fut développée pour retrouver la distribution de tailles des particules nuageuses, en ajoutant un modèle microphysique de condensation dans des conditions de supersaturation en équilibre à une méthode populaire de recouvrement. Les résultats semblent raisonnables pour deux stratocumulus marins ne bruinant pas et la profondeur optique dérivée pour ces nuages se compare bien avec celle dérivée indépendamment avec un autre instrument. Les erreurs de recouvrement furent également estimées, démontrant la valeur ajoutée de la nouvelle technique.

Table of Contents

List of Tables

List of Figures

Chapter 1
Introduction

Marine stratocumulus clouds are ubiquitous over the eastern subtropical oceans (right panel of Fig. 1–1) and play a critical role in the boundary layer dynamics and the global climate (e.g., Klein and Hartmann, 1993; Bony and Dufresne, 2005). These prevailing low-level cloud decks are a key component in Earth's radiation budget (Randall et al., 1984; Ramanathan et al., 1989). Fig. 1–1 illustrates the tight connection between the stratocumulus presence over the subtropical oceans and the net cooling occurring there annually.

The radiative impact of marine boundary layer clouds depends on their macroscopic (e.g., horizontal extent, thickness) and microscopic properties (e.g., particle size distribution). Past studies have focused on the cloud macrostructure properties of marine boundary layer clouds and their relationship to large-scale dynamics and thermodynamic state using satellite observations and reanalysis products (e.g., Klein and Hartmann, 1993; de Szoeke and Xie, 2008). Wood and Bretherton (2006) have shown that approximately 80 % of

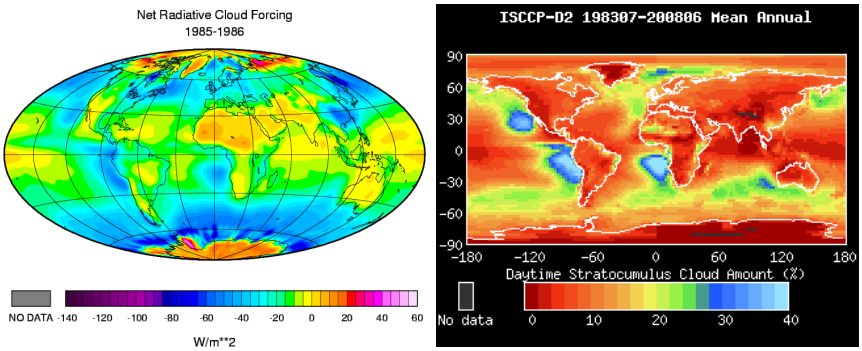

Figure 1–1: Annual mean of (left) the net cloud radiative forcing as obtained by the Earth Radiation Budget Experiment (ERBE) for 2 years, and (right) the global coverage of daytime stratocumulus clouds, as obtained by the International Satellite Cloud Climatology Project (ISCCP) over 15 years.

the variance in low cloud cover in regions dominated by marine stratocumulus clouds can be explained using the estimated strength of the inversion found at the top of the marine boundary layer. However, appreciable complexity and challenges are found on smaller space and time scales, including the cloud micro-scale (spatial scales of tens of meters and temporal scales of a few minutes or less).

If all other parameters are fixed, an increase in the aerosol concentration may reduce the cloud droplet sizes for a fixed liquid water content, and therefore increase the cloud optical thickness (the *Twomey effect*, Twomey, 1974). Reduced cloud droplet sizes can then lead to precipitation suppression and increase the cloud's lifetime (the *Albrecht effect*, Albrecht, 1989). However, recent modeling studies have suggested that elevated concentrations of cloud condensation nuclei can also affect entrainment of free tropospheric air in the marine boundary layer (e.g., Ackerman et al., 2004; Xue et al., 2008), thus leading to important feedbacks that include both key processes. The onset of precipitation is a critical mechanism that determines to a large extent the structure and optical properties of marine stratocumulus clouds, and thus their radiative feedbacks in future climate scenarios.

The parameterization of marine stratus clouds in global models is a challenge of current concern, particularly the representation of their drizzle production. Extensive sheets of stratus and stratocumulus clouds of varying radiative impact lie above the eastern boundary current upwelling regions over the world's oceans. Observations (e.g., Albrecht, 1989; Miller et al., 1998) and modeling studies (e.g., Albrecht, 1993; Wood, 2000) have shown that drizzle is important, principally because it is involved in determining the cloud's lifetime and evolution. Moreover, drizzle is frequently observed, especially over the open oceans, and even low precipitation rates can affect the stability of

the subcloud layer, which in turn impacts the evolution of the parent cloud (e.g., Nicholls, 1984; Wood, 2005a).

1.1 Shortcomings and New Additions

Warm rain microphysics are well understood: a cloud droplet grows by condensing water vapour onto a nucleus, drizzle first forms through collision and coalescence, subsequently growing further mainly by accreting other droplets. However, information about initial cloud properties are lacking to realistically simulate these processes in models. For instance, the degree of supersaturation reached inside the clouds determines the amount of water that condensates. On the other hand, the aerosol loading impacts the size reached by the particles through the competition it creates for the condensate. Similarly, the vertical air motion determines the growth time of the particles before they start to fall, while turbulence mixes volumes at various points in their development and increases the collisions probabilities. These quantities are challenging to obtain inside the clouds, even with in situ instruments. The role of cloud dynamics and turbulence is not well documented and is often used to explain discrepancies between observations and simulations. Moreover, the partitioning of liquid water to cloud and drizzle droplets at small scales and the quantitative assessment of the relative role of autoconversion and accretion in drizzle growth are not well understood.

Information about the cloud particles size distribution (PSD) is also lacking, despite numerous field campaigns and techniques development. In situ observations usually show that the cloud PSD can be approximated by an analytical shape, but the small range of sizes allows various shapes to apply. Physical and modeling arguments have been put forward in support of different shapes, but no consensus exists to our knowledge. Typically, distributions of the type lognormal (e.g., Clark, 1976; Gerber, 1996; vanZanten et al., 2005)

or gamma (e.g., Tampieri and Tomasi, 1976; Liu and Hallett, 1998; Cohard and Pinty, 2000) are chosen, but other functions of various complexity can also be found in the literature (exponential, power-law, delta, Khrgian-Mazin...). Consequently, studies often work with two possible shapes to cover more possibilities (e.g., Frisch et al., 1998; Miles et al., 2000; Geoffroy et al., 2010). Although in situ flights provide good images of the actual particles, their data sets are rather sparse and coarse due to the flight patterns. A more systematic way of obtaining the cloud PSD is needed to follow its evolution in the cloud towards drizzle production.

Stratocumulus clouds are a good place to test new methods to get such information, as they have a large coverage and time span. Their low heights also allow ground-based instruments to see them more accurately.

A big advantage of remote sensing over in situ sampling is the possibility to provide a continuous data set. In particular, millimeter radars received much of the attention due to their ability to fully sample the clouds, even during light precipitation events (see section 2.2 for more details on the instruments). However, only two dimensions are provided, the height and the time. On the other hand, conventional weather radars offer a three dimensional view of the system, with its evolution in time. Nevertheless, they are not sensitive enough to detect non-precipitating clouds. Therefore, scanning cloud radars are in development, although the attenuation suffered at these wavelengths is a challenge.

Previous work has been done to derive cloud and drizzle PSDs using a millimeter radar at the core of the retrieval. On the drizzle side, O'Connor et al. (2005) combined lidar and radar measurements to retrieve the drizzle PSD below the cloud base, while Frisch et al. (1995) developed a technique to retrieve the drizzle PSD within the cloud using only radar measurements. On

the cloud side, Frisch et al. (1998) developed a technique for the periods without drizzle-size particles, retrieving the profile of liquid water content (LWC) and a column number concentration. More recently, Martucci and O'Dowd (2011) implemented a method to retrieve warm cloud PSD using extrapolated lidar measurements.

1.2 Previous Field Experiments

Several field campaigns have been conducted to study clouds, with stratocumulus decks being the focus of a fair part (see Table 1–1 for a list of the main ones). These field studies advanced our knowledge of marine stratocumulus clouds, providing information on their boundary layer thermodynamic and cloud structure, as well as their diurnal cycle. They have highlighted that stratocumulus clouds can form under a diverse range of conditions, in both deep and shallow marine boundary layers, and under a wide range of aerosol loadings. Furthermore, the radiative properties of marine stratocumulus clouds and their propensity to drizzle depend on several factors including aerosols, liquid water path, and dynamics.

The most recent field campaign is the Clouds, Aerosol, and Precipitation in the Marine Boundary Layer (CAP-MBL). It took place from April 2009 to December 2010 in the Azores, to collect data on the physical and radiative properties of low-level clouds. Inter-annual variability had been previously recorded (repeating campaigns every year or so, as the Pan American Climate Studies Stratus cruises series), but no data set was yet available to sample the seasonal cycle. Moreover, it is the first data set to be obtained from a stable platform in the marine environment (island vs. ships and coastal regions). This has the advantage of simplifying the analysis of the data, although the island effects on the environment still remains to be investigated.

Table 1–1: List of the main field campaigns conducted to study the major marine stratocumulus decks, including the most recent one. They are grouped by region of interest: northeast Pacific (NE Pac), southeast Pacific (SE Pac), and northeast Atlantic (NE Atl). The possible platforms for the instruments are ships (S), aircrafts (A), or land (L).

Region	Campaign	Acronym	Observation period	Reference	Platforms
NE Pac	Dynamics and Chemistry of Marine Stratocumulus	DYCOMS	Jul–Aug 1985	Lenschow et al., 1988	A
	First ISCCP Regional Experiment–Marine stratocumulus Intensive Field Observations	FIRE marine-Sc IFO	Jun–Jul 1987	Albrecht et al., 1988	A-L
	Pan American Climate Studies–Tropical Eastern Pacific Process Study–stratocumulus region	PACS-TEPPS Sc region	Aug–Sep 1997	Yuter et al., 1999	S
	Second DYCOMS	DYCOMS-II	Jul 2001	Stevens et al., 2003	A
	Marine Stratus Radiation Aerosol and Drizzle	MASRAD	Mar–Sep 2005	—	A-L
	includes: Marine Stratus/stratocumulus Experiment	MASE	Jul 2005	Lu et al., 2007	A
	Second phase of MASE	MASE-II	Jul 2007	Lu et al., 2009	A
SE Pac	East Pacific Investigation of Climate–stratocumulus cruise	EPIC Sc cruise	Oct 2001	Bretherton et al., 2004	S
	PACS Stratus cruises	—	Nov 2003	Kollias et al., 2004	S
			Dec 2004	Serpetzoglou et al., 2008	S
			Oct 2005	—	S
			Oct 2006	—	S
			Oct–Nov 2007	de Szoeke et al., 2009	S
	Variability of the American Monsoon Systems (VAMOS) Ocean-Cloud-Atmosphere-Land Study	VOCALS	Oct–Nov 2008	Wood et al., 2011	S-A
NE Atl	Atlantic Stratocumulus Transition Experiment	ASTEX	Jun 1992	Albrecht et al., 1995	S-A-L
	Clouds, Aerosol, and Precipitation in the Marine Boundary Layer	CAP-MBL	Apr 2009–Dec 2010	—	A-L

Despite the emphasis given in past field campaigns to marine boundary layer clouds, the Azores campaign is unique compared to previous intensive field campaigns. First, the instrumentation deployed is far more comprehensive and superior to the one available in previous field studies. Second, the campaign is 21 months long and thus provides the opportunity to generate the long data set record required to sample a variety of aerosol, cloud and large-scale environmental conditions. Finally, to our knowledge, it is the first campaign that includes sophisticated millimeter radars (profiling and scanning) on a stable platform (island) that enables the use of the Doppler measurements and the utilization of the recorded Doppler spectrum, without the usual motion contamination from the ship/aircraft platform.

Therefore, the 21-month-long CAP-MBL campaign offers an excellent opportunity to carefully study many aspects from the micro-scale to the large-scale meteorology that impact drizzle initiation and production in marine stratocumulus clouds, using an innovative retrieval method that utilizes the radar Doppler spectra.

1.3 Objectives

The first objective of this work was to tackle the drizzle onset. In particular, emphasis was given to the identification of drizzle production in the cloud. This could then be useful to further study drizzle formation, such as how the liquid partitioning between cloud and drizzle is done and what factors are determinant in its occurrence. In turn, this will help modelers in their parameterization of the drizzle process.

To build on this, the second objective of this work was to tackle the cloud PSD, to learn more about its description. As mentioned earlier, there is a lack in this area, despite the many attempts to recover it from current observations.

If successful, this could be applied to more clouds, and teach us more about the aerosol effects and other unresolved issues.

This thesis is a collection of two papers and some additional work. To help bring everything together, a summary of the tools used throughout the work is first provided in chapter 2. Then, an identification of the clouds observed during the field campaign in the Azores is presented in chapter 3, to select periods characterized by a marine stratocumulus coverage. Chapter 4 investigates the detection of early drizzle formation using existing radar measurements, while chapter 5 tests a new approach to determine the cloud PSD. Finally, chapter 6 draws conclusions, and presents possible future directions for this work.

Chapter 2
Tools and Methods

Throughout the project, a number of instruments were used to study clouds occurrences and properties. This section contains a general description of these instruments, following a description of the two sites where their measurements were taken. A detailed description of models used will conclude the section.

2.1 Deployment Sites

In 1990, the U.S. Department of Energy's Office of Science established the Atmospheric Radiation Measurement program (ARM) to increase our understanding of how clouds affect atmospheric radiative fluxes, and to accordingly improve climate models (Ackerman and Stokes, 2003). Three fixed ARM Climate Research Facilities (ACRF) were established to cover the main climate regimes: one in the U.S. Southern Great Plains (SGP), one at the North Slope of Alaska (NSA), and one in the Tropical Western Pacific (TWP). To supplement these ground-based measurements, ACRF is managing an ARM Aerial Facility (AAF), and two ARM Mobile Facilities (AMFs). The AMF design allows deployment in any environment to support campaigns lasting at least six months, and includes a baseline suite of instruments similar to the ACRF as well as space for guest instruments specific to the campaign.

A subset of instruments from two of the ACRF sites were considered during this work: the SGP site, and the AMF deployment on Graciosa Island in the Azores (GRW).

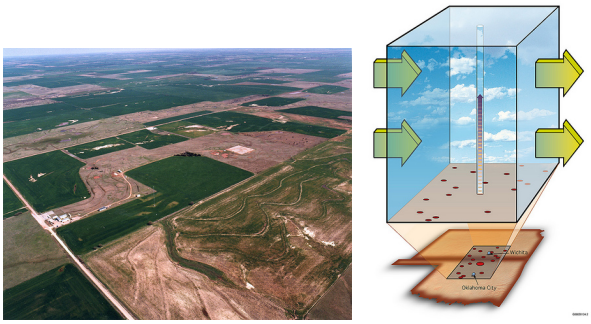

Figure 2–1: (left) Aerial view of the central facility of the SGP site, with its flat surroundings, looking south-east. (right) Schematic illustration of the SGP supersite. (Images courtesy of the ARM program.)

2.1.1 Fixed Site in the Southern Great Plains

The SGP site is located primarily in the north-central Oklahoma (see Fig. 2–1), ensuring a continental environment from the mid-latitude regime. It has numerous instruments arranged in clusters arrayed across approximately $143\,000\,\mathrm{km}^2$. A major draw for this area was its relatively homogeneous geography and easy accessibility. It experiences a wide variability of climate cloud types and surface flux properties, with large seasonal variations in temperature and specific humidity.

The site has been developed to represent a grid cell in global models, as depicted by the schematic illustration in Fig. 2–1. At its core, there is the central facility (located at the center of the grid cell), where most instruments are installed. Surrounding instrument clusters were deployed to capture the variability and reflect the conditions over the typical distribution of land uses within the site. The site operates since 1992, and intensive observation periods and guest instruments often supplement its main instruments' continuous measurements.

2.1.2 Mobile Facility on Graciosa Island

The first AMF was deployed on Graciosa Island to support the CAP-MBL campaign (see Fig. 2–2). This site was chosen since it is located in the region

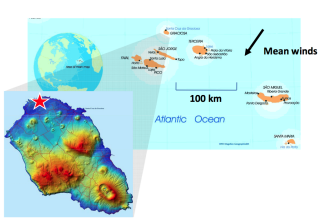

(a)

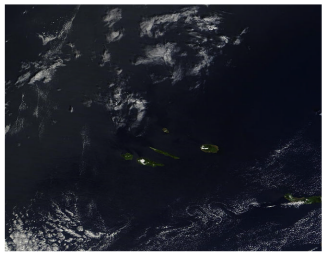

(b)

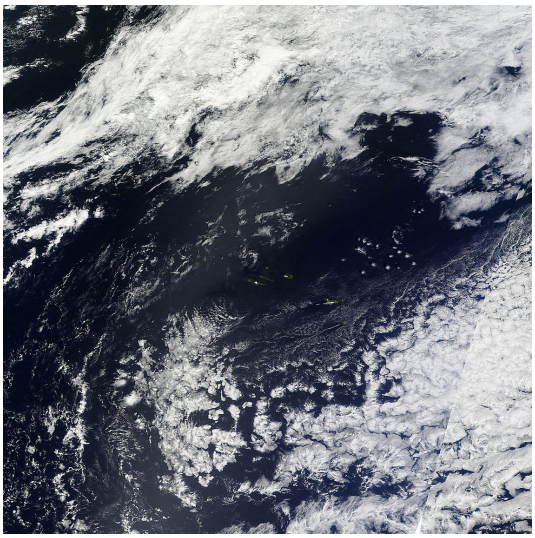

(c)

Figure 2–2: (a) Map showing the geographical situation of the Graciosa Island in the Azores, and its topography (inset; the maximum height is approximately 400 m). The red star indicates the approximate location of the GRW site. (courtesy of R. Wood, from University of Washington) (b) MODIS image zoomed on the Azores, and centered on GRW. (c) Same MODIS image centered on GRW, illustrating various cloud types that can affect the site.

experiencing the transition between stratocumulus conditions and trade-wind cumulus regime (observed in summer). Air masses of different origins can affect the atmospheric conditions, ranging from pristine clean conditions (Arctic plume) to highly urbanized polluted conditions (American plume), with diverse stages in between (North Canadian and European plumes). The diversity in air mass origin will introduce variable aerosol loading conditions. Also, Graciosa is the northernmost island in the center group of islands of the Azores archipelago, with relatively low topography (its highest point is just below 400 m). The prevailing winds are from a northerly direction, and the AMF was deployed near the north coast of the island, on a flat area near sea level (26 m above mean sea level). Thus, the possibilities for the island impacting the atmosphere are reduced.

Therefore, the GRW site provides a unique data set to study marine stratocumuli. Unlike most marine studies, the majority of instruments are ground-based instead of on ships or aircrafts, offering an easier analysis of the data (e.g., vertical velocities measurements are not affected by uncontrolled instrument movement, the measurements are continuous and always at the same location). Moreover, the deployment extended over 20 months (May 2009–December 2010), the longest to date, allowing the study of variability over timescales ranging from daily to seasonal, and increasing the chances of getting days that show the perfect situation for the study.

The CAP-MBL campaign results confirm that the Azores have the right mix of conditions to study how clouds, aerosols, and precipitation interact. Thus, the ACRF is implementing a new fixed site near the GRW site used for the AMF deployment during the campaign. The Eastern North Atlantic (ENA) site, as it will be identified, should be fully operational by the end of 2013.

2.2 Instruments

Although the measurements are taken from two different sites, the primary instruments used in this work fit into three categories of remote sensors: millimeter radars, lidars, and radiometers. These instruments form the minimal set deployed for a typical cloud study field work nowadays. They are described here in general terms, while further details of the exact instrument used are given later in the appropriate chapters.

2.2.1 Millimeter Radars

The main instrument for low-level cloud studies is the millimeter radar (e.g., Kollias et al., 2007b). It is often dubbed "cloud radar" due to its great sensitivity that allows it to detect cloud droplets. However, it is still more sensitive to precipitation particles. Nevertheless, attenuation from drizzle drops

is minor at millimeter wavelengths, allowing the signal to easily pass through light drizzle and fully sample the cloud itself. Furthermore, millimeter radars are usually characterized by a beam width narrow enough (half a degree or better) to provide high temporal and spatial resolutions. When operated in a profiling mode with Doppler capability, the primary measurement of a millimeter radar is the Doppler spectrum. It reports the full distribution of the return radar echo over the range of sampled Doppler velocities. Thus, detailed information about cloud microphysics and dynamics are inherent in such spectra (e.g., Luke et al., 2010; Kollias et al., 2011a).

Two millimeter radar frequencies are usually deployed at the ARM sites: 35 and 94 GHz. Those are windows between absorption peaks of the atmosphere. They correspond to wavelengths around 8.6 and 3.2 mm respectively. The 94 GHz signal is more prone to non-Rayleigh effects, but only in rain, which was not considered in this work. The lower frequency was chosen for the permanent zenith-pointing millimeter radar at SGP, while the higher frequency was chosen for the AMF millimeter radars.

2.2.2 Lidars (Ceilometers)

Since it is very challenging to distinguish between cloud and drizzle particles in a millimeter radar signal, an estimate of the cloud base location is sought elsewhere. Lidars are the instruments of choice to resolve that issue in clouds containing liquid droplets (hence their nickname "ceilometers").

Similarly to millimeter radars, most lidars are operated to provide profiles of the atmospheric column above them. As they use a signal in the visible end of the spectrum, the numerous cloud droplets found at a cloud base strongly attenuate the signal, often completely depleting it within 100 m. Therefore, the cloud base location is easily derived from a lidar profile when liquid droplets are present (typically with a 15-m accuracy). As well, measurements below

the cloud base remain unaffected, and the lidar provides information about precipitation and aerosols present under the cloud.

2.2.3 Microwave Radiometers

On the other hand, radiometers are passive remote sensors. Thus, profiling the atmosphere is much more challenging, and usually requires the use of many frequencies. Typically, microwave radiometers (MWRs) use only two channels: one near a water vapor absorption peak, and one away from it. For the work done here, typical Radiometrics MWRs detecting radiation near 23.8 and 31.4 GHz are used (Liljegren, 1994).

These MWRs are known for their ability to retrieve the integrated amount of water along their line of sight, separated into the vapor and liquid phases (respectively the precipitable water vapor [PWV] and liquid water path [LWP]). Such information can help constrain retrievals from other instruments, but also to correct the radar measurements for attenuation caused by the water in those phases. There are two main retrieval techniques used. The simple one has a statistical basis, and uses only the measurements at the two frequencies of the instrument. The second method physically constrains the retrievals using atmospheric models, and it requires measurements at three frequencies. The latter method is generally more accurate, but requires the presence of two MWRs. Now, 3-channel MWRs are being installed at most sites to simplify the retrievals. Here however, the physical retrieval is only used in one case study (see section 5.4.1), as it was not yet fully available.

2.2.4 Other Instruments

The 2-channel Narrow Field of View Zenith Radiometer (NFOV), deployed as part of the AMF on Graciosa Island, was used to compare the derived results of the retrieval technique developed in chapter 5. It was chosen as an independent source of information about the studied clouds. The NFOV

measures downwelling zenith radiance at two wavelengths (673 and 870 nm), at 1 s intervals. Chiu et al. (2006) developed an algorithm to retrieve the optical depth of the atmospheric column during daytime, using only these radiance measurements. It provides a time series similar to our retrievals, coming from a ground-based instrument looking at comparable sky samples.

When needed, the atmospheric state (pressure and temperature) is taken from the radiosondes. As balloons were launched every six hours, the measurements are interpolated to the radar time-height frame.

2.3 Models

To complement the analysis of the data, a modeling part was added. Two models are used in this work: one is a radar simulator, and the other is a microphysical model. The former was developed to link the drizzle growth simulated by the latter to the radar observations. A brief overview of these two models follows here, but more thorough descriptions are provided in chapter 4 (sections 4.3 and 4.5 respectively).

2.3.1 Doppler Spectra Simulator

A critical tool that we use in this work is an instrument simulator. Instrument simulators are forward models that transform numerical model output to the observation space, and thus offer an alternative to the typical parameterizations for comparing numerical model output and observations. Although not new, instrument forward simulators have recently received interest as a relatively new method to compare model output and observations. Here, a radar Doppler spectra simulator (DSS) was developed to emulate the measurements of millimeter radars under liquid water conditions.

The DSS is applicable to all millimeter radar systems of the ARM program and uses input from bin-microphysics, high-resolution numerical models and produces synthetic radar Doppler spectra. The input parameters to a

DSS are both microphysical (e.g., particle size, shape, phase, and number concentration) and dynamical (e.g., resolved wind components and sub-grid turbulent kinetic energy). Libraries for spherical and non-spherical particles are then used to compute the backscattering cross-section and fall velocities, while the turbulence is parameterized as a Gaussian function with a prescribed width that affects all particles in the same way. An assumed signal-to-noise ratio (SNR) is used to determine the amount of noise added throughout the spectrum, and the spectral smoothing due to spectral averages is included to reproduce the averaging realized by millimeter radars on successive returns. Thus, realistic Doppler spectra are obtained, and several parameters related to the morphological characteristics of the synthetically generated spectra are computed using the same algorithm used by ARM to develop their public output.

2.3.2 1-D Steady-State Microphysical Model

To further support the interpretation of the measurements, a simple one-dimensional drizzle growth model is used to simulate the growth of drizzle PSDs under stratocumulus conditions, in or out of the cloud. The model was greatly simplified to make runs quicker and easier to analyze. For instance, only one growth process is implemented in each run (e.g., accretion or evaporation), while others are either neglected or parameterized, depending on the situation.

A lognormal cloud PSD is assumed, with a prescribed width and total number concentration, and a characteristic size determined from the cloud LWC profile. Although these assumptions are crude, they are generally accepted in most microphysical retrievals. Moreover, the driving idea for this model is to see the effects of the drizzle growth on the spectra moments rather than the cloud impact. The shape of the initial drizzle PSD is also prescribed,

but can follow either a lognormal or a generalized gamma function. In the cloud, the formation rate of embryonic drizzle is used to estimate the drizzle total number concentration. This formation rate is dictated by the assumed cloud PSD and LWC profile at and above the considered level. The drizzle PSD subsequent evolution is then retrieved at given intervals of fallen distance, according to a general equation describing the process in play.

Inside the cloud, two accretion parameterizations can be used, based on different size-dependencies for the collection efficiency and the size-velocity relation. An evaporation parameterization is also present in the model, although it is not used here. A more detailed description of the two accretion processes is given in chapter 4, with a discussion of the errors introduced by the assumptions and their effects on the results.

Chapter 3
Marine Boundary Layer Cloud Observations in the Azores

The data set obtained by the AMF during its deployment in the Azores is relatively new, and has not been explored in great detail. Although we know that stratocumulus have been observed during the campaign by browsing randomly through the data, no objective and systematic analysis of the clouds have been done to help identify periods of interest. Therefore, this chapter is concerned with the identification of the presence of cloud and drizzle, and their classification into a few general cloud types, emphasizing on the low-level clouds. Several interesting cases of extensive stratocumulus coverage over the site has then been selected and used to study the behavior and characteristics of these marine clouds. The results are compared to those obtained in previous studies.

This chapter consists of the revised manuscript published in the Journal of Climate:

Rémillard, J., P. Kollias, E. Luke, and R. Wood, 2012: Marine boundary layer cloud observations in the Azores. *J. Climate*, **25**, 7381–7398, doi:10.1175/JCLI-D-11-00610.1.

Abstract

The recent deployment of the Atmospheric Radiation Measurement Program (ARM) Mobile Facility at Graciosa Island, Azores, in the context of the Clouds, Aerosol and Precipitation in the Marine Boundary Layer (CAP-MBL) field campaign added the most extensive (19 months) and comprehensive dataset of marine boundary layer (MBL) clouds to date. Cloud occurrence is high (60 %–80 %), with a summertime minimum. Liquid precipitation is frequently present (30 %–40 %), mainly in the form of virga. Boundary layer clouds are the most frequently observed cloud type (40 %–50 %) with a maximum of occurrence during the summer and fall months under the presence of anticyclonic conditions. Cumulus clouds are the most frequently occurring MBL cloud type (20 %) with cumulus under stratocumulus layers (10 %–30 %) and single-layer stratocumulus (0 %–10 %) following in frequency of occurrence. A stable transition layer in the subcloud layer is commonly observed (92 % of the soundings). Cumulus cloud bases and stratocumulus cloud tops correlate very well with the top of the transition layer and the inversion base, respectively. Drizzling stratocumulus layers are thicker (350–400 m) and have higher liquid water path (75–150 $\mathrm{g\,m^{-2}}$) than their nondrizzling counterparts (100–250 m and 30–75 $\mathrm{g\,m^{-2}}$, respectively). The variance of the vertical air motion is maximum near the cloud base and is higher at night. The updraft mass flux is around 0.17 $\mathrm{kg\,m^{-2}\,s^{-1}}$, with 40 %–60 % explained by coherent updraft structures. Despite a high frequency of stratocumulus clouds in the Azores, the MBL is almost never well mixed and is often cumulus coupled.

3.1 Introduction

Marine stratocumulus clouds are ubiquitous over the eastern subtropical oceans and play a critical role in the boundary layer dynamics and the global climate (e.g., Klein and Hartmann, 1993; Bony and Dufresne, 2005). These

prevailing low-level cloud decks are a key component in the earth's radiation budget (Randall et al., 1984; Ramanathan et al., 1989). The radiative impact of marine boundary layer clouds depends on their macroscopic (e.g., horizontal extent, thickness) and microscopic properties (e.g., particle size distribution). Past studies have focused on the cloud macrostructure properties of marine boundary layer clouds and their relationship to large-scale dynamics and thermodynamic state using satellite observations and reanalysis products (e.g., Klein and Hartmann, 1993; de Szoeke and Xie, 2008). Wood and Bretherton (2006) have shown that approximately 80 % of the variance in low cloud cover in regions dominated by marine stratocumulus is explained using the estimated inversion strength. However, appreciable complexity and challenges are found on smaller space and time scales, including the cloud microscale (spatial scales of tens of meters and temporal scales of a few minutes or less).

Previous field experiments focusing on marine stratocumulus clouds include the Atlantic Stratocumulus Transition Experiment (ASTEX) (Albrecht et al., 1995), the East Pacific Investigation of Climate (EPIC) (Bretherton et al., 2004), the Dynamics and Chemistry of Marine Stratocumulus (DYCOMS) (Stevens et al., 2003), and the Variability of the American Monsoon Systems (VAMOS) Ocean-Cloud-Atmosphere-Land Study Regional Experiment (VOCALS-REx) (Wood et al., 2011). These field studies advanced our knowledge of marine stratocumulus, providing information on their boundary layer thermodynamic and cloud structure, as well as their diurnal cycle. They have highlighted that stratocumulus clouds can form under a diverse range of conditions, in both deep and shallow marine boundary layers (MBL), and under a wide range of aerosol conditions. Furthermore, the radiative properties and propensity for drizzle from marine stratocumulus clouds depend on several factors including aerosols, liquid water path, and dynamics.

The aforementioned field campaigns are characterized by intensive observation periods limited in time from a couple of weeks to a month. Thus, previous studies have not been carried out long enough to provide a useful climatology of key MBL and associated cloud properties. The recent Clouds, Aerosol and Precipitation in the Marine Boundary Layer (CAP-MBL) field campaign (`www.arm.gov/sites/amf/grw/`), which took place in the Azores, nicely filled that gap. As part of the campaign, the U.S. Department of Energy Atmospheric Radiation Measurement Program (ARM) Mobile Facility (AMF) was deployed on Graciosa Island. This AMF deployment is unique compared to previous intensive field campaigns. First, the AMF instrumentation is far more comprehensive and superior to that available in previous ground-based field studies. Second, the campaign is 21 months long and thus provides the opportunity to generate the long dataset record required to sample a variety of aerosol, cloud, and large-scale environmental conditions. Finally, it is the first marine stratocumulus field campaign with sophisticated cloud radars (profiling and scanning) on a stable (island) platform that enables the use of the Doppler velocity measurements. Thus, the AMF deployment in the Azores produced the most comprehensive data set of MBL clouds to date.

In this study, we select a subset of the deployed AMF instruments to study the observed MBL clouds in more detail. An objective scheme was first developed to identify their occurrence across the entire dataset, and to recognize some important subtypes (e.g., cumulus and stratocumulus), with the presence of precipitation also diagnosed (see section 3.3). The variability and frequency of occurrence of the different cloud and precipitation events is presented with emphasis on the various MBL cloud structures. A further analysis of the MBL emphasizes the differentiation between cumulus and stratocumulus regimes as well as the presence of decoupling. A statistical analysis

of cloud structural and dynamical properties is performed and related to the thermodynamic profiles.

3.2 Observations

The CAP-MBL field campaign lasted 21 months (April 2009–December 2010), permitting the sampling of almost two full years of cloud and precipitation conditions in the Azores. Although this location has been used in the past for the study of marine stratocumulus clouds (ASTEX), a variety of cloud conditions were sampled which include shallow cumulus, cumulus under stratocumulus, deeper convection, and frontal systems. The AMF—with its usual comprehensive array of aerosol, cloud, precipitation, and radiation sensors—was deployed near the north shore of Graciosa Island (39.09°N, 28.03°W, 26 m MSL). This location is upwind for the climatologically prevailing wind conditions in the MBL and was selected to reduce the island effect. The primary instruments used in this study to describe the cloud and precipitation conditions are 1) a W-band (95-GHz) Doppler radar, 2) a laser ceilometer, 3) a two-channel microwave radiometer (MWR), and 4) radiosondes (four per day). The instruments were placed within a few meters of each other; thus, to the extent possible, their measurements describe the same atmospheric column. The operational status of the three remote sensors is summarized in Fig. 3–1, allowing gaps of up to one minute to be considered within normal operation. Overall, the observations are fairly continuous with great overlap between the three remote sensors, spatially as well as temporally.

3.2.1 W-band Doppler Radar

A baseline instrument of the AMF is the W-band ARM Cloud Radar (WACR) (Mead and Widener, 2005), a 95-GHz vertically pointing Doppler radar. Millimeter wavelength radars are ideally suited for the study of MBL clouds (e.g., Kollias et al., 2007b). Owing to its short wavelength (3.15 mm),

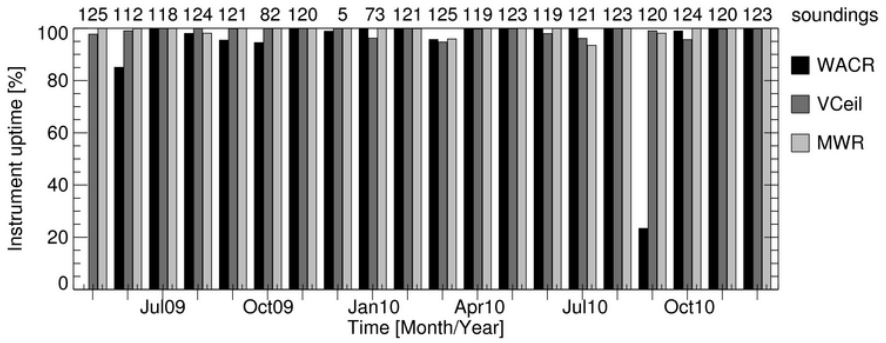

Figure 3–1: Monthly statistics of good running time for the WACR (black), ceilometer (dark gray), and MWR (light gray). Operations are considered bad when more than a minute separates successive measurements. Note that the radar started working in early June 2009, and it was down for about 23 days in September 2010. Note also that the radiometer measurements from 11 Jul through 9 Aug 2010 are unreliable, owing to a software problem, although it is not shown here. The numbers above the graph represent the number of soundings taken during each month that returned good measurements.

it is sensitive enough to detect cloud droplets ($-50\,\mathrm{dBZ}$ at $2\,\mathrm{km}$), while attenuation is small in light to moderate drizzle conditions. Furthermore, it uses a beam width narrow enough (0.19°) to provide high temporal and spatial resolutions (respectively around $2\,\mathrm{s}$ and $43\,\mathrm{m}$). Its primary measurement is the Doppler spectrum, reporting the full distribution of the returned radar echo over the range of sampled Doppler velocities (here $\pm 7.885\,\mathrm{m\,s^{-1}}$ with a resolution near $6\,\mathrm{cm\,s^{-1}}$). Thus, detailed information about cloud microphysics and dynamics are inherent in the radar measurements (e.g., Luke et al., 2010; Kollias et al., 2011a). The WACR also provides an estimate of hydrometeor (i.e., cloud and drizzle) boundaries (see section 3.3.1 below), as it is only sensitive to these atmospheric particles. However, some parts of nonprecipitating liquid clouds might be missed if the cloud droplets are not large enough, and heavy precipitation strongly attenuates the signal affecting the cloud top measurements. For the Azores deployment, the WACR began operating on the morning of 5 June 2009 and operated until the end of the campaign. One major interruption occurred in September 2010, when the radar was down

for almost 23 days, due to a hard disk problem. Otherwise, the radar experienced six downtimes of more than an hour (including three extending over about 1.5 days) and a few shorter, for a total of less than 10 % of a month (see Fig. 3–1, black bars). Note also that the radar used alternating copolarized (H-H) and cross-polarized (H-V) operating modes through late 2009, after which it operated continuously in copolarized mode. The cross-polarized measurements are not used here since MBL clouds have spherical cloud and drizzle particles. Therefore, the time between profiles is around 4 s for the earlier months, and 2 s for the latter. Nonetheless, given the horizontal scales of the sampled clouds the results should not be affected by that change.

3.2.2 Ceilometer

Another baseline AMF instrument is a Vaisala ceilometer (CT25K model, upgraded in mid July 2010 to the CL31 model; Münkel et al., 2007), a near-infrared vertically pointing lidar. It provides profiles of the atmospheric column, sensing aerosols and hydrometeors mainly up to the liquid cloud base, as cloud droplets prevent in-cloud measurements by extinguishing the laser signal. Nevertheless, the sharp increase and subsequent decrease of the lidar backscatter at the level of the cloud base is very useful for deriving the actual cloud base height, while still being able to profile drizzle and aerosols particles under the cloud (e.g., O'Connor et al., 2005; Markowicz et al., 2008). Although up to three liquid layer bases are reported in the ceilometer products, usually only the first one is reliable. This is due to the quick depletion of the lidar signal strength by the numerous cloud droplets, and it depends on the amount of liquid encountered in lower cloud layers. The ceilometer's temporal resolution was around 15 s for this deployment, which is slightly coarser than for the WACR. Here, it is assumed that each reported base height is representative of the whole 15 s. The ceilometer range resolution is 15 m. Thus, the analysis is

done using the original WACR temporal grid, maintaining the high sampling rate of the WACR. The ceilometer was deployed for the whole duration of the campaign. It only experienced 12 downtimes lasting more than an hour (including three covering more than a day), as well as a small number of shorter interruptions (see the dark bars in Fig. 3–1).

3.2.3 Microwave Radiometer

A standard Radiometrics 2-channel microwave radiometer (MWR) was also present throughout the campaign. This instrument passively measures the amount of radiation emitted by the atmosphere at two frequencies (23.8 and 31.4 GHz) to retrieve the amount of integrated water in the atmospheric column overhead, separated into the vapor and liquid phases [the precipitable water vapor (PWV) and liquid water path (LWP); e.g., Liljegren, 1994]. Such information can help constrain retrievals from other instruments, such as the WACR. The MWR time resolution is around 30 s, which is also coarser than for the WACR. Nevertheless, as the MWR measurements actually come from 20-s signal dwells, it is reasonable to consider each retrieved quantity to be representative of the whole 30 s. Therefore, these measurements are oversampled to match the high temporal resolution of the WACR when required by the analysis. The root-mean-squared accuracy of the LWP retrieval is around 20–25 $\mathrm{g\,m^{-2}}$. As with the ceilometer, the MWR was deployed for the whole campaign, and it worked continuously without much interruption of data (see Fig. 3–1, light bars). However, the MWR experienced a processing problem in the second summer, rendering the measurements reported from 11 July through 9 August 2010 unreliable (not shown in Fig. 3–1 as measurements are available nevertheless). Note also that the presence of water on the instrument's window contaminates the measurements, rendering its retrievals unreliable. This happens anytime precipitation reaches the ground.

3.2.4 Radiosondes

Regular radiosonde launches (every 6 h) were performed throughout the deployment to characterize the thermodynamic state of the atmosphere, as well as the wind speed and direction. The radiosondes collect measurements every 2 s during their ascent, providing a typical vertical resolution of 10 m in the troposphere (depending on the conditions at the launch time). These measurements can only be interpolated to the WACR time steps with limited confidence, owing to the coarse temporal resolution of the radiosondes. However, some statistics can still be determined around the balloon launch times, since there are 20 months of data comprising more than 2200 atmospheric profiles, although no sondes were launched in the last third of October 2009, nor from 2 December 2009 through 12 January 2010 (see the numbers at the top of Fig. 3–1).

3.3 Methodology

All instruments described in the previous section have certain skill for detecting the presence of clouds in the overlaying atmospheric column. For instance, relative humidity profiles taken by a radiosonde have been used in the past to provide estimates of cloud layer locations (e.g., Wang and Rossow, 1995). However, their temporal resolution is too coarse to form robust statistics of cloud occurrence, especially in the MBL, where clouds are typically very thin. The MWR is sensitive to the presence of liquid in the column, and measurements above its theoretical sensitivity (30–50 $\mathrm{g\,m^{-2}}$) can be used to infer the occurrence of liquid clouds. However, the MWR misses all ice clouds (mostly cirrus clouds in the Azores), as their thermal emission is negligible at the frequencies sensed by the MWR (Ulaby et al., 1981). Similarly, the ceilometer measurements are very sensitive to the presence of cloud droplets, providing a good estimate of the base height of liquid clouds; its backscatter

profiles can be used to find ice cloud too (e.g., Liu et al., 2009). Nevertheless, it still misses most high clouds, as its useful range stops near 7.5 km. Finally, the WACR is sensitive to most hydrometeors and profiles all clouds in the troposphere, unless strong precipitation occurs and causes too much attenuation (Lhermitte, 1990). However, it cannot easily differentiate precipitation from cloud particles (so cannot be used to reliably provide cloud base estimates in drizzling conditions) and lacks sensitivity to very thin liquid clouds (less than 100 m thick).

Here, a multi-instrument approach that utilizes synergistic measurements from all sensors is used to describe the cloud and precipitation conditions during CAP-MBL. Because of the focus on describing the vertical structure of clouds and precipitation, only the active remote sensor (radar and lidar) measurements are used for the cloud and precipitation occurrence statistics, while the MWR and the soundings are used as additional classification variables. The approach is not new: the cloud radar and lidar are complementary instruments often used to derive cloud and precipitation statistics (e.g., Intrieri et al., 2002; Bretherton et al., 2004; Kollias et al., 2007c; Illingworth et al., 2007).

Using the raw WACR measurements [radar reflectivity and signal-to-noise ratio (SNR)] the radar range gates that contain significant returns from atmospheric targets (e.g., hydrometeors) are identified to develop the radar-detected hydrometeor mask. The large number of WACR integrated radar pulses ($\sim$20 000 collected in 2-s signal dwell and a WACR pulse repetition frequency of 10 kHz) enables it to detect very low signal to noise radar returns in the boundary layer (WACR sensitivity of -56 dBZ at 1 km). The significant detection WACR hydrometeor mask is based on Clothiaux et al. (1995), and

a two-dimensional (time-height) filter is used to remove isolated radar pixels. The WACR-derived hydrometeor mask is used to estimate the number of hydrometeor layers in the atmospheric column and their corresponding boundaries. The WACR-derived hydrometeor layer base is not necessarily the cloud base since the WACR cannot differentiate between cloud and precipitation particles below the cloud base. Thus, the radar-derived hydrometeor mask is combined with the ceilometer-generated time series of cloud-base heights. Although the ceilometer detects drizzle too, its measurements are more sensitive to the numerous small liquid cloud droplets encountered by the laser at the cloud base and thus are systematically used to derive the liquid cloud base, at least for the first cloud layer. As formerly observed (e.g., Comstock et al., 2004; Wood et al., 2011), heavy drizzle often gives false signals, by significantly lowering the ceilometer-derived cloud-base height. During heavy precipitation, the cloud identification will still be reliable, but further analysis of MBL clouds would be compromised. Thus, the profiles containing intense precipitation (defined below) are removed prior to subsequent analysis.

The WACR/ceilometer detections agree very well in the MBL; however, the possibility of underestimating the hydrometeor occurrence at high altitude should be considered since the ceilometer is not capable of detecting high clouds and the radar sensitivity is degraded. The WACR moments, the radar-derived hydrometeor mask, and the ceilometer-derived liquid cloud base are inputs to the cloud and precipitation type identification scheme described in the following section.

3.3.1 Cloud and Precipitation Type Identification

A WACR echo is classified as precipitation if it is detected below the ceilometer cloud-base height. The first category of precipitation is virga, defined as precipitation that does not reach the lowest WACR range gate (i.e.,

Table 3–1: List of liquid precipitation types and their main characteristics used to differentiate them.

	Type		
	Virga	Light	Intense
Echo base	$> 200\,\mathrm{m}$	$< 200\,\mathrm{m}$	$< 200\,\mathrm{m}$
Base reflectivity	—	$< 0\,\mathrm{dBZ}$	$\geq 0\,\mathrm{dBZ}$
Echo below cloud base	Yes	Yes	Possible

no significant radar return at its lowest range gate, around 170 m AGL; see Table 3–1). In cases where the WACR echoes reach the lowest range gate (here taken as a proxy for the surface) two more precipitation categories are identified: light and intense. The separation between these two precipitation types is based on a near-surface (200 m) radar reflectivity threshold of 0 dBZ. Anytime that the WACR lowest gate echoes have a reflectivity above 0 dBZ, intense precipitation is designated, regardless of the ceilometer cloud-base height since the ceilometer measurements are significantly affected by the presence of water on its lens cover. The use of a radar reflectivity threshold is justified given the absence of disdrometer measurements in the Azores. Furthermore, the MBL clouds produce drizzle echoes below 0 dBZ; thus, the intense category of precipitation is almost exclusively related to deeper cloud systems (e.g., frontal precipitation). The distinction between virga and light precipitation provides a qualitative indicator of the drizzle intensity and indicates the portion of the subcloud layer that was affected by evaporation.

Using the WACR-derived hydrometeor mask and the ceilometer-derived cloud bases, groups of connected pixels containing hydrometeors are identified. Each of these hydrometeor clusters is individually analyzed on an hourly basis, with the hydrometeor layer base (top) defined as the 5th (95th) percentile of the hourly distribution of the cloud cluster base (top). Based on

their hourly-derived base and top height extrema and the available ceilometer-derived cloud-base height, several cloud types are identified (columns in Table 3–2). The hourly clusters are first separated into four types based specifically on these boundary definitions: 1) high cloud if the base is above 7 km; 2) middle cloud if the base is above 3 km; 3) low cloud if the top is below 3 km; and 4) deep boundary layer cloud if the base is below 3 km but the top is above 3 km. Note that the last category contains mostly frontal clouds, such as nimbostratus and cumulonimbus. Since the focus of this study is MBL clouds, emphasis is placed on low clouds, where the radar and lidar are most sensitive, allowing for well-defined cloud boundaries. As a result, low clouds are further divided into three subtypes: broken, stratocumulus, and indeterminate. The temporal duration of a hydrometeor cluster is used to differentiate broken cloud conditions (shallow cumulus) from stratiform cloud conditions, while stratocumulus are also required to have a narrow hourly cloud-top height distribution (less than 100-m standard deviation). Examples of stratiform and broken MBL cloud conditions as seen by the WACR and Moderate Resolution Imaging Spectroradiometer (MODIS) are shown in Fig. 3–2. The remaining low cloud hourly clusters make up the third subtype (referred to as indeterminate hereafter). Each cloud type has an expected precipitation type (last row of Table 3–2), although others are also possible. Note that the lidar measurements rarely reach high clouds, and thus no precipitation shaft is expected. Note also that the cloud types are not all mutually exclusive since clouds are observed only in time and height, yet they are also evolving in the two horizontal dimensions.

The cloud and precipitation identification scheme is applied each day when both the WACR and ceilometer were operational, and statistics about cloud and precipitation occurrences are computed on hourly and daily basis, with

Table 3–2: List of cloud types and their main characteristics used to differentiate them in the identification algorithm (Ind: indeterminate). The last row indicates the type of precipitation most likely associated with each cloud type.

	Type					
			Low			
Characteristic	High	Middle	Cu	Sc	Ind	Deep BL
Cloud base	$> 7\,$km	$> 3\,$km	—	—	—	$\leq 3\,$km
Cloud top	—	—	$\leq 3\,$km	$\leq 3\,$km	$\leq 3\,$km	$> 3\,$km
Duration	—	—	$<$20 min	$\geq$20 min	$\geq$20 min	—
CT variability	—	—	—	$< 100\,$m	$\geq 100\,$m	—
Type of precipitation	—	Virga	Virga	Light	Intense	Intense

the daily results composited together to form monthly statistics. Note that the hourly derived boundaries extrema are only used to identify the cloud types. Further analysis makes use of the full distribution of the hourly cloud base and top heights to provide their statistics. Finally, the occurrences of cumulus clouds under a stratocumulus cover are investigated. These represent the WMO-defined low cloud type CL8 and are diagnosed on an hourly basis. When both types are detected in any number of profiles within an hour, all profiles having cumulus and/or stratocumulus clouds within that same hour are included in the Sc + Cu category.

3.3.2 Radiosonde Analysis

Radiosonde data are not used directly in cloud identification but are used to determine the thermodynamic structure of the lower atmosphere during certain cloud conditions. For instance, the inversion often associated with the top of the MBL is easily detected in sounding profiles. A temperature increase with height somewhere between 500 m (to avoid surface effects) and 3 km (to remain in the MBL) denotes the presence of an inversion. The level of maximum increase indicates the inversion layer location and it includes all levels

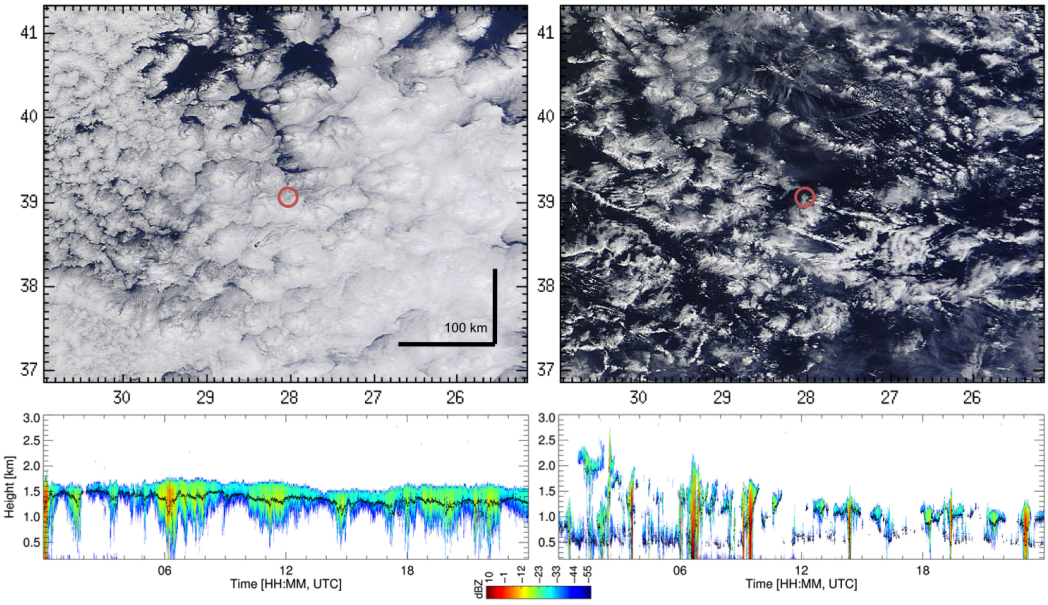

Figure 3–2: (top) True color images from MODIS onboard *Terra* taken around 1315 UTC and spanning about 500 km in both dimensions centered at the location of Graciosa Island (shown in red circle). (left) A stratocumulus cloud case (22 Nov 2009) and (right) a broken cumulus (0300–0600 UTC) and cumulus with stratocumulus (1800–2400 UTC) cases (30 Aug 2010). (bottom) The corresponding daily WACR time-height reflectivity observations with the first ceilometer cloud base shown as black dots.

around it still characterized by an increase. Since wetting affects the temperature measurements above clouds (Caldwell et al., 2005), a loose criterion on the water vapor mixing ratio (r) was added by requiring its decrease with height.

Many studies have also mentioned the presence of a transition layer in the MBL, which separates a surface mixed layer from the cloud-containing layer aloft (Augstein et al., 1974; Garstang and Betts, 1974; Yin and Albrecht, 2000). It is mainly characterized by a sharp decrease of moisture with height, accompanied by a slight increase in temperature. It indicates the presence of decoupling conditions that can lead to a cutoff of the upper part of the MBL from its moisture supply, thus controlling low-level cloudiness. Cumulus clouds often form near its top, as the surface lifting condensation level often

falls within the transition layer (Yin and Albrecht, 2000). Following Yin and Albrecht, the presence of a transition layer will be investigated using their parameter μ, which combines the potential temperature θ and mixing ratio r gradients with respect to the pressure p in the following way:

$$\mu = -\left(\frac{\partial\theta}{\partial p} - \frac{0.608\theta}{1 + 0.608r}\frac{\partial r}{\partial p}\right).$$

Its mean value is computed using all levels below the inversion. Then, if the maximum value of μ in those levels is positive and greater than 1.3 times the mean (based on Yin and Albrecht, 2000), a transition layer is present. The transition layer includes all levels around the μ maximum that satisfy this criterion.

As the detection of these two layers depends on the derivative of the measured variables, a 1-2-1 smoother is applied prior to any analysis. This step removes most of the small-scale variability that might be caused by sampling errors (although the data were already smoothed by the radiosonde software itself) and provides smooth local gradients. Also, when averaging various profiles together, a layer-by-layer procedure is used to preserve the character of the transition and inversion layers [based on Augstein et al. (1974) and Yin and Albrecht (2000)]. For each sounding, five layers are defined: below the transition base, the transition layer, from the transition top to the inversion base, the inversion layer, and above the inversion top (up to 3 km). Each layer is averaged separately using a relative height coordinate (from 0 to 1). The averaged sounding is then obtained by combining the five resulting averaged layers, using the averaged base and top heights of the layers to get the height coordinate.

The lower tropospheric stability (LTS) is also used in this study. Based on Klein and Hartmann (1993), it is defined as the difference in potential

temperature between 700 mb and the surface. Finally, any interpolated (or averaged) wind direction is obtained from the two interpolated (or averaged) components of the wind vector.

3.3.3 Turbulence and Mass Flux Measurements

During nonprecipitating cloud conditions, the WACR Doppler velocity measurements are used to derive turbulence statistics in low-level stratiform cloud conditions. This is based on the assumption that liquid cloud particles have negligible terminal velocity and inertia and, thus, act as tracers of the vertical air motion (e.g., Kollias et al., 2001). Only stratocumulus periods without drizzle detected under the ceilometer base are considered in these statistics, in order to remove most bias caused by the larger precipitating particles. The WACR Doppler velocity measurements are used to estimate the hourly estimates of the mean, variance and skewness of the vertical air motion. Using the vertical air motion measurements, mass flux statistics are also estimated during nonprecipitating stratocumulus conditions to reduce any correlations between drop fall velocities and WACR Doppler measurements. Although Kollias et al. (2011b) showed that drizzle drops are ubiquitous in marine stratocumulus clouds, their impact on the velocity moments remains negligible in nondrizzling parts.

Using the high-resolution in-cloud vertical velocity measurements, the mass flux profiles are derived using two conditional sampling strategies (based on Kollias and Albrecht, 2000). They are both based on the WACR perturbed velocities, which are obtained by removing the hourly mean from the velocity measurements. The first method (a classic direct sampling) simply uses the sign of these perturbed velocities to determine the presence of updraft and downdraft regions. The second method (the coherent sampling) refines this by using the cloud's coherent structures only. Those structures are pockets of

clouds that move together on average. Coherent structures must be observed in both dimensions: the perturbed vertical velocity must conserve its sign for three or more successive profiles (time dimension, which relates to the horizontal dimension) and over at least four successive gates (i.e., about 170 m in the vertical dimension). Both methods directly retrieve the fractional updraft area (σ) and the updraft and downdraft velocities (w_u and w_d), with the second one providing the contribution from the coherent structures. The convective mass flux (M_c) can then be computed from the following: $M_c = \rho\sigma(1-\sigma)(w_u - w_d)$, where ρ is the air density.

The mass flux profiles are also computed using the turbulence statistics as proposed by Randall et al. (1992). This method relates σ and M_c to turbulence statistics. It uses a "top hat" representation of the updrafts and downdrafts properties to express σ, w_u, and w_d as functions of the first three moments of the vertical velocity (mean $\overline{w}$, variance $\overline{w'^2}$, and skewness S_w):

$$\sigma = \frac{1}{2} - \frac{S_w}{2\sqrt{4 + S_w^2}},$$

$$w_u = \overline{w} + \frac{\sqrt{\overline{w'^2}}}{2}\left(\sqrt{4 + S_w^2} + S_w\right),$$

$$w_d = \overline{w} - \frac{\sqrt{\overline{w'^2}}}{2}\left(\sqrt{4 + S_w^2} - S_w\right).$$

Then, the relationship for the convective mass flux depends only on the variance and skewness of the vertical velocity:

$$M_c = \frac{\rho\sqrt{\overline{w'^2}}}{\sqrt{4 + S_w^2}},$$

[for the complete derivation of the equations, see Randall et al. (1992)]. In the following results, the mass flux values are normalized by ρ. The application of the Randall et al. approach to estimate the fractional area of the updrafts and the updraft mass flux and its comparison with the direct and coherent methods

are used as a qualitative indicator of how close to the top-hat representation of updrafts and downdrafts the observed vertical air motion is. Furthermore, it is an indicator of how well high-order closure models can be used to determine the area and mass flux of updrafts.

3.4 Results

3.4.1 Cloud and Liquid Precipitation Occurrence

Using the radar-lidar synergistic observations, the monthly fraction of time hydrometeors were detected in the atmospheric column is shown in Fig. 3–3a. A weak seasonal cycle is observed with minimum (60 %–70 %) during the summer and early fall and maximum (80 %) during the winter and spring season. Liquid precipitation is detected almost 50 % of the time that we have hydrometeors in the atmospheric column and exhibits a similar weak seasonal cycle. A breakdown of the observed cloud occurrence into the four main cloud types (described in section 3.3.1) is shown in Fig. 3–3b. Note that the sum of these cloud type occurrences is likely greater than (rather than equal to) the overall cloud occurrences shown in Fig. 3–3a since more than one cloud type can be present in the atmospheric column at the same time. Low-level clouds are the dominant observed cloud type, with 40 %–60 % occurrence maximizing in the summer and fall seasons. The seasonal cycle of low cloud occurrence anti-correlates with the observed seasonal cycle of all the other cloud types, which peaks during the winter and spring seasons (Fig. 3–3b), consistent with the presence of the subtropical high pressure system during the summer and fall seasons that favors MBL cloud occurrence through the development of low-tropospheric stability and moisture trapping in the low levels. This system is strongest in summertime, when midlatitude storm tracks are at their most poleward, and with its center closer to the site (Hasanean, 2004), explaining the seasonal cycle observed, as proposed by Norris and Klein (2000). A local

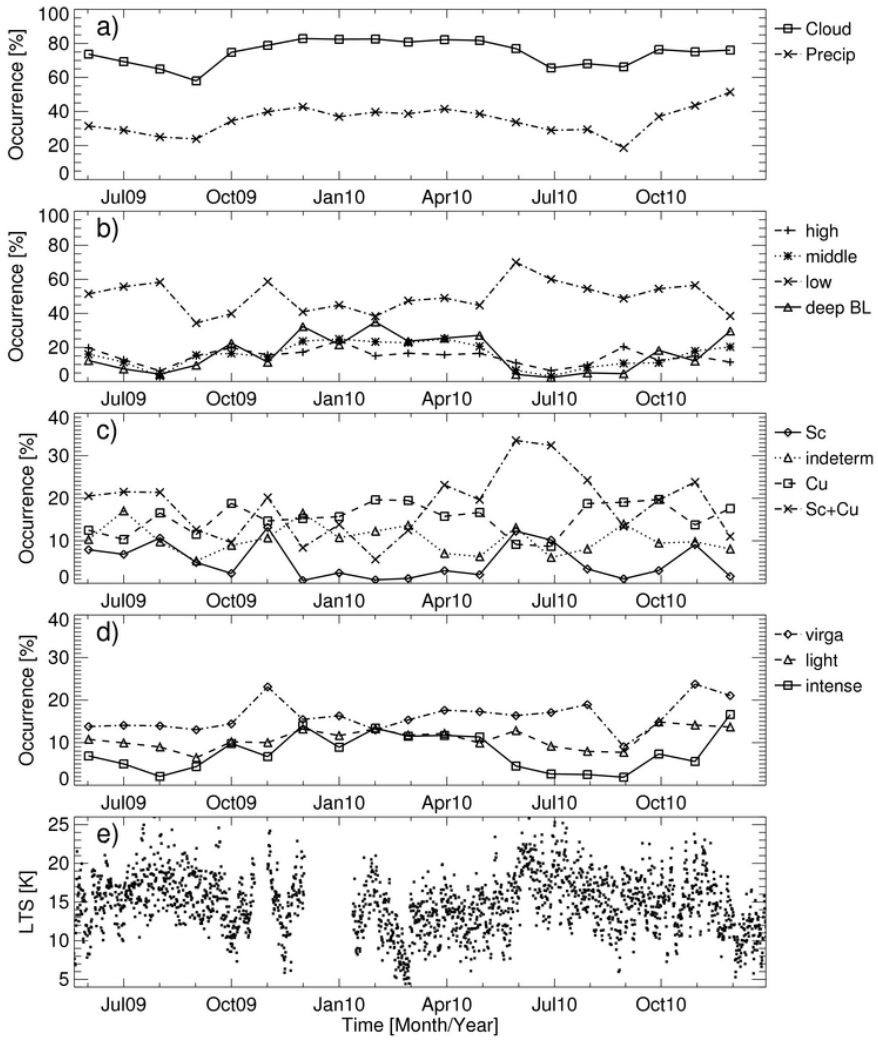

Figure 3–3: Monthly statistics of (a) cloud and liquid precipitation coverage using the lidar-radar algorithm, (b) the four main cloud types, (c) low-level clouds, and (d) liquid precipitation types. Note that the September 2010 results come from only 8 days due to a radar downtime. Also note that the precipitation reported here relates to the first cloud layer only. (e) Time series of LTS as retrieved from the radiosondes launches.

minimum in the low cloud occurrence is noticeable in the early fall of 2009 (a corresponding 2010 event is unconfirmed due to the radar failure in September 2010). This divergence could be a simple manifestation of interannual variability, experiencing more midlatitude systems than normal. A longer time series is needed to verify this feature.

Additional insights on the seasonal cycle of low-level clouds are provided through their breakdown into different subtypes (see Fig. 3–3c). Shallow cumulus clouds are the most frequently observed MBL cloud type with a monthly occurrence of 20 % and weak month-to-month variability during the summer. Monthly increases in Sc + Cu coverage appear to compensate for decreases in the Cu cloud fraction. Indeed, this MBL cloud structure is also frequently observed, with maximum occurrences during the summer months. In fact, they follow a similar annual cycle as the single-layer stratocumulus clouds, which are the least observed MBL cloud type, especially during the winter and spring months. Nevertheless, the dataset is only long enough to derive an anecdotal seasonal climatology, as revealed by the differences between months in the first and second years. As for the indeterminate category, it has typical occurrences around 10 % with small intraseasonal variability. Such low values probably come from the intermediate state of this type, acting as a transition between the other clouds based in the MBL (i.e., low and deep BL clouds).

The LTS has often been linked to the presence of low clouds. For instance, Zhang et al. (2010) provided coarse threshold values of LTS, less than 14 K and greater than 19 K, for small and large low-cloud fractions, respectively. These values correlate well with the cumulus and stratocumulus covers (see Fig. 3–3e). In fact, increases in LTS are usually associated with increases in stratocumulus coverage. Moreover, most values are close to, or above, the 14-K threshold, allowing cumulus clouds to form. This emphasizes the greater stability (mean of 17 K) found in the Azores, compared to the eastern equatorial Pacific (13 K, see Yin and Albrecht, 2000).

Fig. 3–3a demonstrates the propensity of marine clouds to produce precipitation. However, it often completely evaporates before reaching the surface, as illustrated by the separation into the three types considered (virga, light,

and intense) in Fig. 3–3d. Intense precipitation occurs mostly during fall and winter, weakly following the presence of deep BL clouds, suggesting that it is primarily associated with stronger and deeper systems. Other precipitation categories display no obvious annual variability.

3.4.2 Stratocumulus and Cumulus Cloud-Base Height Statistics

According to Table 3–2, stratocumulus and cumulus clouds are separated based on their horizontal extent. Furthermore, their cloud-base height statistics are different and this improves the robustness of the radar-lidar-based classification algorithm. The distributions of their hourly averaged cloud-base heights are compared in Fig. 3–4a. Only hourly periods with a cloud fraction greater than 10 % for the given type are included in the analysis. In addition, any hourly period with intense precipitation is also excluded to avoid possible contamination of the ceilometer cloud base. Although considerable variability in the cloud base occurrences of these two cloud types is observed, a separation is clearly visible between the two distributions, with cumulus clouds forming lower than stratocumulus clouds. This is consistent with the frequently observed cumulus under stratocumulus MBL cloud structure in the Azores. Yet, some stratocumulus bases have been detected at very low altitudes (below 500 m, below most cumulus). Such low-based stratocumulus clouds have been sampled during ASTEX (de Roode and Duynkerke, 1997); however, foglike conditions could have contaminated the statistics.

The hourly-averaged stratocumulus cloud-top height and cumulus cloud-base height are compared with the MBL inversion base and the transition layer top respectively (Fig. 3–4b). The MBL inversion base and transition layer top are estimated from the radiosondes. The cloud boundary heights used in the comparison with the radiosondes are 1-h averages centered on the sounding launch time. In addition, a minimum of 10 % cloud fractional coverage is

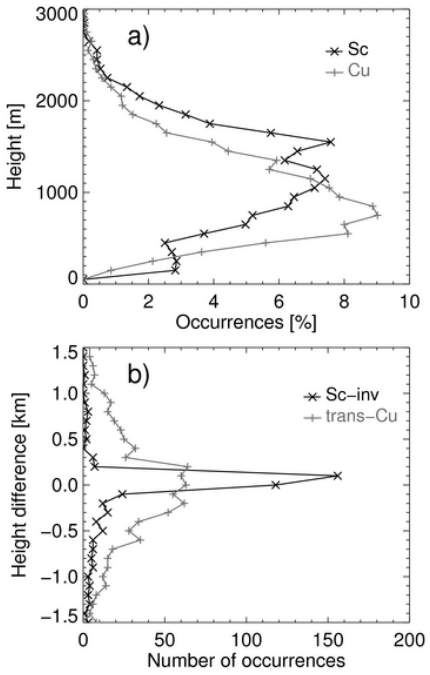

Figure 3–4: (a) Distributions of the hourly cloud-base heights for the stratocumulus (black line) and cumulus (gray line) clouds. (b) Distributions of the distance between the transition layer and the cumulus hourly base (gray line), and between the stratocumulus hourly top and the inversion layer (black line).

required and the absence of intense precipitation. The results are again in reasonable agreement with the expectations: both distributions are peaking near a zero difference, although the cumulus cloud base exhibits higher variability around the transition layer top. The broader distribution of cumulus cloud-base heights around the transition layer top height can be partially explained by their intermittent character and their role in maintaining the transition layer in the first place (Stevens, 2007) and the difficulty in retrieving the hourly averaged cloud base, especially in shear conditions. Furthermore, part of the variability might be caused by the challenge of correctly detecting the transition layer in noisy soundings and from cumulus clouds linked to other clouds (i.e., breaking deep BL, stratocumulus, or indeterminate clouds).

The double-peak cloud-base height structure observed for the stratocumulus clouds is explained by their seasonal cycle (Fig. 3–5a). The lower peak (around 1100 m) results from summer cases, while the higher peak (around 1600 m) results from the transition periods (spring and fall, mainly May and September). The winter season did not experience much stratocumulus coverage (as noticed in Fig. 3–3c) and thus does not contribute much. This seasonal dependence could be linked to the dominant air mass, which in turn is influenced by the strength of the high pressure system. The agreement between the stratocumulus tops and the inversion base is still visible after averaging them monthly, except in winter when the stratocumulus clouds are less frequent (Fig. 3–5a). Interestingly, the averaged stratocumulus top is sometimes within the inversion layer. This agrees well with recent in situ observations (e.g., Carman et al., 2012), although the measurements have a great variability (not depicted here) due to intraseasonal variations and various air mass intrusions. Another noticeable finding is the very frequent occurrence (higher than 80 %) of inversion and transition layers in the MBL throughout the field campaign (Fig. 3–5b). The occurrence is based on the monthly fraction of soundings with inversion and/or transition layers. The persistence of transition layers indicates the lack of well-mixed conditions in the subcloud layer.

MBL Variability During Single and Multilayer Cloud Conditions

A detailed analysis of the MBL variability during stratocumulus and stratocumulus over cumulus conditions and their corresponding MBL thermodynamic structure is presented here. Since a vertical stratification of the MBL influences the development of these low clouds, the MBL thermodynamic structure is first investigated using the soundings directly, without classifying them by cloud type (see Fig. 3–5b). Inversion-topped MBLs were encountered by

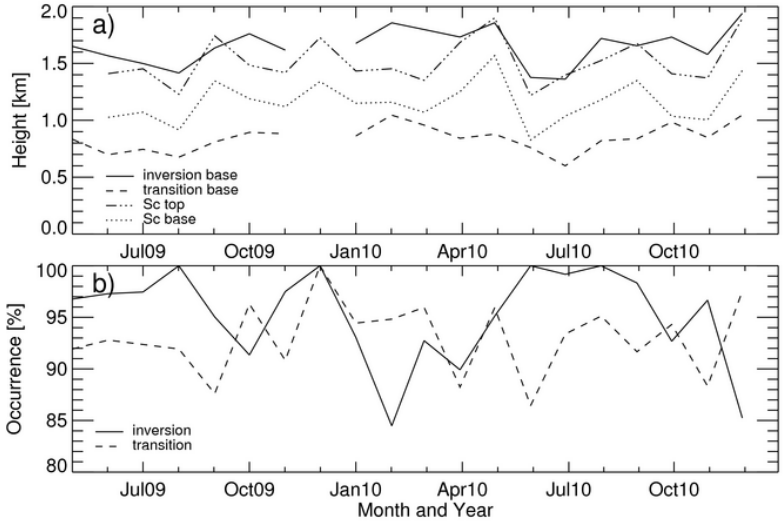

Figure 3–5: Monthly statistics of (a) the transition and inversion layers base height, and the stratocumulus clouds boundaries and (b) the occurrences of the inversion and transition layers, as a fraction of the number of soundings per month.

95 % of the soundings. Interestingly, the remaining 5 % of the soundings, which are inversion free, occurred mostly in wintertime—the season when deep systems are more frequently observed. This also supports the strong influence of the nearby high pressure system, which would sustain the inversion cap through the divergence it creates. Similarly, 92 % of the soundings presented a transition layer signature. However, this fraction is roughly the same for all studied months, showing no clear preference to any season. This is consistent with the constant coverage of cumulus clouds throughout the campaign, which help create and maintain this MBL structure (Stevens, 2007).

The proportions of transition and inversion layers found in soundings are much larger than observed over the eastern equatorial Pacific (Yin and Albrecht, 2000). It is reasonable to hypothesize that significantly strong mixing in the layer above the transition is required to support a clear temperature jump at its base. Radiative cooling associated with extensive clouds in the upper MBL may provide such mixing. In purely trade cumulus BL, this mixing is less efficient and the transition layer is less well defined. Interestingly, the

transition layer height closely follows the inversion base height annually (see Fig. 3–5a), which further supports this hypothesis.

The MBL thermodynamic structure is also analyzed using its cloud structure. Every hour of the day, the time fraction of multilayer low clouds is recorded along with the standard deviation of the ceilometer first cloud base. If multilayer conditions exist for more than 10 % of the hour and the cloud-base standard deviation is larger than 300 m (depicting broken clouds under a stratiform layer), then the hour is classified as multilayer cloud condition. On the other hand, if only a single cloud layer is detected within the hour and the cloud-base standard deviation is less than 100 m (ensuring a single level), then the hour is classified as single-layer cloud condition. Using the number of hours every month classified as single or multilayer cloud conditions, their diurnal and seasonal cycle can be estimated (Fig. 3–6). The observations suggest the presence of a weak diurnal cycle with increased single-layer occurrences during daytime and the opposite for multilayer conditions. Although this seems counterintuitive from a diurnal decoupling view, it is supported by the near-constant decoupled state of the MBL (see Fig. 3–5b), allowing cumulus to be omnipresent, while stratocumulus tend to fill in preferentially during nighttime. On the other hand, the MBL does show more multi-layer cases in the wintertime and more single-layer clouds in the summertime, with associated transitions in the spring and fall seasons. This result is consistent with a weaker high pressure system in winter, allowing for a weaker and higher (see Fig. 3–5a) inversion, providing more vertical extent to form multiple clouds.

The soundings collected within an hour of single and multilayer cloud conditions are further analyzed to identify the main feature of their corresponding thermodynamic structure in the MBL. Each sounding is first analyzed separately to detect the height of the inversion and transition layers (if present).

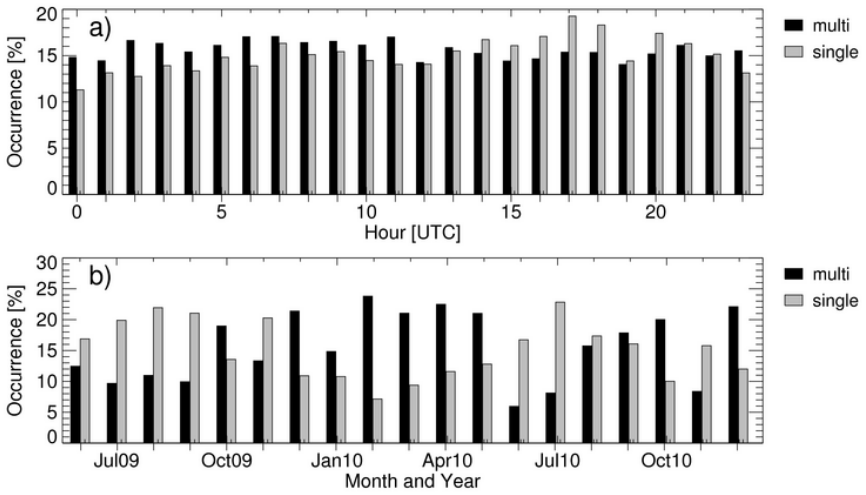

Figure 3–6: (a) Daily and (b) annual cycles of hours characterized by single and multilayer clouds in the MBL (the gray and black bars, respectively). Each number of occurrences is normalized by the total number of hours with data within the considered hour in (a) or month in (b) to provide percentage values. Note that the local standard time in the Azores is UTC − 1 h.

The analysis indicated that the vast majority of the analyzed soundings that correspond to both single and multilayer cloud conditions show a transition layer (as seen in Fig. 3–5b). The soundings that did not have a detectable transition layer in the MBL were shallow (inversion height below 1 km), which might have prevented the complete formation of a transition layer. This concurs with previous studies (Albrecht et al., 1995; Wood and Bretherton, 2004) suggesting that the atmospheric BL must be deeper than ∼700 m to have a decoupled structure.

The single cloud layer soundings are separated in two subsets according to the thermodynamic layer linked to the cloud layer: the inversion (SLa) or the transition (SLb). A third category of soundings corresponds to multilayer cloud conditions (ML). Although the cloud type is not directly used in this classification, each group corresponds to a different MBL situation: stratocumulus (SLa), cumulus (SLb), and stratocumulus with cumulus underneath (ML). Using all soundings with a transition layer, composited profiles

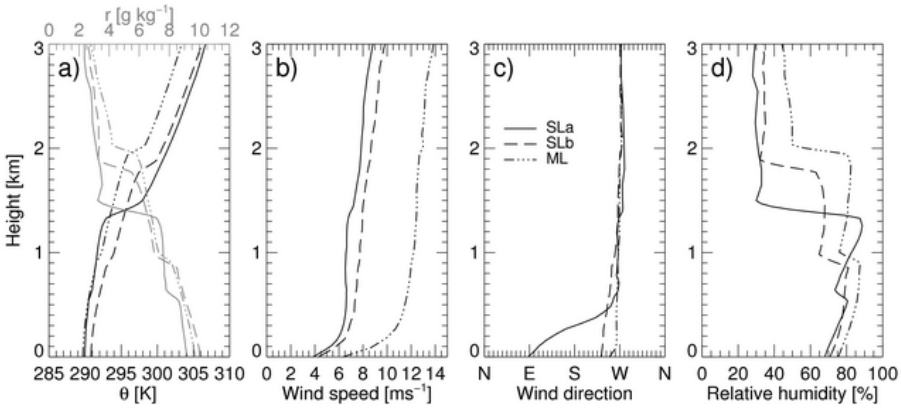

Figure 3–7: Profiles of (a) potential temperature (black; bottom axis) and water vapor mixing ratio (gray; top axis), (b) wind speed, (c) wind direction, and (d) relative humidity composited over the cases with multiple BL clouds (dashed-dotted lines) and a single BL cloud at the inversion or transition level (solid and dashed lines, respectively), all presenting a transition layer.

were obtained for each group following the layer-by-layer averaging method described in section 3.3.2 (see Fig. 3–7). The SLa cases have a lower averaged inversion height, reminiscent of the difficulty to fully decouple shallow MBLs. They also have the strongest potential temperature and mixing ratio jumps through the inversion layer associated with the weakest jumps at the transition layer, supporting only the stratocumulus cloud. Comparatively, both layers show strong jumps for the SLb cases. A strong inversion in both types of single layer cases is consistent with their tendency to occur during summer, when the high pressure system is stronger.

The averaged profiles of potential temperature and mixing ratio exhibit a gradual transition from the stratocumulus (SLa) to stratocumulus with cumulus (ML) to cumulus (SLb) cloud regimes, supporting the usual picture of the transition from midlatitude to tropical MBL often experienced in the Azores (de Roode and Duynkerke, 1997). The profiles with the lowest relative humidity correspond to cloud conditions associated with the transition layer only (SLb group), consistent with the broken nature of cumulus clouds. Multilayer cloud conditions show higher wind magnitudes on average. However, there is

a great variability associated with the wind measurements, partly due to seasonal differences (not shown). The wind direction averaged profiles are very similar above the base of the transition layer; however, an easterly wind at the surface seems to be linked with single cloud layer detections near the inversion. Although not shown here, this change in direction in the SLa group happens in the summer, while fall cases are more unidirectional. Also, winter and spring single-layer cases tend to have a greater southern component. However, due to the wide range of variability in the data, more cases are needed to verify the existence (or lack of) of a preferred wind speed and direction (or synoptic situation) for each MBL structure through the seasons.

3.4.3 Stratocumulus Clouds

3.4.3.1 Macroscopic Properties and Thermodynamic Structure

Using the hours with single-layer stratocumulus conditions, 35 days when stratocumulus clouds persist through most of the day are selected for additional analysis. Most of the selected days occurred in early summer (June–July) or late fall (October–November). During the summer period, stratocumulus clouds have lower cloud-base heights compared to the late fall (causing the bimodal structure in Fig. 3–8a, as previously noticed in Figs. 3–4 and 3–5a using all stratocumulus clouds). Distinct difference in the distribution of cloud thickness is observed during drizzling (excluding intense precipitation) and nondrizzling conditions. The distribution of cloud thicknesses for periods with a drizzle shaft peaks around 250–300 m, while the distribution of cloud thicknesses for periods without virga peaks at 150 m (Fig. 3–8b). On the contrary, there is no clear difference in the distributions of cloud bases using the same separation (see Fig. 3–8a). The peak below 200 m for the cases "without drizzle" comes mostly from periods when the ceilometer measurements are

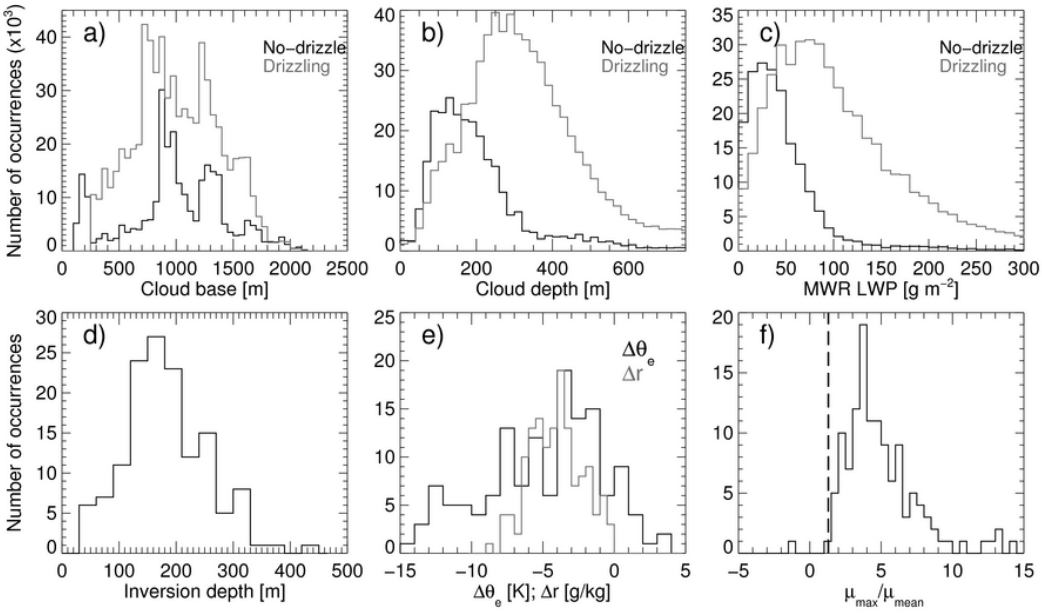

Figure 3–8: Distribution of instantaneous (a) cloud base and (b) depth, (c) LWP, (d) inversion depth and (e) strengths, and (f) transition strength measured in the selected stratocumulus cases. In (a)–(c), measurements were divided according to the absence or presence of a drizzle shaft (the black and gray curves, respectively). In (e) the strength is reported in terms of equivalent potential temperature (black curve) and in terms of water vapor mixing ratio (gray curve). In (f) the vertical dashed line corresponds to the minimum value used to detect a transition layer (based on Yin and Albrecht, 2000).

compromised by heavy precipitation, as they correspond to the tail of larger depths seen in Fig. 3–8b.

Another way to demonstrate the difference in cloud thickness during drizzling and nondrizzling periods is through their corresponding distributions of LWP (see Fig. 3–8c). Although small amounts of liquid water are possible in drizzling and nondrizzling stratocumulus clouds, LWP greater than 75–100 $\mathrm{g\,m^{-2}}$ are sufficient to produce drizzling conditions. This result compares well with previous studies conducted in various stratocumulus decks (e.g., Wood, 2005a; Zuidema et al., 2005; Serpetzoglou et al., 2008; Kubar et al., 2009). Moreover, the nondrizzling distribution peaks around 30 $\mathrm{g\,m^{-2}}$, which is near the theoretical accuracy of the deployed MWR. Also, as before, the

tail of greater LWP visible for the nondrizzling profiles is associated with the deeper stratocumulus clouds with bases affected by precipitation.

The soundings recorded during the selected 35 days are used to describe the inversion and transition layer characteristics. As expected, all recorded soundings indicate the presence of an inversion layer near the stratocumulus cloud top. Owing to their small number (141) and the difficulty to properly define the associated drizzling character, no separation was performed. The depth of the inversion layer shows a strong peak just below 200 m (see Fig. 3–8d). This is much deeper than most observations (e.g., Carman et al., 2012) and simulations (e.g., Stevens et al., 1999). Nevertheless, this derived quantity is likely influenced by the smoothing of the data by the sounding software, as well as by wetting, which would have mainly caused an overestimate of the layer top (see Caldwell et al., 2005).

The full distributions of the jumps in equivalent potential temperature ($\Delta\theta_e$) and water vapor mixing ratio (Δr) are given in Fig. 3–8e. As observed in various stratocumulus studies, $\Delta\theta_e$ is often negative. Although this situation can still satisfy the stability criterion (Kuo and Schubert, 1988; MacVean and Mason, 1990) since Δr is usually also negative, most values fall within the range generally accepted for the criterion, and only a few soundings are clearly stable. Such persistence under unstable conditions has been observed in other studies (e.g., Faloona et al., 2005; Carman et al., 2012). Yamaguchi and Randall (2008) explain this behavior by the weakness of the feedback in stratocumulus.

Based on the methodology devised by Yin and Albrecht (2000) for the east Pacific (as described in section 3.3.2), the presence of a transition layer was also diagnosed for most of the persisting stratocumulus soundings, as the

threshold value was usually exceeded (see Fig. 3–8f). This suggests that the stratocumulus layer is decoupled from the surface.

3.4.3.2 Diurnal Cycle

Using the hourly-derived statistics from the 35 selected days, a composite daily cycle is derived for the occurrence and boundaries of the stratocumulus clouds and their associated drizzle, using 3-h bins (Fig. 3–9). As expected, the cloud fraction is very high ($> 80\,\%$) throughout the day. The maximum values of cloud fraction are found during nighttime, with a gradual decrease of coverage occurring in the morning hours, followed by an increase after sunset, as in other marine decks (e.g., Ghate et al., 2009). The marine stratocumulus clouds observed in the Azores are usually precipitating ($70\,\%$ of the time), and the small decrease in cloud fractional coverage during daytime is also associated with a reduced drizzling fraction reaching ground. In fact, while virga is constantly detected in $45\,\%$ of an average stratocumulus, light precipitation has a marked decreased occurrence during the day. As for intense precipitation, it rarely occurs in a stratocumulus (less than $5\,\%$), and it is mostly around sunset and sunrise. Note that the following panels of Fig. 3–9 show pseudo-daily cycles, as each value is the average weighted by the hourly fractions. As such, periods from various cases are mixed together, and the resulting cycle should be taken with a grain of salt, especially for the measurements affected by the seasons (e.g., boundaries heights).

Shallow MBLs are needed during nighttime to observe nondrizzling conditions, as indicated by the lower cloud boundaries, while the development of drizzle during daytime does not depend on the MBL depth (Fig. 3–9b). Light drizzle periods correspond to thicker cloud decks (cf. 450–550 m to 200–270 m) and higher LWP values (cf. 140–200 $\mathrm{g\,m^{-2}}$ to 30–60 $\mathrm{g\,m^{-2}}$). Interestingly, virga periods have similar cloud depths ($\sim$300 m) as the nondrizzling periods but

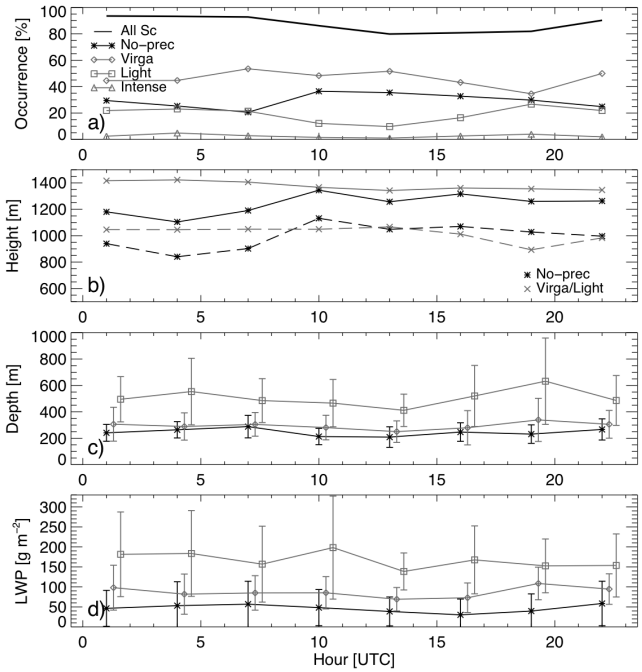

Figure 3–9: Three-hourly statistics, composited from 35 days of persisting single-layer stratocumulus coverage, separated between periods without radar echoes below the cloud base and periods with various types of drizzle (virga, light, or intense): (a) fraction of the stratocumulus coverage, (b) cloud-base (dashed) and cloud-top (solid) heights, (c) cloud depth, and (d) LWP from the MWR. The average stratocumulus coverage is also included in (a) with the thick line. The error bars in (c),(d) represent the standard deviations.

constantly show larger LWP values (70–100 g m^{-2}). Furthermore, only the LWP of virga periods have a distinctive daily cycle, with a pronounced increase near sunset. A similar cycle is observed in the cloud depth of the light drizzle periods, following its stratocumulus coverage (Fig. 3–9c,d). Note that the variability between the cases remains important, creating some overlap.

3.4.3.3 Vertical Air Motion Statistics

Vertical air motions play an important role in the evolution of stratocumulus. Considering only the time periods without a drizzle shaft in the 35 selected cases, hourly vertical air motion statistics are derived (section 3.3.3). Hours with less than 15 % nondrizzling coverage are discarded from the following analysis. In the analysis, positive velocities indicate updrafts. Thus, negative

skewness of the hourly distribution of vertical air motion indicates the presence of a few strong narrow downdrafts compensated by many weak broader updrafts. Daytime and nighttime composites of the vertical air motion statistics are constructed to highlight differences between day (1100–1700 UTC) and night (2300–0500 UTC) time periods. Time periods close to local sunrise or sunset are discarded from this type of analysis to ensure a clear separation between the two periods.

The vertical air motion variance profiles peak at the cloud base (Fig. 3–10a). As noted in previous studies of the MBL (e.g., Nicholls, 1989; Hignett, 1991; Lothon et al., 2005; Guo et al., 2008; Ghate et al., 2010), it indicates a maximum of turbulent kinetic energy near the middle of the MBL since our measurements cover the top part of the MBL occupied with cloud. Higher variance is observed during nighttime, as observed by Hignett (1991), and is consistent with turbulence driven by cloud-top radiative cooling. This excess turbulent energy is responsible for the thickening of the stratocumulus deck, as well as its higher cloud fraction and stronger drizzle presence. The nighttime skewness profile of the vertical air motion is negative throughout the cloud layer (Fig. 3–10c). This is consistent with cloud-top radiative cooling as the driving mechanism and most nocturnal in situ observations (e.g., Kollias and Albrecht, 2000; Guo et al., 2008). During daytime however, skewness values are closer to neutral in the lower two thirds. Near the cloud top, both periods show a similar behavior, strong negative values, suggesting cloud-top-driven turbulence.

The diurnal evolution of the vertical air motion variance and skewness in the stratocumulus layer is shown in Fig. 3–10b,d using 3-h bins. The vertical air motion variance maximum is still clearly at night in the bottom half of the cloud. The periods exhibiting the highest variance values in the lower part

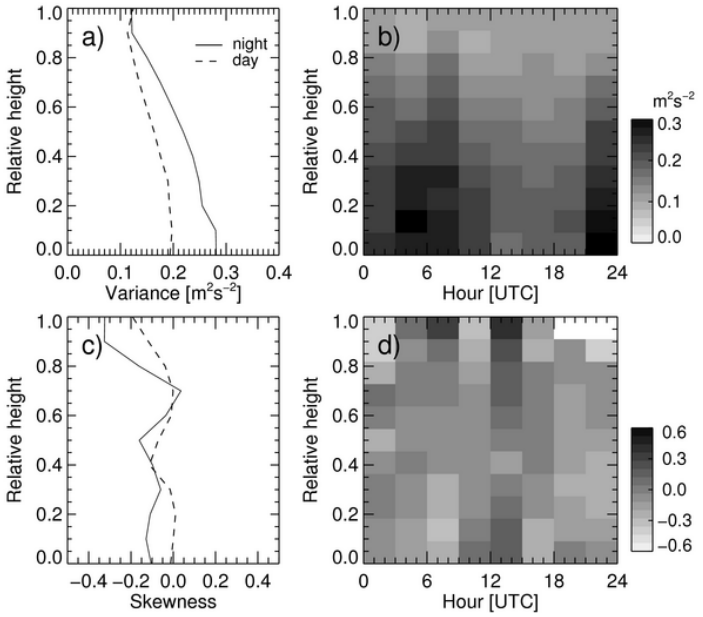

Figure 3–10: Night (solid) and day (dashed) average profiles of the hourly estimated (a) variance and (c) skewness of the radar measured mean Doppler velocity and 3-hourly profiles of the (b) variance and (d) skewness of the radar measured mean Doppler velocity, composited over the selected periods of stratocumulus without drizzle under the cloud base. Note that the vertical axis represents the height above cloud base, in units of cloud depths, thus covering only the cloud layer.

of the cloud are 2100–2400 UTC and 0300–0900 UTC. Minimum vertical air motion variance in the lower part of the cloud is observed during the 1200–1800 UTC period. Close to the cloud top, the variance appears consistently low through the day. The diurnal cycle of the vertical air motion skewness better captures the role of cloud-top radiative cooling as a source of turbulence during nighttime. Positive values are also observed, but mostly in the top half during daytime, especially around noon when positive values appear to take over the whole cloud, consistent with surface-driven turbulence.

3.4.3.4 Updraft Mass Flux

The in-cloud vertical air motions support a significant portion of the turbulent transport of heat and moisture in the cloud layer. The turbulence transport is often organized in temporally-spatially coherent updraft and downdraft

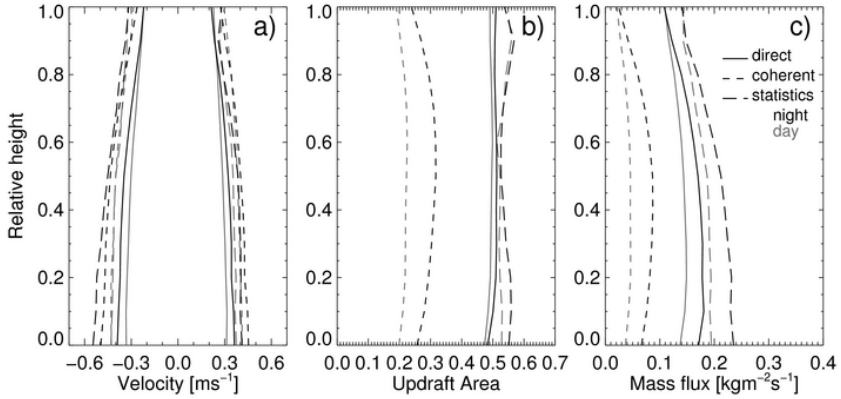

Figure 3–11: Night (black) and day (gray) profiles of (a) updraft and downdraft velocities, (b) updraft area, and (c) mass flux associated with the updrafts, as obtained using three methods: direct sampling (solid lines), coherent structures only (short dashes), and the statistical method (long dashes).

structure. Here, the vertical air motion measurements are separated into nighttime and daytime periods and the analysis described in section 3.3.3 is applied to estimate the mean updraft and mean downdraft velocity profiles, the updraft area profile and the updraft mass flux profile. The resulting in-cloud profiles are shown in Fig. 3–11, using the three possible methods (direct, coherent, and statistical). First, note that the statistical technique gives generally the same profiles as the direct sampling, despite a small overestimate of the magnitudes, as found in LES models (Randall et al., 1992) and continental stratocumulus (Kollias and Albrecht, 2000).

The mean amplitudes of velocity in updrafts and downdrafts are very similar. This is linked to the cloud separating into two halves (one going up, the other going down) on average throughout its depth, which compares well with continental stratocumulus clouds (e.g., Kollias and Albrecht, 2000; Ghate et al., 2010), and other marine cases (e.g., Nicholls, 1989; de Laat and Duynkerke, 1998). However, coherent structures are responsible only for 40 %–60 % of the total mass flux. The contribution of coherent structures to the turbulent transport is maximized at night near the middle of the cloud. The

mean velocity of coherent structures is also stronger, as expected. Nevertheless, their contribution to the mass flux is still limited, especially during daytime. As observed in the majority of stratocumulus decks, the mass flux is greater during nighttime and in the bottom half of the cloud, when and where the turbulence is stronger. It is also linked to the mean velocities being maximized near the cloud base ($\sim$0.5 m s^{-1}), decreasing with height.

A similar analysis performed at the cloud base of cumulus gives comparable values, although the night and day results are closer. The main differences are stronger mean updraft and downdraft velocities and a weaker contribution from nighttime coherent structures. A more detailed analysis of the shallow cumulus cloud dynamics in the Azores can be found in Ghate et al. (2011).

3.5 Summary

The CAP-MBL campaign led to the collection of an extensive and well-documented ground-based dataset of MBL clouds. Here, the frequency of occurrence of different cloud and precipitation types along with their macroscopic properties (e.g., cloud boundaries) and MBL structure are presented. Several remote sensors are used to develop statistics of occurrence of various cloud and precipitation types. Clouds occur frequently throughout the 19-month period that was analyzed (June 2009–December 2010), with a maximum (80 %) during the winter-spring months and a minimum (60 %–65 %) during the summer months. Precipitation occurrence is also very high (30 %–40 %), but precipitation only reaches the ground less than 15 % of the time. Most intense precipitation events correlate well with the occurrence of non-MBL clouds linking them to midlatitude cyclones during the winter and spring months.

A predominance of MBL clouds was observed all year long, while higher clouds show enhanced occurrences in winter. Moreover, cumulus clouds are

present during all seasons, while stratocumulus clouds occur preferably during the transition periods. These two types often occur together, with each type being tied to a distinct thermodynamic layer (the cumulus to the transition layer and the stratocumulus to the inversion layer). The strength of the subtropical high pressure system influences the height (and presence) of the inversion, thus regulating the height of the stratocumulus layer, as well as the possibility to create two cloud layers in the MBL. In fact, on average, a stronger θ increase, a greater LTS value, and a lower inversion base tend to accompany a greater surface pressure in the Azores (a proxy for the strength of the subtropical anticyclone). In turn, although not shown here, a higher pressure also seems more favorable for a stratocumulus formation alone, while the cumulus clouds would form underneath at lower surface pressure.

Analysis of the sounding profiles demonstrates the near omnipresence of decoupling in the Azores MBL—a new finding that is only made possible by the long measurements made during the campaign. Cloud layers do not always reveal this decoupling, presenting only one layer in the observations. A two-part explanation can be hypothesized. First, a strong transition layer could prevent moisture from reaching the upper cloud layer. Second, a transition layer too weak might be unable to prevent the vertical development of cumulus clouds that would then fuse with the stratocumulus layer.

Thirty-five days characterized by the presence of persistent single-layer stratocumulus clouds were selected to gain further insights on their diurnal cycle, macroscopic properties (LWP and cloud boundaries), and dynamics. The minimum cloud coverage is observed in the afternoon. This is consistent with the findings of other studies using ground-based and satellite observations and models (e.g., Rozendaal et al., 1995; Abel et al., 2010). Although the fractions found here are greater (remaining above 80 %), this is probably a

bias due to the selection of persisting stratocumulus layers. Diurnal clearing is accompanied by a thinning of the cloud layer and a decrease in ground precipitation coverage and LWP. Again, this is consistent with other stratocumulus studies, such as those performed in the southeast Pacific (e.g., Wood et al., 2002; Abel et al., 2010). Furthermore, it was observed that stratocumulus is most likely to drizzle if the cloud depth exceeds 250 m and the LWP is above $60\,\mathrm{g\,m^{-2}}$. Local maxima of ground precipitation coverage occur around sunrise and sunset.

We find that stratocumulus clouds are more turbulent during nighttime. Throughout the day, the turbulence maximized in the bottom half of the cloud, except around sunrise and after sunset when it extended through higher levels. Profiles of skewness from the velocity time series are consistent with cloud-top radiative cooling during nighttime and surface heating around noon, as reported in many other stratocumulus clouds (e.g., Kollias and Albrecht, 2000). Mass flux is greater at night with the updrafts covering about half of the cloud, in accordance with observations in other decks and current theories (e.g., Nicholls, 1989; de Laat and Duynkerke, 1998; Kollias and Albrecht, 2000). However, coherent updraft structures contribute 40 %–60 % of the total updraft mass flux. Higher contributions (70 %–75 %) have been observed in previous studies (e.g., Kollias and Albrecht, 2000).

Various parts of the analysis were complicated, or even hindered, by the great variability observed between cases. Seasonal differences and air mass origin are likely to have a strong influence on this aspect. They should be studied further to understand better their impacts. For the moment, it is difficult to know the aerosol source and content in each cloud, especially when the MBL has a decoupled structure.

Chapter 4
Modeling of the Drizzle Onset and Early Growth

Chapter 3 highlighted the occurrence of persisting stratocumulus coverage during the CAP-MBL campaign, providing a data set to study this type of clouds. The ultimate goal for this work is to improve the retrieval of the cloud PSD. Therefore, a certain knowledge of the cloud droplets location, and of the drizzle presence and impacts, is needed. Previous studies have typically used a simple radar reflectivity threshold to determine the location of drizzle-free volumes. However, it was recently showed that this method is highly subjective and depends on the cloud environment. The present chapter revisits the determination of drizzle location inside a stratocumulus cloud. Various modeling frameworks are used. A comparison with continental cases from the SGP site is also made, to ensure the results are general to all stratocumulus clouds.

This chapter is the synthesis of the work done by the thesis author, as part of her research project, for a two-part paper published in the Atmospheres division of the Journal of Geophysical Research:

Kollias, P., J. Rémillard, E. Luke, and W. Szyrmer, 2011a: Cloud radar Doppler spectra in drizzling stratiform clouds: 1. Forward modeling and remote sensing applications. *J. Geophys. Res.*, **116**, D13201, doi:10.1029/2010JD015237.

Kollias, P., J. Rémillard, W. Szyrmer, and E. Luke, 2011b: Cloud radar Doppler spectra in drizzling stratiform clouds: 2. Observations and microphysical modeling of drizzle evolution. *J. Geophys. Res.*, **116**, D13203, doi:10.1029/2010JD015238.

4.1 Introduction

An investigation of the precipitation formation requires the knowledge of the location of the precipitating particles in the observations. It was long thought that a simple radar reflectivity threshold could do that (Frisch et al., 1995; Mace and Sassen, 2000; Wang and Geerts, 2003; Krasnov and Russchenberg, 2005). However, a discrepancy in the actual threshold used between experiments over the years led Liu et al. (2008) to review the whole idea. They concluded that this criterion depends on the number concentration of cloud condensation nuclei, and that the threshold method has an ambiguous part linked to a gradual change. As the number concentration is not easily available, another method is needed.

A simple correlation between the radar reflectivity and the mean Doppler velocity can be useful here, as cloud droplets have negligible fall velocity and should show no such correlation. However, this requires a subset of data to find a single reflectivity threshold, while assuming it applies to the whole data set.

A more thorough method involves the retrieval of microphysical parameters in the cloud. That way, even the drizzle water content would be known at every gate observed by the instruments. However, no known and proven algorithm exists yet for every cloud region, and this could become quite tedious to apply everywhere.

Here, we propose to look deeper in the radar core measurement, the Doppler spectrum, and its parameters. Precipitation-size particles should appear at greater downward velocities in the spectrum, forming a bump that gradually separates from the cloud peak as precipitation grows. This will be reflected differently in various parameters of the Doppler spectrum. As long

as noise does not impede the detection of such a signal, precipitation onset would then be visible directly from the radar observations.

This chapter includes first a description of the radar Doppler spectrum parameters considered here, followed by a look at observations done in the Azores with the WACR. Finally, a microphysical modeling study is done to explain the main results noticed in the observations.

4.2 Radar Doppler Spectrum Parameters

Millimeter radars record the full Doppler spectrum at each sampled range gate. This measurement relates to the size distribution of particles found inside the sampled volume. However, simple relations between size and velocity cannot be applied here, as air motions affect the particles' movements. Thus, the measured velocities are the particles' apparent motion along the radar's line of sight. In a nutshell, motions at scales larger than the sampled volume move all particles the same way, translating the full spectrum by an unknown amount, while motions at scales smaller than the sampled volume add a random component to each particle, broadening the measured spectrum.

Five parameters of a Doppler spectrum are considered here: the reflectivity factor (Z), the mean Doppler velocity (V_D), the spectrum width (σ_D), the skewness (s_D), and the kurtosis (k_D). These parameters measure respectively the strength of the signal, its mean, its spread around the mean, its asymmetry, and its "peakedness" or its tails' heaviness. They relate to the zeroth to fourth moments of the spectrum. Reflectivity, velocity and width have received much attention in previous cloud studies. However, skewness and kurtosis are two less-known parameters that further describe the shape of the spectrum. The skewness value is zero when the spectrum power is evenly distributed on either side of the peak (e.g., for a symmetric function like the Gaussian), while a shift of power to the right (left) of the peak results in a

positive (negative) skewness. The kurtosis, on the other hand, can be thought of as a "peakedness" measure: high (low) kurtosis indicates a sharp (rounded) peak. Another factor in the kurtosis value is the weight found in the tails: longer, fatter tails increase the kurtosis value. The Gaussian function is the reference, taking a kurtosis value of 3.

Because cloud and drizzle particles have typical sizes that allow the use of the Rayleigh approximation to describe the scattering of the radar's millimeter wavelength electromagnetic radiation, a full mathematical formulation of the five considered parameters is possible, assuming an analytical shape for each PSD and a size-velocity relationship. Here, we assume that both the cloud and drizzle PSDs can be approximated by a lognormal function:

$$n\left(r\right) = \frac{N}{\sqrt{2\pi}\sigma_x r} \exp\left(\frac{-\left(\ln r - \ln r_0\right)^2}{2\sigma_x^2}\right), \tag{4.1}$$

where r is the particle radius, N is the total number of drops per unit volume, σ_x is the logarithmic width of the distribution, and r_0 is the median radius (e.g., Frisch et al., 1995). The quantity $n(r)\,\mathrm{d}r$ represents the number of particles found with a radius between r and $r + \mathrm{d}r$. Truncations of the PSDs are also considered to see the effect of introducing the reality of finite PSDs, i.e. PSDs that cover only a range of sizes. The k-th moment of a truncated lognormal PSD is given by:

$$\langle r^k \rangle = \frac{1}{N}\int_{r_{min}}^{r_{max}} r^k n\left(r\right)\,\mathrm{d}r = \frac{F\left(k\right)}{2} r_0^k \exp\left(\frac{k^2\sigma_x^2}{2}\right), \tag{4.2a}$$

$$\text{with } F\left(k\right) = erf\left(\frac{\ln\left(r_{max}/r_0\right)}{\sqrt{2}\sigma_x} - \frac{k\sigma_x}{\sqrt{2}}\right) - erf\left(\frac{\ln\left(r_{min}/r_0\right)}{\sqrt{2}\sigma_x} - \frac{k\sigma_x}{\sqrt{2}}\right), \tag{4.2b}$$

where r_{min} and r_{max} are respectively the lower and upper bounds of the distribution and *erf* is the error function. The function $F(k)/2$ accounts for the use of a truncated PSD and its omission results in the expression discussed in

Frisch et al. (1995). For a cloud PSD, the lower bound typically doesn't affect the moments, and the second *erf* in the function $F(k)$ takes the value of -1.

The zeroth moment of the radar Doppler spectrum (i.e., Z) for an individual PSD and the combined cloud and drizzle PSDs can be expressed as:

$$Z_i = 2^6 N_i r_{0,i}^6 \exp\left(18\sigma_{x,i}^2\right) \left[F_i\left(6\right)/2\right], \tag{4.3a}$$

$$Z_{meas} = Z_c + Z_d = Z_d\left(1+\chi\right), \tag{4.3b}$$

where the subscript i indicates either cloud (c) or drizzle (d) PSD. The parameter $\chi = Z_c/Z_d$ is used here to determine the relative contribution of the cloud and drizzle PSDs to the observed radar Doppler spectrum parameters. The expression for the measured radar reflectivity factor is straightforward since turbulence does not influence the measurement, only spreading the returned power over a wider range of velocities.

Following Frisch et al. (1995), the k-th velocity moment of the radar Doppler spectrum is given by:

$$\langle V^k \rangle_D = \frac{\langle r^6 \left[V_f\left(r\right)\right]^k \rangle}{\langle r^6 \rangle}, \tag{4.4}$$

where $V_f(r)$ is the fall velocity of the particle with radius r. For each class of particles, a simple size-velocity relation is assumed. Cloud droplets are small enough that their fall velocity is in the Stokes regime: $V_f = cr^2$, with $c = 1.2 \times 10^8\,\mathrm{m^{-1}\,s^{-1}}$ (Rogers and Yau, 1989). On the other hand, a linear relationship usually represents well drizzle drops' fall speed, such that $V_f = ar - b$, with $a = 8333\,\mathrm{s^{-1}}$ and $b = 0.0833\,\mathrm{m\,s^{-1}}$ (Frisch et al., 1995). Therefore, Eq. 4.4 becomes, for each class of particles:

$$\langle V^k \rangle_{D,c} = \frac{c^k \langle r^{6+2k} \rangle}{\langle r^6 \rangle}, \tag{4.5a}$$

$$\langle V^k \rangle_{D,d} = \frac{\langle r^6 \left(ar - b\right)^k \rangle}{\langle r^6 \rangle}. \tag{4.5b}$$

4.2.1 Cloud Droplets Alone

If only cloud droplets are present in the radar sampling volume, the microphysical information that can be retrieved is limited. The radar reflectivity can be linked to the cloud PSD parameters, especially if integrated liquid water path measurements are available, but linkages are not available for the other radar moments (e.g., Frisch et al., 1998, 2002). Since cloud droplets have negligible fall velocities, spread over a very narrow range, air motions dominate the location and the shape of the radar Doppler spectrum: the vertical component of air motion (w_{air}) determines the observed mean Doppler velocity, and the turbulence broadening parameter (σ_t) determines the observed spectrum width. In addition, the Doppler spectrum skewness should be around zero and kurtosis near 3, since turbulence is assumed to have a Gaussian distribution. Nevertheless, the possibilities of deriving more information about the cloud PSD parameters will be further investigated in the next chapter. Moreover, the Doppler velocity and spectrum width of cloud spectral peak are traditionally used to retrieve, respectively, the vertical air motion (w_{air}) and the eddy dissipation rate (ε) with relatively small uncertainties (Kollias et al., 2001; O'Connor et al., 2005; Kollias and Albrecht, 2010).

4.2.2 Mixture of Cloud Droplets and Drizzle Drops

For the combination of two non-overlapping truncated lognormal distributions, the total k-th velocity moment is a reflectivity-weighted average of the k-th velocity moment of each distribution, as follows:

$$\langle V^k \rangle_D = \frac{Z_c \langle V^k \rangle_{D,c} + Z_d \langle V^k \rangle_{D,d}}{Z_c + Z_d} \approx \frac{\langle V^k \rangle_{D,d}}{1 + \chi}. \tag{4.6}$$

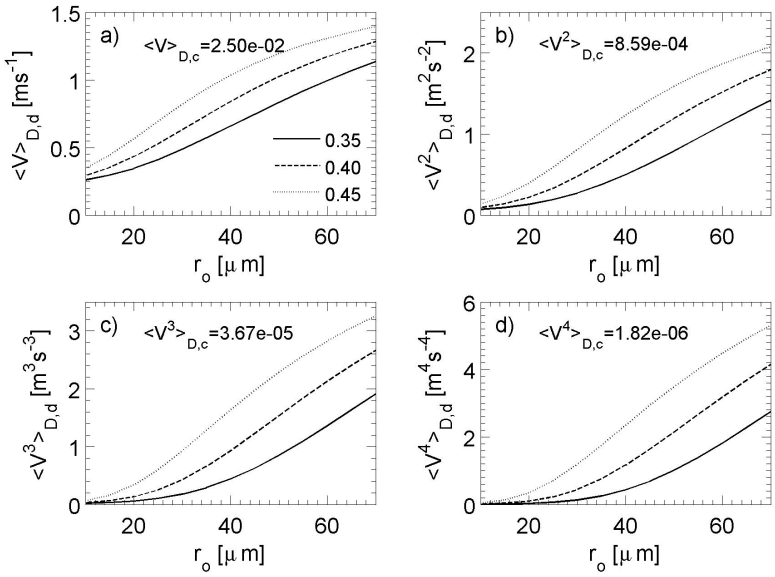

Figure 4–1: The first four velocity moments for a drizzle PSD as a function of drizzle modal radius $r_{o,d}$ and for three different PSD logarithmic widths $\sigma_{x,d}$ (0.35, 0.40, 0.45). The corresponding velocity moments for a cloud PSD with $r_{o,c} = 6.5\,\mu\text{m}$ and logarithmic width $\sigma_{x,c} = 0.35$ is shown in the legend.

The approximation on the right-hand side is based on the fact that the cloud PSD velocity moments $\langle V^k \rangle_{D,c}$ are negligible compared to their corresponding drizzle velocity moments. As illustrated in Fig. 4–1, the cloud and drizzle velocity moments are closest when the drizzle sizes are small, and even there, a difference of one order of magnitude is already present between each corresponding moments. This greatly simplifies the resulting equations for the parameters of the Doppler spectrum when a mixture of cloud droplets and drizzle drops is expected in the radar sampling volume.

From Eq. 4.6 and following the definition of each parameter, we obtain the formulas for the variance (σ^2_{PSD}), skewness (s_{PSD}) and kurtosis (k_{PSD}) of an ideal quiet-air ($w_{air} = 0$; $\varepsilon = 0$) radar Doppler spectrum of combined cloud and drizzle PSDs:

$$\begin{aligned}\sigma^2_{PSD} &= \langle V^2 \rangle_D - \langle V \rangle^2_D \\ &\approx \frac{\sigma^2_d + \chi \langle V^2 \rangle_{D,d}}{[1+\chi]^2},\end{aligned} \tag{4.7a}$$

$$s_{PSD} = \frac{\langle V^3\rangle_D - 3\langle V\rangle_D\langle V^2\rangle_D + 2\langle V\rangle_D^3}{\sigma_{PSD}^3}$$
$$\approx \frac{\sigma_d^3 s_d + \chi\left[(2+\chi)\langle V^3\rangle_{D,d} - 3\langle V\rangle_{D,d}\langle V^2\rangle_{D,d}\right]}{\left[\sigma_d^2 + \chi\langle V^2\rangle_{D,d}\right]^{3/2}}, \tag{4.7b}$$

$$k_{PSD} = \frac{\langle V^4\rangle_D - 4\langle V\rangle_D\langle V^3\rangle_D + 6\langle V\rangle_D^2\langle V^2\rangle_D - 3\langle V\rangle_D^4}{\sigma_{PSD}^4}$$
$$\approx \frac{\sigma_d^4 k_d + \chi\left[(3+3\chi+\chi^2)\langle V^4\rangle_{D,d} - 4(2+\chi)\langle V\rangle_{D,d}\langle V^3\rangle_{D,d} + 6\langle V\rangle_{D,d}^2\langle V^2\rangle_{D,d}\right]}{\left[\sigma_d^2 + \chi\langle V^2\rangle_{D,d}\right]^2}, \tag{4.7c}$$

Thus, the considered quiet-air radar Doppler spectrum parameters can be expressed as a function of the parameter χ and up to four velocity moments of the drizzle-only quiet-air radar Doppler spectrum (note that the Doppler spectrum parameters (variance σ_d^2, skewness s_d, and kurtosis k_d) appearing in Eqs. 4.7 are functions of the four velocity moments). The assumptions of a truncated lognormal function to describe the PSD and a linear size-velocity relationship allow the development of analytical functions for the drizzle velocity moments and spectrum parameters. Hence, the dependence on the drizzle PSD parameters in Eqs. 4.7 can be better developed, although the expressions quickly become long and complicated to read. Therefore, only the intermediate equations are shown here, with $F_d^*(k) \equiv F_d(k)/F_d(6)$:

$$\langle V\rangle_{D,d} = a r_{0,d} \exp\left(\tfrac{13\sigma_{x,d}^2}{2}\right) F_d^*(7) - b, \tag{4.8a}$$

$$\langle V^2\rangle_{D,d} = a^2 r_{0,d}^2 \exp\left(14\sigma_{x,d}^2\right) F_d^*(8) - 2abr_{0,d} \exp\left(\tfrac{13\sigma_{x,d}^2}{2}\right) F_d^*(7) + b^2, \tag{4.8b}$$

$$\langle V^3\rangle_{D,d} = a^3 r_{0,d}^3 \exp\left(\tfrac{45\sigma_{x,d}^2}{2}\right) F_d^*(9) - 3a^2 b r_{0,d}^2 \exp\left(14\sigma_{x,d}^2\right) F_d^*(8)$$
$$+ 3ab^2 r_{0,d} \exp\left(\tfrac{13\sigma_{x,d}^2}{2}\right) F_d^*(7) - b^3, \tag{4.8c}$$

$$\langle V^4\rangle_{D,d} = a^4 r_{0,d}^4 \exp\left(32\sigma_{x,d}^2\right) F_d^*(10) - 4a^3 b r_{0,d}^3 \exp\left(\tfrac{45\sigma_{x,d}^2}{2}\right) F_d^*(9)$$
$$+ 6a^2 b^2 r_{0,d}^2 \exp\left(14\sigma_{x,d}^2\right) F_d^*(8) - 4ab^3 r_{0,d} \exp\left(\tfrac{13\sigma_{x,d}^2}{2}\right) F_d^*(7) + b^4, \tag{4.8d}$$

$$\sigma_d^2 = a^2 r_{0,d}^2 \exp\left(13\sigma_{x,d}^2\right)\left[\exp\left(\sigma_{x,d}^2\right) F_d^*(8) - F_d^*(7)\right]^2, \tag{4.9a}$$

$$\sigma_{x,d}^3 s_{PSD} = a^3 r_{0,d}^3 \exp\left(\frac{39\sigma_{x,d}^2}{2}\right)\left[\exp\left(3\sigma_{x,d}^2\right) F_d^*(9) - 3\exp\left(\sigma_{x,d}^2\right) F_d^*(8) F_d^*(7) + 2F_d^*(7)^3\right], \tag{4.9b}$$

$$\sigma_{x,d}^4 k_{PSD} = a^4 r_{0,d}^4 \exp\left(26\sigma_{x,d}^2\right)\left[\exp\left(6\sigma_{x,d}^2\right) F_d^*(10) - 4\exp\left(3\sigma_{x,d}^2\right) F_d^*(9) F_d^*(7) + 6\exp\left(\sigma_{x,d}^2\right) F_d^*(8) F_d^*(7)^2 - 3F_d^*(7)^4\right]. \tag{4.9c}$$

In their final form, the quiet-air radar Doppler spectrum parameters depend on four variables: χ, $r_{0,d}$, $\sigma_{x,d}$, and $r_{max,d}$ (and N_d if Z is included, see Eq. 4.3). The dependence on the maximum drizzle radius is important only when this variable has a value similar to the median radius of the full lognormal PSD (e.g., in the early growth stages).

4.2.3 Effect of Air Motions

In reality, radar measurements are obtained in turbulent air, and air motions affect the resulting Doppler spectrum. The effect of w_{air} is a simple shift of the radar Doppler spectrum. It impacts only the observed mean Doppler velocity:

$$\langle V \rangle_{D,meas} = \langle V \rangle_D + w_{air}. \tag{4.10}$$

The impact of the turbulent eddies with spatial scales smaller than the radar sampling volume is formulated using a convolution of the turbulence PDF with the quiet-air radar Doppler spectrum. This assumes that all particles are affected in the same way by the turbulent motions, which is reasonable for the small sizes of cloud and drizzle particles. The resulting k-th moment

after the convolution can be expressed using the formula provided by Laury-Micoulaut (1976):

$$\sigma_{f*g}^{(n)} = \sum \frac{n!}{p_1!p_2!}\sigma_f^{(p_1)}\sigma_g^{(p_2)}, \text{ with } p_1 + p_2 = n. \tag{4.11}$$

Here, the functions f and g represent respectively the quiet-air Doppler spectrum and the turbulence PDF. Since the turbulence is assumed to be Gaussian with a mean value of zero and known second moment (σ_t^2), the resulting spectrum is characterized by the following convolved parameters:

$$\sigma_{meas}^2 = \sigma_{PSD}^2 + \sigma_t^2, \tag{4.12a}$$

$$s_{meas} = \frac{\sigma_{PSD}^3 s_{PSD}}{\left[\sigma_{PSD}^2 + \sigma_t^2\right]^{3/2}}, \tag{4.12b}$$

$$k_{meas} = \frac{\sigma_{PSD}^4 k_{PSD} + 3\sigma_t^2\left[\sigma_t^2 + 2\sigma_{PSD}^2\right]}{\left[\sigma_{PSD}^2 + \sigma_t^2\right]^2}. \tag{4.12c}$$

Eqs. 4.10 and 4.12 relate the mean Doppler velocity, spectrum width, skewness and kurtosis of the cloud radar Doppler spectrum to the microphysical and dynamical conditions.

Examples of measured Doppler spectra are illustrated in Fig. 4–2. These were recorded by the WACR as a stratocumulus passed over its deployment site in the Azores. The cloud spectrum (panel a) exhibits a weak spectral peak power with an approximate Gaussian distribution, while the drizzle spectrum (panel b) shows a strong, wide spectral peak with apparent non-Gaussian effects. Cloud-drizzle spectra (panels c-d) show even stronger non-Gaussian shapes with a "bump" on the left side of the primary spectral peak indicating the presence of a cloud PSD, creating bimodality in some cases.

4.3 Parameters Sensitivity

First, the sensitivity of the Doppler spectrum parameters needs to be tested, to ensure the viability of their use. To do so, a radar Doppler spectrum simulator (DSS) was developed to emulate Doppler spectra measured

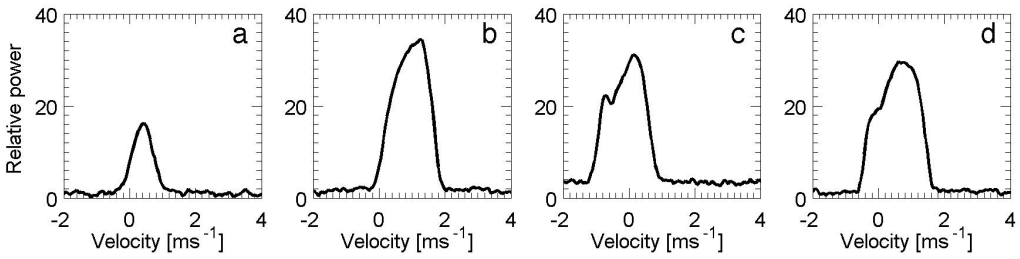

Figure 4–2: Examples of cloud radar Doppler spectra obtained from the WACR deployed in the Azores in volumes containing (a) only cloud droplets, (b) only drizzle drops, and (c)–(d) both types of particles. Note that positive velocities indicate downward motion, and the same ranges are used for all spectra.

by various ARM millimeter radars for a variety of cloud and/or drizzle PSDs and turbulent conditions. The DSS can simulate Doppler spectra from either PSD alone, or from combinations of them, using the ratio χ to determine the relative contribution of each PSD.

4.3.1 Forward Modeling

Typically, individual PSDs are considered to follow lognormal functions. However, other functions (e.g., exponential or modified gamma) are also possible, although not used here. Moreover, PSDs can be input by giving number concentrations in various size bins, as output by various growth models (e.g., see section 4.5). When analytical functions are used, a 10-µm gap is introduced between the cloud and drizzle PSDs, to avoid a discontinuity at the transition radius. Here, the transition occurs at 25 µm, as in previous studies (e.g., Frisch et al., 1995; Miles et al., 2000). Particles having a radius smaller than 1 µm are not considered in the DSS, as their impact is negligible and are rarely detected by in situ instruments. At the other end, a maximum radius of 250 µm is imposed, to avoid rain-size drops, although a smaller upper limit can be chosen in the simulations. Finally, the radius resolution in the analytical functions is 0.5 µm.

An ideal quiet air Doppler spectrum $S_Q(V_f)$ is obtained from the following formula:

$$S_Q\left(V_f\right) = \frac{\lambda^4}{\pi^5 |K|^2} n\left(r\right) \sigma_b \frac{\mathrm{d}r}{\mathrm{d}V_f}, \tag{4.13}$$

where λ is the wavelength of the considered radar, $|K|^2$ is the refractive index factor, and σ_b is the particle's backscatter cross-section. This last parameter is computed from Mie theory since the particles are all small enough to remain spherical, while the same size-velocity relations $V_f(r)$ mentioned in section 4.2 are assumed in the DSS to obtain the derivative in Eq. 4.13. The resulting S_Q is then interpolated to the simulated Doppler radar velocity resolution.

Both large- and small-scale air dynamics contribute to the radar Doppler spectrum shape and location. The DSS assumes that air motions are affecting equally all particles. At scales smaller than the sampling volume, turbulent motions are assumed to follow a Gaussian function $g(V_f)$ having a prescribed width (σ_t, the turbulent spectral broadening) that can be related to the turbulent eddy dissipation rate ε (e.g., Kollias et al., 2001; O'Connor et al., 2005). This turbulence is then parameterized by the following convolution:

$$S_t\left(V_f\right) = \left[S_Q * g\right]\left(V_f\right) = \frac{1}{\sqrt{2\pi}\sigma_t} \int_{-V_N}^{V_N} S_Q\left(x\right) \exp\left[\frac{-\left(V_f - x\right)^2}{2\sigma_t^2}\right] \mathrm{d}x, \tag{4.14}$$

where $S_t(V_f)$ is the radar Doppler spectrum resulting from the convolution of the turbulence function $g(V_f)$ with the quiet-air Doppler spectrum $S_Q(V_f)$, with the integral covering all velocity bins of the simulated Doppler spectrum, and V_N is the Nyquist velocity of the considered radar system. At scales larger than the sampling volume, only the vertical component is considered due to the typically narrow antenna beam width of millimeter radars that renders the horizontal components negligible. Therefore, the radar sampling volume averaged air motion causes a simple translation of the entire radar return power spectrum in the velocity space, by an amount equal to its vertical

component w_{air}. The radar Doppler spectrum resulting from that shift is simply $S_w = S_t(V = V_f + w_{air})$.

To better simulate radar Doppler spectrum, noise is added. Using the radar constant of the simulated radar and the target range, the well-characterized ARM millimeter radar receiver noise power P_N is converted from mW to $\mathrm{mm}^6\,\mathrm{m}^{-3}$. Noise has a white spectrum, causing its mean power to be independent of the frequency/velocity of the Doppler spectrum. Thus, the noise spectral density $P_{N,nfft}$ is provided by the following expression: $P_{N,nfft} = P_N/(N_{fft}\Delta v)$, where N_{fft} is the number of points in the fast Fourier transform used to obtain the radar Doppler spectrum and Δv is the spectral velocity resolution. Once the mean noise power density is estimated, we add a random fluctuation component following the method described by Zrnić (1975) and the spectral power density of the signal-plus-noise is given by the expression: $P_{S+N,nfft}[i] = -(S_w[i] + P_{N,nfft})\ln(x[i])$, with $i = 1, \ldots, N_{fft}$ and x is a random number uniformly distributed between 0 and 1. Successive Doppler spectra are averaged to accurately emulate the noise in the recorded spectrum.

Fig. 4–3 illustrates an example of the DSS work, showing on the left the PSDs input to provide the spectra on the right, showing those created at various steps of the simulation process. Further analysis of the final spectrum can now be done the same way as for the measured spectra. Examples of the computed parameters are included in Fig. 4–3b.

4.3.2 Parameters Sensitivity to SNR and Velocity Resolution

The signal-to-noise ratio (SNR) and the Doppler velocity resolution are two parameters often used to describe the quality of a radar Doppler spectrum. Low SNR conditions can have a great impact in the uncertainty associated with the moment estimates, while low Doppler velocity resolution can greatly affect

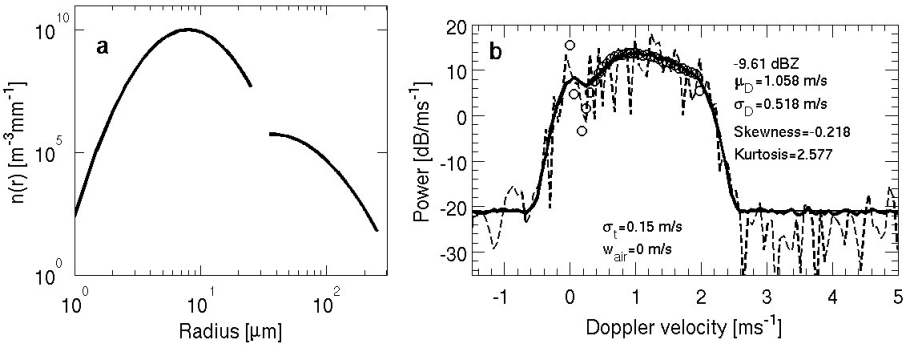

Figure 4–3: (a) Example of input cloud and drizzle PSDs. (b) The simulated radar Doppler spectrum at various stages, with the numbers on the right representing the computed values of five parameters (reflectivity, mean velocity, spectral width, skewness, and kurtosis) of the final spectrum (thick): the circles represent the ideal quiet-air spectrum (air characteristics are shown at the bottom); the thin continuous line is the noise-free turbulent spectrum; the dashed line is one noisy spectrum; and the thick line is the averaged noisy spectrum.

the accuracy of the moment estimates, especially for narrow spectra. Simulations over a wide range of SNR conditions and for different Doppler spectra velocity resolutions were performed to assess the noisiness of the skewness and kurtosis estimates (Fig. 4–4). A drizzle-only PSD with fixed logarithmic width ($\sigma_x = 0.40$) and increasing median radius (r_0: 20–70 µm) is used as a proxy of drizzle particles' growing contribution to the radar returned signal. The turbulence broadening term is fixed ($\sigma_t = 0.2\,\mathrm{m\,s^{-1}}$) in all simulations. For comparison, the theoretical values of skewness and kurtosis obtained from the expressions derived above (combining Eqs. 4.7, 4.8, 4.9, and 4.12) are also shown in Fig. 4–4 (thick gray dashed lines). SNR conditions equal to or higher than 0 dB are needed to get a reliable estimate of the moments. Similarly, Doppler velocity resolution better than $10\,\mathrm{cm\,s^{-1}}$ is required. The latter is achieved for both millimeter radar systems used in this study, while the former criterion is typically fulfilled when drizzle is present above the cloud base, which is the area of main interest here. The overall agreement of the analytical and simulated values of skewness and kurtosis is encouraging and

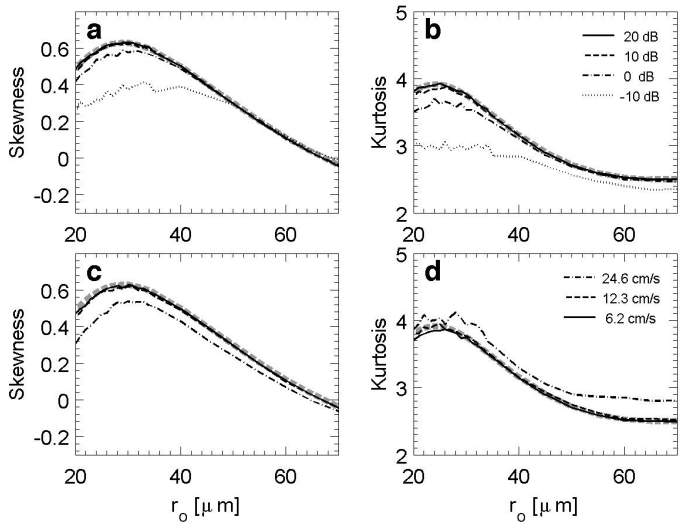

Figure 4–4: Effect of (a)–(b) the SNR (velocity resolution of $6.2\,\mathrm{cm\,s^{-1}}$) and (c)–(d) the Doppler spectrum velocity resolution (SNR of 10 dB) on the (a),(c) skewness and (b),(d) kurtosis estimates of simulated radar Doppler spectra. The thick dashed line represents the theoretical value predicted by the expression provided here, while the various continuous lines are values obtained from the simulated radar Doppler spectra.

suggests that the analytical expressions are capable of predicting the Doppler moments for a variety of microphysical and dynamical conditions. Extensive testing (not shown here) of the validity of the presented formulas against the simulator output has been performed with consistently good agreement.

4.4 Observations

Taking a closer look at the observed Doppler spectra parameters (e.g., Fig. 4–5) helps in our search of a critical measurement (or set of measurements) that could indicate the onset location of the drizzle formation. In fact, it hints toward the spectrum skewness usefulness: this parameter takes positive values near the cloud top (even slightly increasing downward), quickly decreases to negative values near mid-cloud, and remains negative down to the cloud base. This behavior is most obvious when drizzle is actually escaping the cloud , as the drizzle production was more effective. The spectrum kurtosis also seems

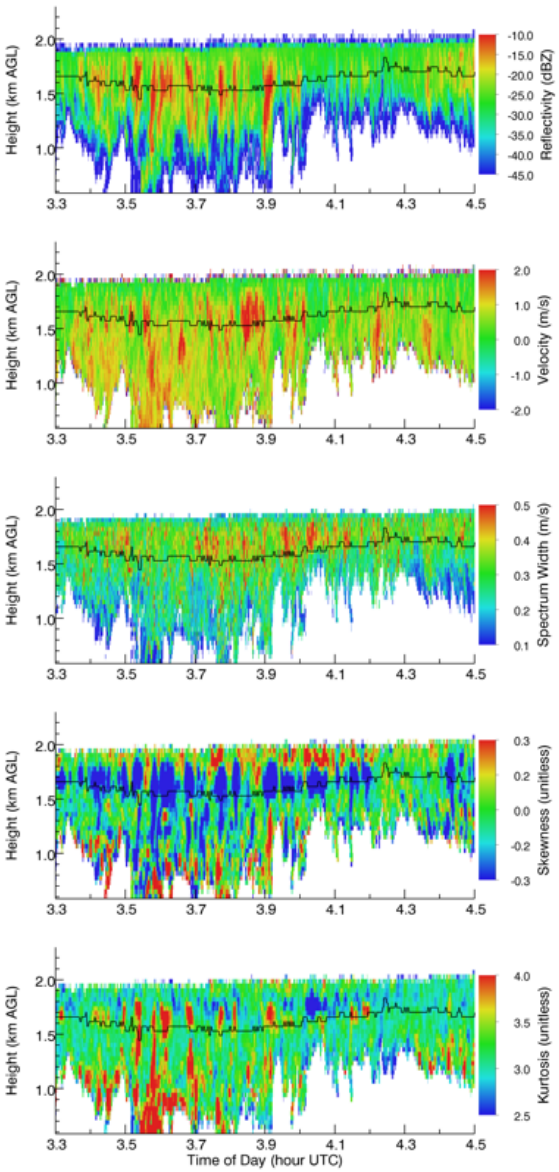

Figure 4–5: W-band radar Doppler spectra moments: (a) reflectivity, (b) mean Doppler velocity, (c) spectral width, (d) skewness, and (e) kurtosis at the ARM AMF Graciosa site during a 72-minute period. The black line represents the corresponding cloud base as detected by a co-located Vaisala ceilometer. (Courtesy of E. Luke, from Brookhaven National Laboratory.)

to have a preferred behavior when drizzle is falling, but it is less obvious than for the skewness.

The change in spectra parameters with drizzle onset and growth is further characterized by investigating the distributions of their values at various growth stages. Radar reflectivity values are used as a proxy for particle

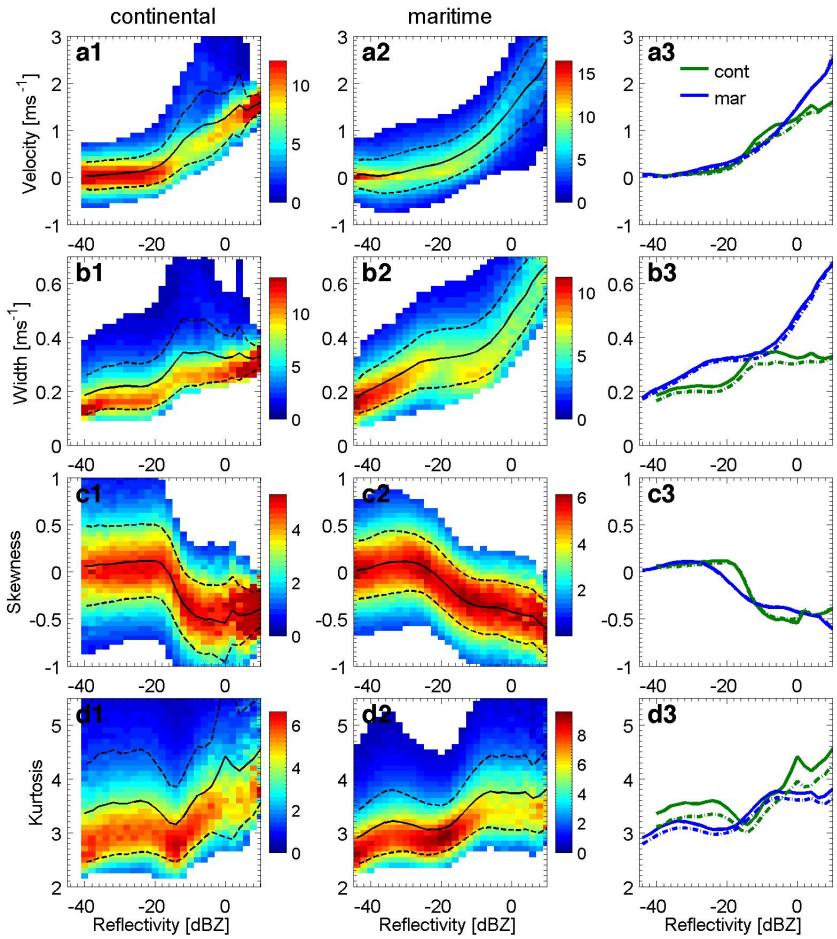

Figure 4–6: Histograms of observed radar Doppler spectra moments as a function of the cloud radar reflectivity from continental (ARM SGP; left) and maritime (ARM AMF/Graciosa; center) locations: (a) mean Doppler velocity, (b) spectrum width, (c) skewness, and (d) kurtosis. The colors represent the percentage of the data found in a 2-dB reflectivity bin with the corresponding moment's value, while the black lines represent the mean (solid) and standard deviation (dashed) of each distribution. Panels (a3)–(d3) compare the mean (solid) and median (dashed-dotted) found in continental (green) and maritime (blue) clouds.

growth, as it is mostly sensitive to their size rather than number concentration (Rayleigh regime). The results are shown in Fig. 4–6, including only measurements made above the cloud base detected by the lidar, and collected from about a dozen single-layer stratocumulus cases. Although the observations are collected over a wide range of atmospheric conditions, the distributions exhibit systematic variability and trends.

First, the observations show that the usual reflectivity threshold used to determine the presence of precipitation (typically between −20 and −15 dBZ) reflects better the dominance of precipitation particles over cloud droplets in the Doppler spectrum, as indicated by a near-zero skewness and minimum in kurtosis. These are characteristics of a symmetric, broad and flat spectrum, which can be obtained by the superposition of two spectra with similar strength, and a slight offset in their mean. This had also been hinted by Liu et al. (2008), as they drawn their conclusions using a theoretical threshold function that represents that change in dominance. The reflectivity value at which this happens is varying over the various cases (as shown by the range of reflectivity values where the change occurs), most likely due to variations in the number concentration of cloud nuclei (Liu et al., 2008). Nevertheless, as proposed by Liu et al. (2008), this transition occurs over a narrow range of reflectivity values, especially in the continental data set, where the number concentration is expected to vary less.

More importantly here, the observations in Fig. 4–6 indicate that the skewness of the radar Doppler spectrum alone can be a nice indicator of the onset of the precipitation formation. In fact, it is even more sensitive to the presence of precipitation-size particles than other parameters (reflectivity, mean velocity, spectral width...), showing their presence at reflectivity values as low as −40 dBZ, through an increase in skewness with reflectivity (growth proxy).

The greater velocities reached by the drizzle particles (even the early ones) explain this systematic change. It creates a small tail at the right of the Doppler spectrum peak (thus positive skewness) that is detected due to the high sensitivity of the WACR, and the dependence of the return on the sixth power of the size. Consequently, the early formation of precipitation

drops can be located using simply the cloud radar Doppler spectra skewness, and the full retrieval of microphysics and dynamics is only needed in areas surrounding these locations to investigate further the early growth of drizzle.

Other interesting features in Fig. 4–6 are the several distinct differences between the maritime and continental distributions of Doppler spectrum width. For instance, a steady increase of the Doppler spectrum width (from 0.15 to $0.3\,\mathrm{m\,s^{-1}}$) is observed at low radar reflectivities. Since there is no reason to expect a systematic increase of in-cloud turbulence with radar reflectivity, the observed increase is attributed to microphysical factors. It clearly indicates that drizzle particles exist in maritime clouds at very low reflectivities. The other differing region worth noting is within the reflectivity regime higher than about 0 dBZ. While the average spectrum width in the continental clouds remains almost constant, in the maritime clouds the observations show a significant increase of the spectrum width with reflectivity. In that same regime, the maritime clouds show greater Doppler velocities and the skewness gets more negative than in continental clouds, on average. These discrepancies will be examined using modeling in the next section.

4.5 Interpretation of the Observations

To further our understanding of the observed trends in Fig. 4–6, a simplified approach was used to simulate the growth of drizzle in a typical cloud during its early stage and later on when it is well developed.

The evolution of the drizzle PSD within a cloud layer is represented by its decomposition into individual spectra originating from the autoconversion process at different levels. With some simplifying assumptions about the microphysical growth processes, the approximate evolution of an individual drizzle PSD as a function of distance fallen is obtained from a general equation describing PSD development under steady-state conditions. In our simplified

approach, the formation rate of embryonic drizzle droplets via the autoconversion process is not calculated explicitly. The shape of the initial drizzle PSD is prescribed, but its total number concentration is estimated from the formation rate of embryonic drizzle, which is parameterized as a function of the assumed cloud droplet number concentration and LWC profile at/above a level at which the PSD is introduced.

Starting from a specified drizzle PSD at a level z_0, its evolution while it is falling under steady-state conditions, within a region where the number of drops in the spectrum is conserved, follows this general relation:

$$\frac{\partial n_d(r,z)}{\partial t} = 0 \quad \Longrightarrow \quad \frac{\partial}{\partial r}\left(n_d \frac{\mathrm{d}r}{\mathrm{d}t}\right) + \frac{\partial}{\partial z}\left(n_d \frac{\mathrm{d}z}{\mathrm{d}t}\right) = 0, \tag{4.15}$$

where $n_d(r,z)$ represents the drizzle PSD at level z. To meet its conditions, this relation neglects the introduction of new droplets by autoconversion, the self-collection, the breakup and the complete evaporation below the cloud base (Gossard et al., 1990; Rogers et al., 1991). The assumption that droplets fall vertically at their terminal velocity (no vertical and horizontal air motion) leads to $\mathrm{d}z/\,\mathrm{d}t = V_f$, with z oriented downwards. The air density correction term for fallspeed is not taken into account, as it is expected to have a much smaller effect than the other processes due to the short distances considered here.

The expansion of Eq. 4.15 gives the following partial differential equation:

$$\left.\frac{\mathrm{d}r}{\mathrm{d}t}\right|_{PRC} \frac{\partial n_d}{\partial r} + V_f \frac{\partial n_d}{\partial z} = -n_d \left[\frac{\partial}{\partial r}\left.\frac{\mathrm{d}r}{\mathrm{d}t}\right|_{PRC} + \frac{1}{V_f}\frac{\mathrm{d}V_f}{\mathrm{d}r}\left.\frac{\mathrm{d}r}{\mathrm{d}t}\right|_{PRC}\right]. \tag{4.16}$$

The term $\left.\frac{\mathrm{d}r}{\mathrm{d}t}\right|_{PRC}$ describes the growth rate of the droplets due to microphysical processes PRC. The analytical solution of Eq. 4.16 is obtained assuming that, in a given layer, the evolution of the drizzle PSD is mainly through one microphysical process (e.g., accretion) described by a unique power law ($\left.\frac{\mathrm{d}r}{\mathrm{d}t}\right|_{PRC} = Ar^B$), and with the sedimentation parameterized by a uniquely

prescribed power law velocity-size relationship applied for an entire subrange of sizes of interest ($V_f = \alpha r^{\beta}$):

$$n_d\left(r,z\right) = f_{r,z}^{\beta+B} n_0\left(f_{r,z}\cdot r, z_0\right), \tag{4.17a}$$

$$\text{with } f_{r,z} = f_{r,z}\left(r,\Omega,B,\alpha,\beta\right) = \left[1+\frac{B-\beta-1}{\alpha}\Omega r^{B-\beta-1}\right]^{-1/(B-\beta-1)}, \tag{4.17b}$$

where $n_0(r,z_0)$ is an initial PSD at the initial level z_0, and Ω is the integrated value of A (introduced in the power law of the growth process) from z_0 to a level below at z.

The relation 4.17a shows that the drizzle PSD at a level z can be described by the initial distribution at z_0 displaced along the radius axis by an amount $\Delta r = r\cdot(f_{r,z}-1)$. Moreover, the number concentration changes by a multiplication factor of $f_{r,z}^{\beta+B}$. The input PSD spectra are assumed to take the form of an analytical function such as lognormal.

Inside a cloud, $n(r,z)$ is composed of the cloud and drizzle modes. The cloud mode contribution is calculated assuming that the cloud droplets follow a lognormal distribution (Eq. 4.1) with a prescribed $\sigma_{x,c}$ and N_c, varying for maritime and continental clouds. The characteristic size $r_{0,c}$ is determined at each level from the cloud LWC profile, which is prescribed in the form $LWC(z) = f_{ad}LWC_{ad}(z)$. The adiabaticity factor f_{ad} is calculated using the function proposed by Wood et al. (2009) or Chin et al. (2000).

The cloud LWC and droplet number concentration are also used to estimate the number concentration autoconversion rate (Wood, 2005b), allowing the evaluation of the injected total number concentration of the initial distributions for each individual drizzle PSD. Once the first drizzle particles are formed, they grow via the cloud droplet collection process called accretion (ACC). It can be expressed as a function of the cloud LWC only, and two

regimes can be identified: one for the early stage of collectional growth describing the growth of drizzle embryos freshly transferred from the cloud to the drizzle category (*ACC1*), and one for the well-developed drizzle representing continuous accretional growth (*ACC2*). This differentiation comes from the collection efficiency: it is small for the initial embryos and quickly increases as the drops grow, eventually becoming mostly size-independent when drops reach a radius of 50–60 µm (e.g., Rogers and Yau, 1989). To keep things mathematically simple here, we use Long's (1974) approximation of the collection kernel $K(r, r_c)$ for a drizzle drop of radius r collecting cloud droplets of radius r_c:

$$K\left(r, r_c\right) \approx a_\kappa r^{3\kappa}. \tag{4.18}$$

For small drizzle drops ($r < 50\,\mu\text{m}$; *ACC1*), $\kappa = 2$ and $a_\kappa = 1.93 \times 10^{17}\,\text{m}^{-3}\,\text{s}^{-1}$, while for large drizzle drops ($r \geq 50\,\mu\text{m}$; *ACC2*), $\kappa = 1$ and $a_\kappa = 2.65 \times 10^{4}\,\text{s}^{-1}$. Note that Long's kernel is independent of the collected cloud droplets size. Following Eq. 4.18, the two accretional growth processes can be expressed as:

$$\left.\frac{\mathrm{d}r}{\mathrm{d}t}\right|_{ACC} = \frac{1}{4\pi\rho_w r^2}\int_{r_{min}}^{r_{max}} K\left(r, r_c\right) m\left(r_c\right) n\left(r_c\right)\,\mathrm{d}r_c = \frac{a_\kappa}{4\pi\rho_w} LWC r^{3\kappa-2}, \tag{4.19}$$

where ρ_w is the liquid water density, $m(r_c)$ and $n(r_c)$ are the cloud mass and PSD respectively, and LWC is their combined integral denoting the cloud liquid water content. Both *ACC* regimes have the same dependence on the cloud LWC. However, their dependence on the collecting drop's size differentiates them: a fourth-power dependence is found for the *ACC1* growth rate, while the *ACC2* growth rate is directly proportional to the collecting drop's size. Note that the *ACC1* regime is similar to the so-called "large cloud droplet mode" in the bulk parameterization of Saleeby and Cotton (2004). On the other

hand, the *ACC2* regime relates to the larger drizzle droplets present at more considerable distances from the level of their generation via autoconversion.

The distinction between two regimes with respect to cloud accretion by drizzle is maintained with respect to the velocity power law. In general, the terminal velocity for droplets smaller than about 30 µm in radius is represented with $\beta = 2$ (the Stokes regime), while the value of β progressively decreases for larger droplets, becoming close to 1 for r around 60–80 µm. Here, two different power law relationships for terminal velocity are used, which better approximate separately the very small drizzle droplet regime (*ACC1*, with $\beta = 2 - \delta$ and $0 < \delta < 1$ [in the model: $\alpha = 7.637 \times 10^5\,\mathrm{m}^{-0.5}\,\mathrm{s}^{-1}$, $\beta = 1.5$]) and the one for larger drops (*ACC2*, with $\beta = 1 + \delta$ and δ positive but close to 0 [in the model: $\alpha = 4.538 \times 10^4\,\mathrm{m}^{-0.2}\,\mathrm{s}^{-1}$, $\beta = 1.2$]).

This artificial separation of the accretion process in two distinct regimes, each with unique power law relationships for accretional growth and terminal velocity, allows the use of Eq. 4.17 in the analytical study of the drizzle spectrum evolution when controlled mainly by one of the two regimes. Eq. 4.17b can now be approximated by:

$$f_{r,z} \approx \left[1 - \frac{\Omega}{\alpha} r^{1+\delta}\right], \text{ for the } ACC1 \text{ process,} \tag{4.20a}$$

$$f_{r,z} \approx \left[1 - \frac{\Omega}{\alpha r^{1+\delta}}\right], \text{ for the } ACC2 \text{ process,} \tag{4.20b}$$

with Ω proportional to the LWP of the layer between z_0 and z, with a different constant for each *ACC* process. Therefore, for small drizzle drops (*ACC1* process), the PSD at z represents the initial PSD displaced by $\Delta r \approx -\Omega r^{2+\delta}/\alpha$ and multiplied by the factor $f_{r,z}^{6-\delta} \approx 1 - (6 - \delta)\Omega r^{1+\delta}/\alpha$. Consequently, for small Ω, only a very tiny change with respect to the initial PSD is expected for the small r considered ($\Delta r \to 0$, $f_{r,z}^{6-\delta} \to 1$), resulting from a very slow growth by accretion at these sizes. However, the PSD modification increases

relatively rapidly with increasing r, as we can expect from rapidly rising collection efficiency and velocity. It leads to a broadening of the PSD due to a progressive advancement of the larger droplet tail towards increasing r.

A different evolution of the individual drizzle PSD is expected for drizzle that is already developed and grows by a continuous cloud accretion *ACC2*. For a size-velocity relationship almost linear ($\delta \approx 0$), the modified PSD is obtained by a translation of the initial PSD that is size-independent, $\Delta r \approx -\Omega/\alpha$, and by the multiplication factor $f_{r,z}^{2+\delta} \approx 1 - 2\Omega/(\alpha r)$, representing the reduction of the concentration decreasing slowly with increasing r.

Some error in our modeling of the drizzle evolution under the accretion of cloud droplets is introduced due to:

1 the neglecting of the effects of the growth by condensation, which may have some small impact on the evolution of the smaller droplet tail;

2 the assumption about zero air motion;

3 the neglecting of a turbulence effect;

4 the neglecting of the self-collection process.

The error introduced by first three assumptions is important mostly for the small drizzle droplets growing under the *ACC1* regime, while the fourth factor is expected to be important mainly for heavily drizzling cases.

In this study, the final contribution of the drizzle mode to the full PSD is represented as a superposition of PSDs injected progressively at different levels, to represent the autoconversion process. The evolution of each of these distributions is calculated independently according to Eq. 4.17 starting from the injection level proper for each distribution. This evolution is based on the assumption that the unique power law relations for terminal velocity and growth rate are valid for the whole distribution. Since these power laws are a good approximation over a limited range of droplet sizes only, the contribution

of the droplets that are outside of the corresponding subrange must be insignificant for the simulated layer. This imposes a limitation for the size domain of the initial PSDs and the vertical extension of the studied cloud layer.

The output total cloud and drizzle PSDs are then fed into the DSS to emulate the observations of these PSDs by a millimeter Doppler radar. Two main behaviors noticed in the observations are further studied here: the early growth of drizzle particles (low reflectivity values), and the continuous growth of a well-developed drizzle PSD.

4.5.1 Early Drizzle Growth

Taking a cloud layer near cloud top, where the first drizzle precursors are generated by autoconversion, the parameterization for *ACC1* can be applied since we can assume the absence of larger droplets. A fallen distance of 40 m is considered sufficiently small to have not yet generated the larger droplets for which the kernel and velocity parameterizations are no longer valid. This growth represents the transition regime described in section 4.4, where the drizzle begins to affect the parameters of the Doppler spectrum.

Starting from the uppermost level of the layer, a new distribution of droplets freshly transferred to the drizzle category is introduced every 5 m to account for the production of drizzle by autoconversion active in the whole layer. Each of them will then fall slowly, evolving according to Eq. 4.17a with Eq. 4.20a. The curves presented in Fig. 4–7a show the total predicted PSD every 10 m, each line representing the sum of the cloud PSD and of all the drizzle PSDs that are input above or at a given cloud level (and that have evolved until reaching that given cloud level). As predicted by Eq. 4.17a given Eq. 4.20a for an individual PSD, the changes are rather small for smaller drizzle droplets and increase progressively with r, changing the slope of the bigger sizes in the drizzle PSD. This effect is amplified in the Doppler spectrum simulated by the

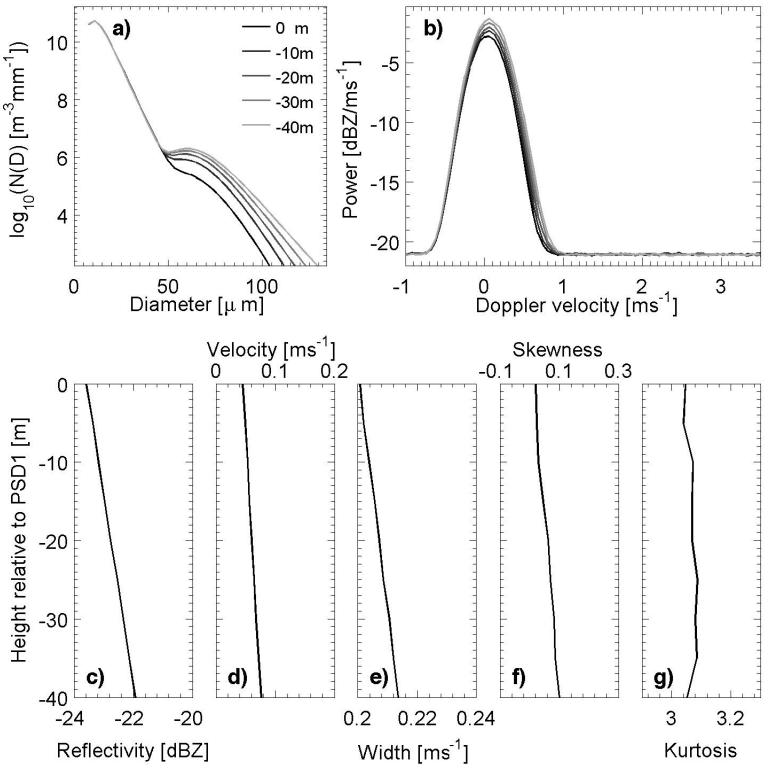

Figure 4–7: (a) Evolution of the continental PSDs near the cloud top, as modeled considering only the *ACC1* process. (b) Simulated radar Doppler spectra corresponding to those PSDs, where no air motion and a turbulence width of $0.2\,\mathrm{m\,s^{-1}}$ were assumed. (c)–(g) Evolution of the five considered Doppler spectrum parameters, as computed by the simulator.

DSS (Fig. 4–7b), with the right side of the peak gradually moving towards more positive velocities while the left side barely shows any changes. The lower panels (Fig. 4–7c–g) present the vertical evolution of the corresponding five Doppler spectrum parameters.

This example has been obtained assuming continental cloud conditions. It should then describe the average behavior observed around -24 to $-22\,\mathrm{dBZ}$ for the continental cases shown in Fig. 4–6. In fact, the results visually compare well for the first three parameters (velocity, width and skewness): in both the model and observations, they present a slow increase as the drizzle grows (i.e., as the reflectivity increases and the drizzle impact on the Doppler spectrum becomes more apparent). Moreover, the simulated values are close

to the observed ones. As for the kurtosis, no clear behavior can be drawn from either the observations or the simulations in that range of reflectivities. Nonetheless, an average value above three was found, which relates well with the observations.

4.5.2 Well-Developed Drizzle: Marine Vs. Continental

The presence of heavy drizzle in deep clouds (marked by reflectivity higher than about 0 dBZ) completely dominates the Doppler spectrum, and different tendencies with increasing reflectivity can be noticed for continental and maritime clouds as discussed in section 4.4. The Doppler velocity increases more rapidly in maritime than in continental clouds, with a spectrum broadening observed only in the maritime clouds. This broadening is even accompanied by the skewness becoming more negative, while it stays rather constant for the continental clouds.

To have some insight into the microphysical causes of the observed differences, we perform the calculations of the spectra evolution within two clouds having the same constant LWC but with different droplet number concentrations: $100\,\mathrm{cm}^{-3}$ and $500\,\mathrm{cm}^{-3}$ for maritime and continental, respectively. In both cases, the first drizzle PSD at the layer top produces similar reflectivity (just above 0 dBZ), but with slightly larger Doppler velocity in the maritime clouds to be in agreement with the climatology shown in Fig. 4–6. Every 40 m, a new drizzle PSD is introduced to simulate the formation of new drizzle drops through the still active autoconversion of cloud droplets. All the initial spectra are assumed to be already sufficiently developed to be described by the *ACC2* parameterization. This means that we neglect the development of the drizzle droplets newly generated just at and above a given level that evolves via *ACC1*, explaining the greater introduction distance in this case. The results are shown in Fig. 4–8.

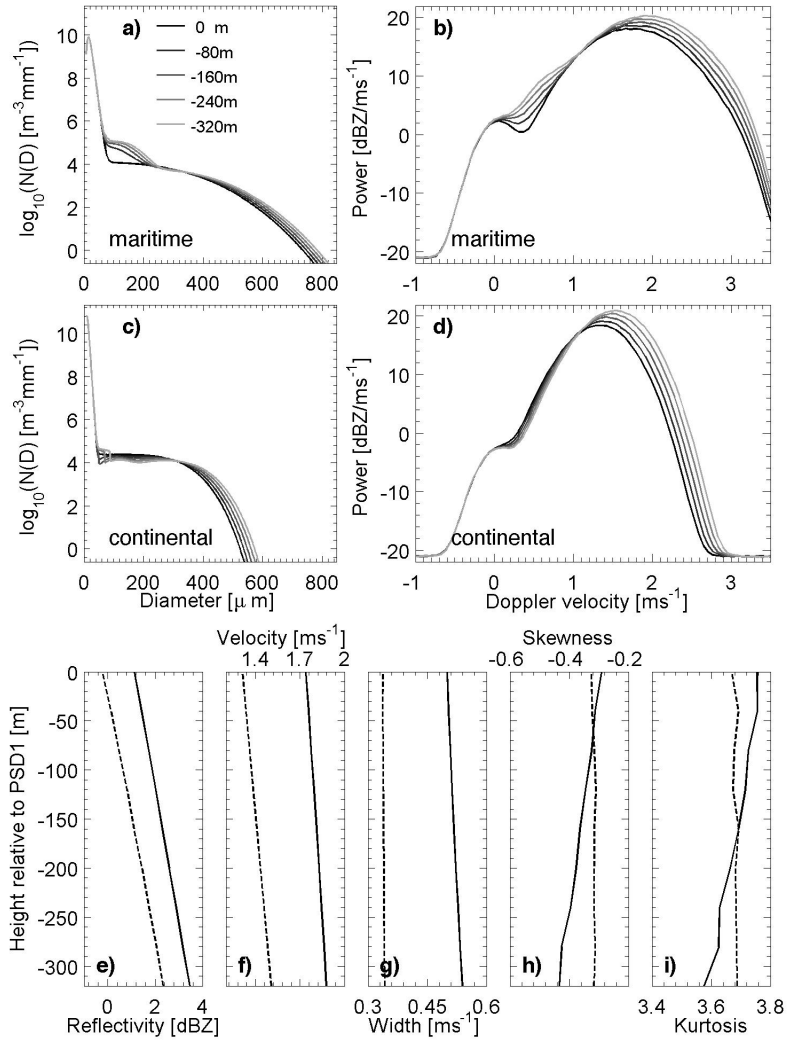

Figure 4–8: (a),(c) Evolution of the maritime and continental PSDs, respectively, when drizzle is well developed in the cloud, as modeled considering only the *ACC2* process. (b),(d) Simulated radar Doppler spectra corresponding to those PSDs, where no air motion and a turbulence width of $0.2\,\mathrm{m\,s^{-1}}$ were assumed. (e)–(i) Evolution of the five considered Doppler spectrum parameters, as computed by the simulator, for the maritime (solid) and continental (dashed) PSDs.

The main difference is in the intensity of the introduced PSDs within the simulated cloud layer: almost negligible in the continental case and much more important in the maritime. This difference results from the dependence of the autoconversion rate of the number concentration on the cloud droplet concentration prescribed for the two clouds. The growth of the PSD and the Doppler spectrum evolution at the larger droplet tail is very similar in the two

cases since the accretional growth is mainly a function of the cloud LWC, and identical for both. However, the continuous addition to the initial spectrum of the new spectra due to the autoconversion still active in the maritime clouds, leads to a continuous increase of the total spectrum width and a skewness growing more negative, while these two parameters are constant throughout the continental growth (see Fig. 4–8g–h), as observed previously in Fig. 4–6.

Nevertheless, a more rapid increase of mean Doppler fall velocity with radar reflectivity in the maritime than in the continental clouds is not obtained. This increase could be a consequence of the formation of larger droplets via the self-collection between drizzle droplets, not taken into account in the simulated PSD evolution. Using the proposed parameterization of self-collection (Beheng, 1994), the average rate of self-collection in our simulated maritime case is about $0.1\,\mathrm{m^{-3}\,s^{-1}}$. Assuming an average velocity of $1\,\mathrm{m\,s^{-1}}$, a rough estimation then gives 10 collision events during a fall of 100 m. An enhancement of the self-collection ratio can occur from turbulence and also an increase of collision probability can be expected due to a rather wide PSD of drizzle in the maritime case.

4.6 Summary

The recording of the full radar Doppler spectrum is now a common approach in profiling millimeter radars, and is certainly the standard for all ARM profiling radars since 2004. The argument for recording the full radar Doppler spectrum, despite its impact on data volume, is our belief that the decomposition of the radar return as a function of observed Doppler velocities offers new opportunities for the study of cloud and precipitation microphysics and dynamics. This potential needs to be exploited systematically, especially in simple cloud systems such as liquid stratiform drizzling clouds. A proposed

method for accomplishing this is through the careful use of radar Doppler spectra forward modeling and 1-D microphysical modeling.

This chapter summarizes modeling work done to demonstrate the possibilities of the cloud Doppler spectra. A new, comprehensive approach for using radar Doppler spectra observations in liquid clouds that contain drizzle droplets is introduced. We argue that cloud radar Doppler spectra are usually highly asymmetrical (non-Gaussian) and thus contain information about the cloud microphysics and dynamics. In addition to the usual three parameters of the radar Doppler spectrum (reflectivity, mean Doppler velocity and spectral width), two other parameters (skewness and kurtosis) are introduced to describe its shape.

The link between cloud/drizzle microphysics, dynamics and radar observables is accomplished with two complementary methods. First, analytical relationships that link all five radar Doppler spectra parameters to cloud microphysics and air dynamics are presented. The analytical relationships are used to explore the behavior of the five parameters for a variety of dynamical and microphysical conditions, and especially their behavior during drizzle onset and subsequent growth, although not all the analysis done is included here. In addition, a radar Doppler spectrum forward model is presented. The forward model is tuned for the ARM cloud radar characteristics and its input are detailed cloud and drizzle PSDs, and information about the air motions within the radar sampling volume. The forward model allows microphysical model output to be linked with radar observations. Also, the generality of the proposed relationships between cloud microphysics, dynamics and radar observables was validated using the forward model.

It was established that the skewness of radar Doppler spectra is very sensitive to the development of a weak spectral bump at the higher fall velocity

side of the radar Doppler spectrum. Such small spectral bumps result from the autoconversion process that leads to drizzle onset in warm clouds. Thus, skewness is recommended as a more sensitive indicator of early drizzle onset rather than radar reflectivity or Doppler velocity, which are sensitive only when the drizzle contribution to the total observed reflectivity is significantly larger than the cloud contribution.

Furthermore, comprehensive radar observations obtained during stratocumulus coverage in continental and maritime environments are presented and compared to illustrate the presence of a systematic behavior in the transition regime from cloud-only to drizzling cloud observations. The observed trends of the radar Doppler spectra moments as a function of radar reflectivity exhibit several similarities. However, a few noticeable differences were found and successfully explored using microphysical modeling.

The transformation of the microphysical model output to radar Doppler spectrum and related radar observables (e.g., spectrum width and skewness) offers a methodology for interpreting radar observations and for improving microphysical modeling. This closed loop process offers new venues for examining cloud microphysics and dynamics at very small scales. The continuous recording of radar Doppler spectra from all the profiling cloud radars makes such observations widely available to the scientific community.

Chapter 5
Radar-Radiometer Retrievals of Number Concentration and Dispersion Parameter in Marine Stratocumulus

Chapter 4 demonstrated that, although drizzle particles are ubiquitous in marine stratocumulus clouds, their contribution to the radar measurements remains small during their early development, especially for the reflectivity and mean Doppler velocity. Such occasions can be noticed when no drizzle shaft is actually detected below the cloud base and the reflectivity increases with height. Two such cases of a few hours each were present in the data set of stratocumulus selected in chapter 3, and they offer opportunities to test methods to retrieve information about the cloud PSD. Chapter 4 also showed that the radar Doppler spectra moments provide insights on the microphysical properties inside sampled volumes. This chapter now revisits a retrieval method developed in the 1990s. A cloud condensational model is added to constrain the retrieval algorithm, making use of the derivative of the radar reflectivity profiles. Steady-state conditions are assumed to be maintained inside the cloud away from the edges. This allows the removal of some limiting assumptions that were originally needed. Consequently, all parameters of a lognormal cloud PSD are now retrieved.

This chapter is based on an early version of a manuscript submitted to Atmospheric Measurement Techniques:

Rémillard, J., P. Kollias, and W. Szyrmer, 2012: Radar-radiometer retrievals of number concentration and dispersion parameter in marine stratocumulus. *Atmos. Meas. Tech. Discuss.*, **5**, 7507–7533, doi:10.5194/amtd-5-7507-2012.

5.1 Introduction

Extensive sheets of stratus and stratocumulus clouds lie above the eastern boundary current upwelling regions over the world's oceans (Klein and Hartmann, 1993). Marine stratocumulus clouds play a critical role in the boundary layer dynamics and are a key component in Earth's radiation budget (Randall et al., 1984; Ramanathan et al., 1989; Bony and Dufresne, 2005). However, appreciable complexity and challenges are found on smaller space and time scales, including the cloud-scale (Stevens and Feingold, 2009). If all other parameters are fixed, an increased aerosol concentration may reduce cloud droplet sizes for a fixed liquid water content, and therefore increase cloud optical thickness (the *Twomey effect*, Twomey, 1977). In turn, reduced cloud droplet sizes can lead to precipitation suppression and increase the cloud lifetime (the *Albrecht effect*, Albrecht, 1989). However, recent modeling studies have suggested that elevated CCN concentrations can also affect entrainment of free tropospheric air in the marine boundary layer (e.g., Ackerman et al., 2004), thus leading to important feedbacks that include both key processes.

Providing observational constraints for these processes at the cloud-scale requires coordinated multi-synergistic, multi-platform measurements. In situ aircraft-based observations provide direct measurements of cloud thermodynamical and microphysical properties, but are temporally and spatially limited. Ground-based supersites (e.g., Ackerman and Stokes, 2003) offer the advantage of continuous, multi-instrument observations. Relating the ground-based measurements to the variables of interest requires the use of physical or statistical retrieval techniques (e.g, Turner et al., 2007). Here, we are concerned with the retrieval of microphysical properties of non-precipitating stratocumulus clouds where condensation in an updraft and evaporation due to cloud-top

mixing are the key processes that determine the profile of cloud microphysical properties.

Several previous studies have focused on the retrieval of microphysical processes in marine stratocumulus (Frisch et al., 1995, 1998, 2002; Fox and Illingworth, 1997; Kato et al., 2001; Turner et al., 2007). Frisch et al. (1998) first introduced the combination of radar-radiometer measurements to retrieve the in-cloud profile of liquid water content. The presence of drizzle limits the applicability of the technique, and either the use of a radar reflectivity threshold (e.g., Liu et al., 2008) or the absence of radar echoes below the cloud base is used to remove drizzling clouds. In the absence of radiometer measurements, a variety of regression-based power law relations between the radar reflectivity factor and the liquid water content have been proposed (Atlas, 1954; Sauvageot and Omar, 1987; Fox and Illingworth, 1997; Wang and Geerts, 2003; Sassen and Liao, 1996; Kogan et al., 2007). The review paper of Turner et al. (2007) shows the large differences among the state-of-the-art liquid water content retrievals in nonprecipitating thin liquid clouds. Cloud optical depth measurements have also been used to constrain the microphysical retrievals in stratocumulus clouds (Dong et al., 1997; Mace and Sassen, 2000; Kim et al., 2008; McComiskey et al., 2009). More recently, Martucci and O'Dowd (2011) developed a new technique to retrieve warm cloud microphysics combining radar profiles to extrapolated lidar profiles.

A new retrieval method is developed here, building on the previous retrieval technique introduced by Frisch et al. (1995, 1998, hereafter F95+) that used the combination of radar and radiometer measurements. Assuming that condensation and evaporation are the only processes controlling the evolution of the cloud particle size distribution (PSD), the vertical gradient of the

attenuation-corrected radar reflectivity of the cloud is used to derive the dispersion parameter (σ, assumed constant in the column) and the number concentration (N_{cld}, allowed to vary vertically around the derived column-averaged value). The observed mean Doppler velocity is used as a proxy for the vertical air motion and it is used to estimate the supersaturation in the cloud.

This paper first briefly describes the typical instruments available. The novel approach is then described and illustrated by two nondrizzling examples from the Azores. Finally, the results are compared to another instrument's measurements, to assess the feasibility of this technique.

5.2 Observations

The study utilizes marine stratocumulus observations collected during the recent deployment of the US Department of Energy Atmospheric Radiation Measurement (ARM) Mobile Facility (AMF) at the Graciosa Island, Azores, in the context of the Clouds, Aerosol and Precipitation in the Marine Boundary Layer (CAP-MBL) field campaign. CAP-MBL took place from April 2009 to December 2010 in the Azores, to collect data on the physical and radiative properties of low-level clouds. The analysis is limited to low-level nonprecipitating marine stratocumulus clouds without any other higher-level clouds.

Measurements from the W-band ARM Cloud Radar (WACR), two 2-channel microwave radiometers (MWR), the ceilometer, and the 2-channel Narrow Field-of-View radiometer (NFOV) are used in this study (Table 5–1). Time series measurements of column-integrated amounts of precipitable water vapor (PWV) and liquid water path (LWP) are provided from the MWRs. The uncertainty in the MWR-retrieved LWP is typically better than $20\,\mathrm{g\,m^{-2}}$, depending on the retrieval method (Turner et al., 2007). Cloud optical depth τ_{NFOV} measurements are available from the NFOV at 1-s resolution (Chiu et al., 2006). Subsequently, the column-integrated cloud effective radius r_e can

Table 5–1: Cloud properties measured or derived from ARM observations in the Azores.

Measured quantity	Variable	Instrument
Radar reflectivity	Z ($\mathrm{mm^6\,m^{-3}}$)	WACR
Cloud top height	h_{TOP} (m)	WACR
Cloud base height	h_{BASE} (m)	Ceilometer
Cloud vertical air motion	w_{air} ($\mathrm{m\,s^{-1}}$)	WACR
Cloud liquid water path	LWP ($\mathrm{g\,m^{-2}}$)	MWR
Cloud optical depth	τ_{NFOV}	NFOV

be estimated from the τ_{NFOV} and LWP (e.g., Wood and Hartmann, 2006) using the expression $r_e = 9LWP/(5\rho_w\tau_{NFOV})$. The ceilometer provides estimates of the cloud base height, and it is used in conjunction with the WACR data to ensure that the selected period contains no drizzle (WACR echoes below the cloud base).

The WACR provides information on the vertical structure of the marine stratocumulus clouds as depicted by the radar reflectivity (Z) and mean Doppler velocity (V_d) measurements. The WACR reflectivity profile is corrected for attenuation from water vapor and liquid (e.g., Meneghini, 1978; Matrosov et al., 2004). The Balloon-Borne Sounding System (BBSS) provides vertical profiles of both the thermodynamic state of the atmosphere, and the wind speed and direction. The MWR provides the PWV and LWP measurements required for the estimation of the water attenuations. It is assumed that the vapor is distributed exponentially in the column, according to the surface pressure and temperature, while the liquid gets distributed in the cloud layer using the Frisch et al. (1998) method. Water vapor and liquid produce a total two-way attenuation of 1–2 dB each, but oxygen attenuation remains negligible.

5.3 Retrieval Method

Typically, an analytical form is chosen to represent the cloud PSD such that only three parameters are introduced in the equations of the moments of the radar Doppler spectra: a characteristic size (e.g., effective radius), a dispersion parameter, and a concentration parameter. One of the widely used forms is the lognormal PSD:

$$n(r) = \frac{N_{cld}}{\sqrt{2\pi}\sigma r} \exp\left(\frac{-\left(\ln r - \ln r_0\right)^2}{2\sigma^2}\right), \tag{5.1}$$

where N_{cld} is the number concentration, r_0 the median radius, and σ the lognormal width (a measure of the PSD dispersionacross the sizes). Such a PSD form yields the following k^{th} moment (see F95+):

$$\int r^k n(r)\,\mathrm{d}r = N_{cld} r_0^k \exp\left(\frac{k^2}{2}\sigma^2\right). \tag{5.2}$$

The bulk quantities of distribution that represent physical quantities of interest are directly related to the moments of the cloud PSD. For instance, the liquid water content (LWC) relates to the third moment of the PSD, resulting in the following:

$$Q_c = \frac{4\pi\rho_w}{3}\int r^3 n(r)\,\mathrm{d}r = \frac{4\pi\rho_w}{3} N_{cld} r_0^3 \exp\left(\frac{9}{2}\sigma^2\right). \tag{5.3}$$

The radar reflectivity factor (Z) is proportional to the backscattering cross-section of the droplets, which in turn relates to the sixth moment of the PSD since droplets are much smaller than the radar wavelength. Therefore, Z can be written as:

$$Z = 2^6 \int r^6 n(r)\,\mathrm{d}r = 2^6 N_{cld} r_0^6 \exp\left(18\sigma^2\right). \tag{5.4}$$

Combining Eqs. 5.3 and 5.4, the dependence on one of the PSD parameters can be removed:

$$Q_c = \frac{\pi \rho_w}{6} \frac{\sqrt{N_{cld} Z}}{\exp\left(\frac{9}{2}\sigma^2\right)}. \tag{5.5}$$

The application of Eq. 5.5 requires that either drizzle particles are absent or their presence does not affect the radar reflectivity profile. Alternatively, a separation of the measured Z values into their cloud and drizzle parts would be sufficient.

Analysis of a large database of in situ measurements taken in marine stratocumuli suggests that the cloud concentration number and lognormal width tend to be approximately constant with height (e.g., Miles et al., 2000). The growth and broadening of the PSD with height generally observed are accounted by an increase in the mean size and in the standard deviation around the mean size. Their ratio, however, is usually constant with height, resulting in a constant lognormal width. Based on these observations, most aforementioned retrievals algorithms also treat N_{cld} and σ as invariant with height (e.g., Frisch et al., 1998). However, the vertical resolution of in situ measurements is usually coarse. Here, we only assume that σ is constant with height, and its value is estimated from the calculated column-averaged number concentration. To find the last quantity, we will require that the variations of N_{cld} around its column average remain small.

Integrating Eq. 5.5 throughout the cloud layer provides an equation for the LWP:

$$LWP = \frac{\pi \rho_w}{6} \frac{\langle N_{cld}^{1/2} \rangle}{\exp\left(\frac{9}{2}\sigma^2\right)} \int \sqrt{Z(z)}\, \mathrm{d}z, \tag{5.6}$$

where the angled brackets represent a column averaging, weighted by the square-root of reflectivity: $\langle N_{cld}^{1/2} \rangle = \frac{\int \sqrt{N_{cld}(z)} \sqrt{Z(z)}\, \mathrm{d}z}{\int \sqrt{Z(z)}\, \mathrm{d}z}$. With LWP measurements available through the MWR, inverting Eq. 5.6 allows the retrieval of the

column-averaged N_{cld}, albeit normalized by a function of the PSD dispersion:

$$N_{norm}^{1/2} \equiv \frac{\langle N_{cld}^{1/2} \rangle}{\exp\left(\frac{9}{2}\sigma^2\right)} = \frac{6LWP}{\pi\rho_w \int \sqrt{Z(z)}\,\mathrm{d}z}. \tag{5.7}$$

The derivation of the last relation is the same as in Frisch et al. (1998), but with the column-constant N_{cld} replaced with the column-averaged value $\langle N_{cld}^{1/2} \rangle$.

To estimate the N_{cld} at a given height from the calculated $N_{norm}^{1/2}$ in Eq. 5.7, we use the profile of vertical gradient of reflectivity. The vertical changes of reflectivity have to reflect the evolution of PSD via active microphysical processes. In the absence of precipitation processes, the cloud droplets are assumed to grow only by condensation (and evaporation) as they follow the air motions. As such, the changes in reflectivity values are simply linked to the condensation/evaporation process, neglecting the effect of changes in N_{cld} as the reflectivity is mostly sensitive to changes in the sizes (review Eq. 5.4). The condensation/evaporation process dictates that the particle size growth rate is described by the following equation (e.g., Rogers and Yau, 1989):

$$\frac{\mathrm{d}r}{\mathrm{d}t} = \frac{S - \frac{a}{r} + \frac{b}{r^3}}{r\,(F_k + F_D)}, \tag{5.8}$$

where r is the droplet's radius, t is the time, S is the degree of saturation, a and b are constants depending respectively on the curvature and solute of the droplet, and F_k and F_D are atmospheric factors accounting respectively for the thermal and diffusion effects. Once initial droplets are formed, the curvature and solute terms can usually be neglected, leaving a simple form for the droplet's growth (and evaporation if $S < 0$). The time coordinate here relates to the height coordinate (z) through the vertical air motion (w_{air}), as cloud droplets sizes remain small enough to produce only negligible fall speeds,

and Eq. 5.8 becomes:

$$\frac{\mathrm{d}r}{\mathrm{d}z} = \frac{S}{r w_{air}\left(F_k + F_D\right)}. \tag{5.9}$$

On the other hand, the radar reflectivity factor is given by Eq. 5.4. In its most common units (dBZ), at a given height, the reflectivity changes with height can then be written as:

$$\frac{\mathrm{d}\left(\mathrm{dBZ}\right)}{\mathrm{d}z} = \frac{4.34}{Z}\frac{\mathrm{d}Z}{\mathrm{d}z} = \frac{4.34}{\int r^6 n(r)\,\mathrm{d}r}\int 6r^5 \frac{\mathrm{d}r}{\mathrm{d}z} n(r)\,\mathrm{d}r. \tag{5.10}$$

Using Eq. 5.9 for the change of radius with height, we get:

$$\begin{aligned}\frac{\mathrm{d}\left(\mathrm{dBZ}\right)}{\mathrm{d}z} &= \frac{26.04S}{w_{air}\left(F_k + F_D\right)}\frac{\int r^4 n(r)\,\mathrm{d}r}{\int r^6 n(r)\,\mathrm{d}r} \\ &= \frac{26.04S}{w_{air}\left(F_k + F_D\right)}\frac{1}{r_0^2 \exp\left(10\sigma^2\right)},\end{aligned} \tag{5.11}$$

where a lognormal PSD has been used to estimate the integrals (see Eq. 5.2).

Finally, it is assumed that steady-state conditions are reached and maintained inside each sampled volume (excluding the edges). Therefore, a steady-state supersaturation will be used, as derived by Korolev and Mazin (2003):

$$S_{qs} = \frac{a_0 w_{air}\left(F_k + F_D\right)}{b_0 \int r n(r)\,\mathrm{d}r} = \frac{a_0 w_{air}\left(F_k + F_D\right)}{b_0 N_{cld} r_0 \exp\left(\sigma^2/2\right)}, \tag{5.12}$$

where a_0 and b_0 are variables depending on temperature and pressure (defined by Korolev and Mazin (2003), and summarized in appendix). A lognormal PSD was assumed to obtain the right-hand side part. Korolev and Mazin (2003) argued that this steady-state approximation holds in stratocumuli, except near the edges. Solving for the ratio S_{qs}/w_{air} in Eq. 5.12, and substituting it into Eq. 5.11, the relation for the reflectivity gradient becomes:

$$\frac{\mathrm{d}\left(\mathrm{dBZ}\right)}{\mathrm{d}z} = \frac{26.04 a_0}{b_0 N_{cld} r_0^3 \exp\left(\frac{21}{2}\sigma^2\right)}. \tag{5.13}$$

Notice that a dependence on the LWC appears in Eq. 5.13, although there is still a dependence on the dispersion parameter. Using Eqs. 5.4 and 5.7, the following relation is obtained:

$$\left[\frac{N_{cld}(z)}{\langle N_{cld}^{1/2}\rangle^2}\right]^{1/2} = \left\{\frac{208.32 a_0 N_{norm}^{1/6}}{b_0\sqrt{Z(z)}}\left[\frac{\mathrm{d}\,(\mathrm{dBZ})}{\mathrm{d}z}\right]^{-1}\right\}\langle N_{cld}^{1/2}\rangle^{-4/3}. \tag{5.14}$$

On the right-hand side, all variables measured or obtained from measurements are grouped inside the braces.

Eq. 5.14 still has two unknowns, but we can request that the profile of N_{cld} remains close to its column-averaged value, such that we search for the value of $\langle N_{cld}^{1/2}\rangle$ that minimizes the following integral:

$$\int \left|\sqrt{\frac{N_{cld}(z)}{\langle N_{cld}\rangle}} - 1\right| \mathrm{d}z$$
$$= \int \left|\left\{\frac{208.32 a_0 N_{norm}^{1/6}}{b_0\sqrt{Z(z)}}\left[\frac{\mathrm{d}\,(\mathrm{dBZ})}{\mathrm{d}z}\right]^{-1}\right\}\langle N_{cld}^{1/2}\rangle^{-4/3} - 1\right| \mathrm{d}z. \tag{5.15}$$

Note that, as mentioned earlier, some assumptions are not valid at the edges. Therefore, the integral here excludes these radar volumes. Nevertheless, the retrieved column-averaged N_{cld} is assumed to apply also to the rogue volumes such that the remaining of the approach can still be done.

Once a value is retrieved for $\langle N_{cld}^{1/2}\rangle$ the three PSD parameters follow from Eqs. 5.14 ($N_{cld}(z)$), 5.7 (σ), and 5.4 ($r_0(z)$). Then, the effective radius at each range gate can be calculated from:

$$r_e \equiv \frac{\int r^3 n(r)\,\mathrm{d}r}{\int r^2 n(r)\,\mathrm{d}r} = r_0 \exp\left(\frac{5}{2}\sigma^2\right). \tag{5.16}$$

By definition, the optical depth (τ) depends on the cloud PSD and the particles extinction cross-sectional area. For spherical droplets following a lognormal PSD with a column-constant width, τ in the visible light spectrum

Table 5–2: Cloud properties retrieved by the proposed method, or derived using the retrieved quantities.

Cloud property	Variable	Status
Column-averaged number concentration	$\langle N_{cld} \rangle$ (cm^{-3})	Retrieved
Number concentration	N_{cld} (cm^{-3})	Retrieved
Column-constant lognormal width	σ	Retrieved
Median radius	r_0 (µm)	Retrieved
Effective radius	r_e (µm)	Derived
Cloud optical depth	τ	Derived
Supersaturation	S_{qs} (%)	Derived

can be written as:

$$\tau = \iint 2\pi r^2 n(r)\,\mathrm{d}r\,\mathrm{d}z = 2\pi \exp\left(2\sigma^2\right) \int N_{cld}(z) r_0^2(z)\,\mathrm{d}z. \tag{5.17}$$

Now having an estimate of the cloud PSD parameters, we can retrieve that variable too. As other instruments also measure τ independently, it provides a point of comparison to assess the feasibility of the approach described above. Two instruments that routinely retrieve τ are used here. One is MODIS, onboard polar orbiting satellites Terra and Aqua, providing only point comparisons. The other is the NFOV (Chiu et al., 2006) ground-based nearby the other instruments in the Azores, providing time series comparisons.

A summary of the cloud properties retrieved and derived in this work is provided in Table 5–2.

5.4 Results

The method described above assumes that only cloud droplets contribute to the measurements. However, marine stratocumuli have a propensity to produce drizzle, and it was observed that drizzle particles are nearly always present to some degree (Kollias et al., 2011a). Therefore, the method is applied for two periods when drizzle was rarely detected under the ceilometer cloud base, both observed on Graciosa Island, in the Azores, during June 2010. It is

believed that the drizzle contributions to the WACR measurements in those cases are minimal.They are thus neglected here to demonstrate the possibilities of the new method. Its further application however requires the removal of the drizzle contribution to the measurements (Luke and Kollias, 2012).

5.4.1 Case of 13 June 2010

The first case is a stratocumulus cloud observed on June 13, 2010. Observed and retrieved parameters are shown for a two-hour daytime period (0930–1130 UTC; NFOV retrievals are available only during the day). No other cloud layer was observed during that period (e.g., cirrus), and no significant drizzle was falling from the stratocumulus (Fig. 5–1a). The radar reflectivity profile peaks near the cloud top, further supporting either the lack of drizzle particles or their negligible role in the WACR moments. The Doppler measurements (Fig. 5–1b) show many short-lived up and down movements going through the cloud, with amplitudes typically smaller than $1\,\mathrm{m\,s^{-1}}$. Near the end of the two-hour period, downdrafts became more dominant, and a thinning of the cloud is visible through the rising of the cloud base. Eventually the cloud dissipated in the afternoon. Overall, the cloud had a depth of 200–250 m, with a rather constant LWP and PWV (Fig. 5–1c).

The retrieved column-averaged number concentration $\langle N_{cld} \rangle$, the height-dependent N_{cld}, the column constant σ, and the height-dependent effective radius r_e and supersaturation S_{qs} are shown in Fig. 5–2. Relatively high cloud droplet number concentrations are retrieved (N_{cld} between 400 and $600\,\mathrm{cm^{-3}}$) with correspondingly small effective radius (r_e around 6 µm). Such values are typically found in continental stratocumuli (Miles et al., 2000). Azores is an inhabited island and the air masses have origins with variable aerosol loadings (Rémillard et al., 2012a). Furthermore, the retrieved values are consistent with the suppression of drizzle formation in that case.

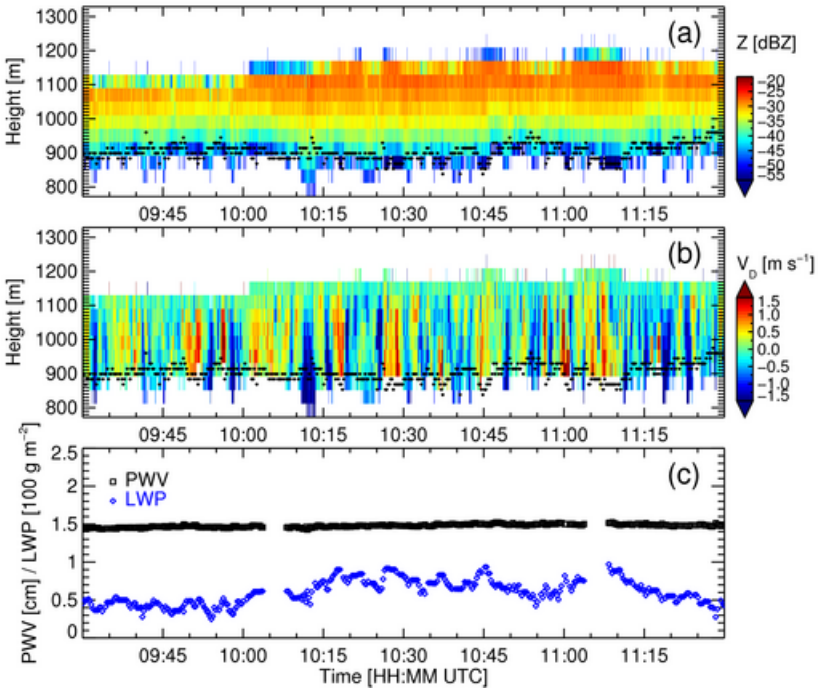

Figure 5–1: Measurements made over a two-hour period on 13 June 2010: (a) radar reflectivity factor, (b) mean Doppler velocity (positive values indicate upward motion), and (c) LWP (blue) and PWV (black) from the MWR. The black dots in (a),(b) represent the cloud-base height as measured by the ceilometer.

The retrieved σ values are varying between 0.2 and 0.4 (Fig. 5–2c). These values are in agreement with previous data sets, as reported by Miles et al. (2000), although in the lower half of the climatological estimated range. The low retrieved values of σ are consistent with the suggestion that the cloud droplets did not grow to drizzle sizes, keeping the PSD narrow. The supersaturation is estimated using Eq. 5.12. The WACR Doppler velocity measurements are assumed to represent well w_{air}, as no significant drizzle was detected and cloud droplets have fall velocities smaller than the radar resolution (a few $\mathrm{cm\,s^{-1}}$). The resulting S_{qs} field has values within 0.1 % (see Fig. 5–2e). The S_{qs} retrieved field seems reasonable, although very few in situ measurements are available to compare.

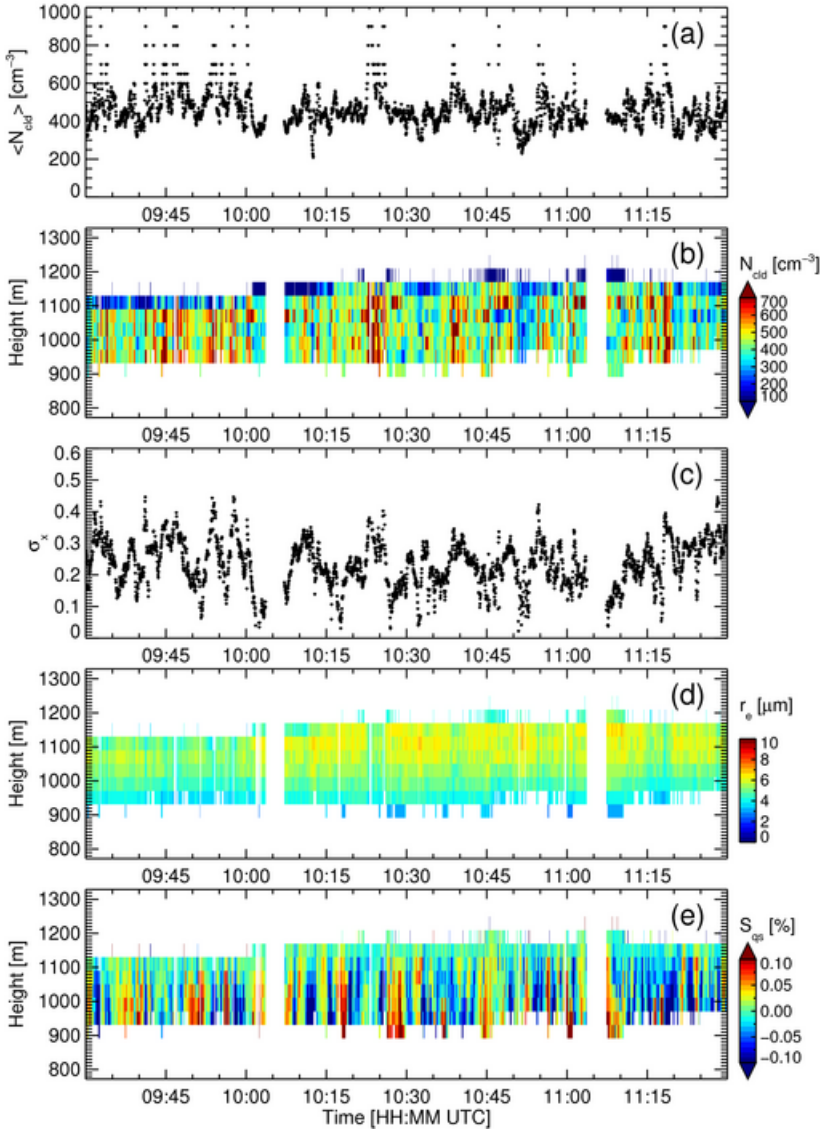

Figure 5–2: Microphysical retrievals obtained over two hours on 13 June 2010: (a) column-averaged cloud droplet number concentration $\langle N_{cld} \rangle$, (b) vertical profile of cloud droplet number concentration $N_{cld}(z)$, (c) logarithmic width σ, (d) cloud effective radius profile $r_e(z)$, and (e) supersaturation profile $S_{qs}(z)$. Periods without retrievals are associated with missing MWR retrievals, or failure of reaching a minimum in Eq. 5.15.

Using Eq. 5.17, the cloud optical depth τ is retrieved and compared with the optical depth τ_{NFOV} retrieved from the NFOV measurements (Fig. 5–3a). The two independently retrieved optical depths agree very well, both in scales of variability and magnitude. Since the LWP variability drives to a

large extent the τ variability, it is not surprising that the radar-radiometer derived and the shortwave derived optical depths agree in the observed scales of variability. Thus, the fact that the two retrievals exhibit very similar values ($\langle\tau\rangle - \langle\tau_{NFOV}\rangle = -0.5$) suggests that the proposed method retrieves the cloud microphysical parameters with reasonable accuracy. In particular, the slope of the relationship between cloud optical depth and LWP depends on the cloud effective radius (e.g., Kim et al., 2003). The linear regression of τ on the LWP values (Fig. 5–3d,e) shows very good fits, with similar slopes. The τ_{NFOV}–LWP derived effective radius retrievals exhibit larger variability compared to the effective radius retrieved using the radar-radiometer method (Fig. 5–3b). This different variability might come from the instruments sensitivities. The radar signal is most sensitive to variations in the presence of big particles, while the effective radius is more affected by the small sizes of the PSD. The assumption that σ is constant with height might also have impacted the variability of our retrievals, since the LWC and τ follow different relations with σ.

If the F95+ radar-radiometer based retrieval technique is applied to derive the cloud layer-average effective radius and optical depth, the range of solutions is very large, depending on the assumed cloud dispersion parameter value (see the gray shaded and hatched regions in Fig. 5–3).

Uncertainties on the retrievals have been evaluated by mathematically propagating an estimated error on each initial measurement: 1 K in the temperature field, 1 hPa in the pressure field, 1 dB for the corrected reflectivity field, and around $6\,\mathrm{g\,m^{-2}}$ for the LWP. The last one comes directly from the LWP retrieval (the physical method here), while the other values were chosen for illustration purpose. The uncertainty obtained from each instrument for the optical depth is shown in Fig. 5–3c. The main factor here is the radar reflectivity errors, due to its additive character in the equations. It results in

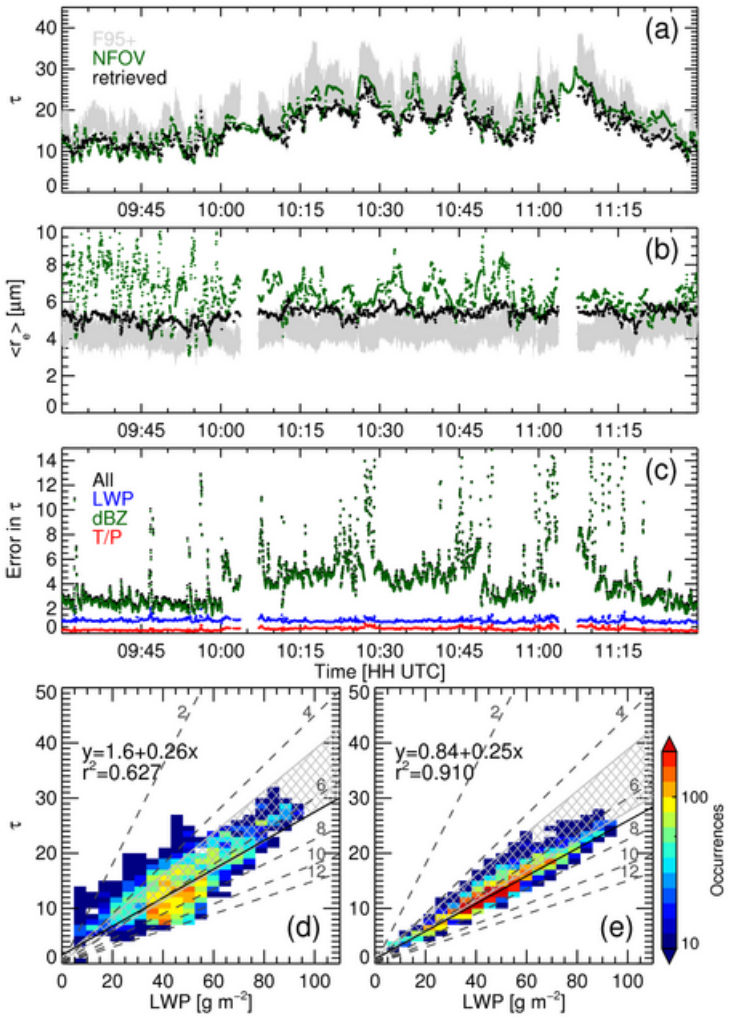

Figure 5–3: Comparison results for two hours on 13 June 2010: (a) cloud optical depth τ, and (b) cloud-layer averaged effective radius $\langle r_e \rangle$, as computed from the retrieved PSD parameters (black), and as retrieved from the NFOV and LWP measurements (green). (c) Errors in the retrieved optical depth, evaluated from the propagation of errors from each instrument and overall. The lower scatter plots show the relationship of τ as a function of the LWP values, as obtained (d) by the NFOV or (e) from the method described here. The black line represents the linear regression performed on the data (excluding those where LWP$<$20 g m^{-2}), with its equation and the goodness of the fit reported in the legend. The dashed lines depict the slopes expected for different values of $\langle r_e \rangle$. The gray shaded or hatched regions illustrate the range of results obtained when using the F95+ method with σ varied between 0.2 and 0.46 (the upper limit is the value reported by Frisch et al. (1998)).

bigger uncertainties for the deeper parts of the cloud, as more radar errors get added in the column.

Overall, the uncertainty shown is close to the range of values obtained by the F95+ technique only by varying the lognormal width, without adding the instruments errors. It shows that the method described has some added skills. In fact, the uncertainty on the retrieved lognormal width and median radius is typically better than 20 % of the retrieved value when using the errors cited above.

5.4.2 Case of 29 June 2010

The second case is a stratocumulus cloud observed on the morning of 29 June 2010 (see Fig. 5–4) following nighttime drizzling conditions over the AMF location. Observed and retrieved parameters are shown for a two-hour daytime period (0930–1130 UTC). A thin cirrus layer (thickness from 0.5 to 1 km) is observed after 1000 UTC at an altitude of 10 km. Very low intensity drizzle (−40 dBZ) is observed sporadically below the cloud base between 1045 and 1115 UTC (Fig. 5–4a). The radar reflectivity profile peaks near the cloud top and exhibit values higher than those observed on the June 13 case. The Doppler measurements (Fig. 5–4b) show several coherent updraft and downdraft structures with vertical air motion magnitudes up to 1.5 $\mathrm{m\,s^{-1}}$. Overall, the cloud has a depth of 250–350 m, with a peak in the LWP during the thickest cloud period (Fig. 5–4c).

The retrieved column-averaged number concentration $\langle N_{cld} \rangle$, the height-dependent N_{cld}, the column constant σ, and the height-dependent effective radius r_e and supersaturation S_{qs} are shown in Fig. 5–5. Lower cloud droplet number concentrations are retrieved (N_{cld} between 200 and 400 $\mathrm{cm^{-3}}$) with the effective radius reaching values up to 10 µm near the cloud top (Fig. 5–5a,b, and d). As in the first case, the retrieved σ values are varying between 0.2 and 0.4 (Fig. 5–5c). The supersaturation S_{qs} field has values within 0.1 %

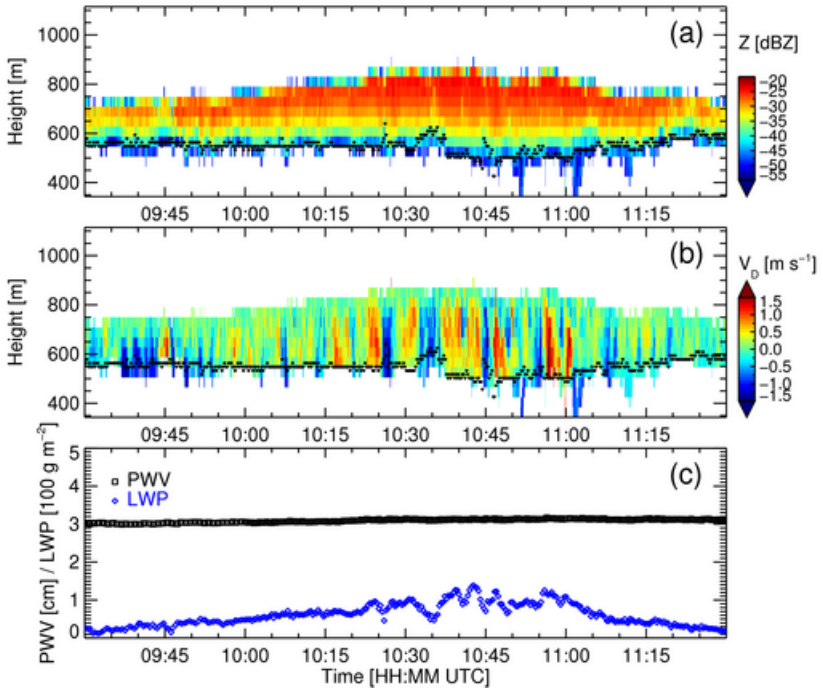

Figure 5–4: Measurements made over a two-hour period on 29 June 2010: (a) radar reflectivity factor, (b) mean Doppler velocity (positive values indicate upward motion), and (c) LWP (blue) and PWV (black) from the MWR. The black dots in (a),(b) represent the cloud-base height as measured by the ceilometer.

(Fig. 5–5e). However, it is clear in this case that more cloud area experiences higher supersaturation compared to the first case.

Once again, using Eq. 5.17, the cloud optical depth τ is retrieved and compared with the optical depth τ_{NFOV} retrieved from the NFOV measurements (Fig. 5–6a). The two independently retrieved optical depths agree very well, both in scales of variability and magnitude, although the bias is higher this time ($\langle\tau\rangle - \langle\tau_{NFOV}\rangle = -3.0$). The presence of the cirrus layer during the observing period provides a plausible explanation for the higher NFOV optical depth values. The linear regression of τ on the LWP values (Fig. 5–6d,e) shows very good fits, with similar slopes. As in the first case, the τ_{NFOV}–LWP derived effective radius retrievals exhibit larger variability compared to the effective radius retrieved using the radar-radiometer method (Fig. 5–6b).

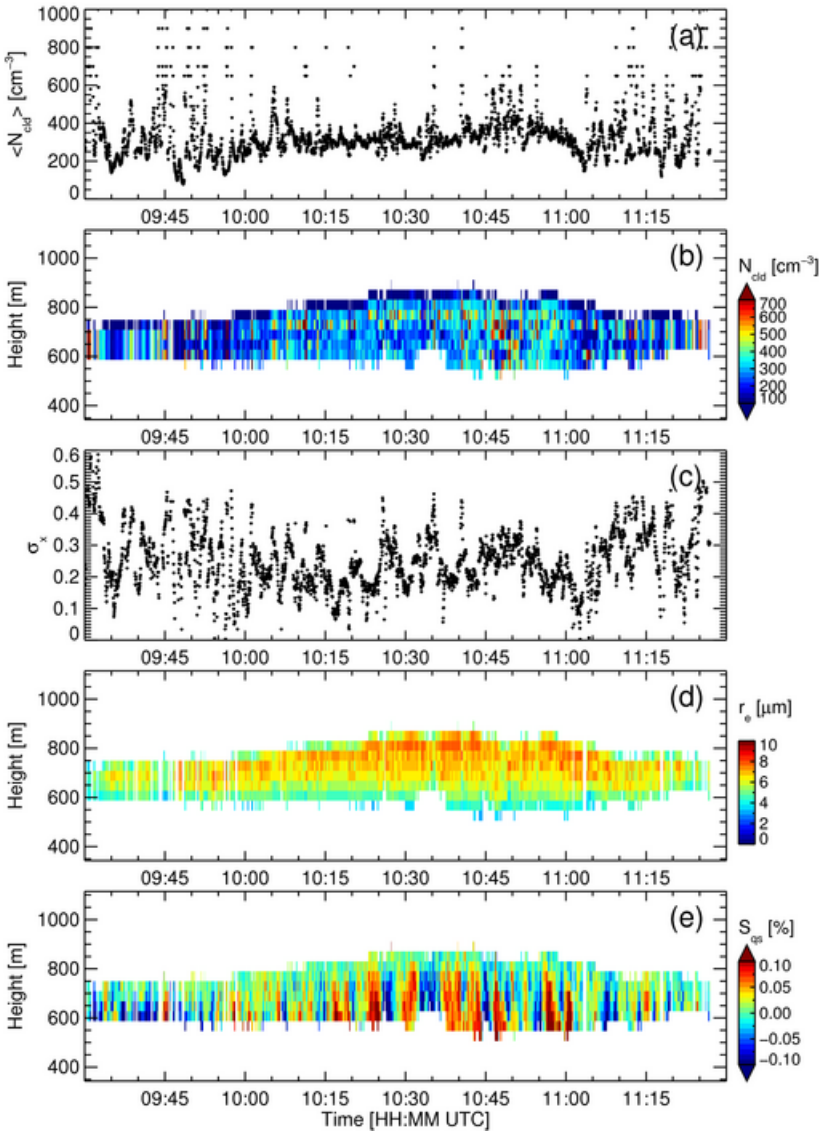

Figure 5–5: Microphysical retrievals obtained over two hours on 29 June 2010: (a) column-averaged cloud droplet number concentration $\langle N_{cld} \rangle$, (b) vertical profile of cloud droplet number concentration $N_{cld}(z)$, (c) logarithmic width σ, (d) cloud effective radius profile $r_e(z)$, and (e) supersaturation profile $S_{qs}(z)$. Periods without retrievals are associated with missing MWR retrievals, or failure of reaching a minimum in Eq. 5.15.

An estimate of the uncertainties of the retrieved optical depths is shown in Fig. 5–6c. For this case, the statistical LWP retrieval was used instead of the physical one (see Turner et al., 2007, for a review of those retrieval

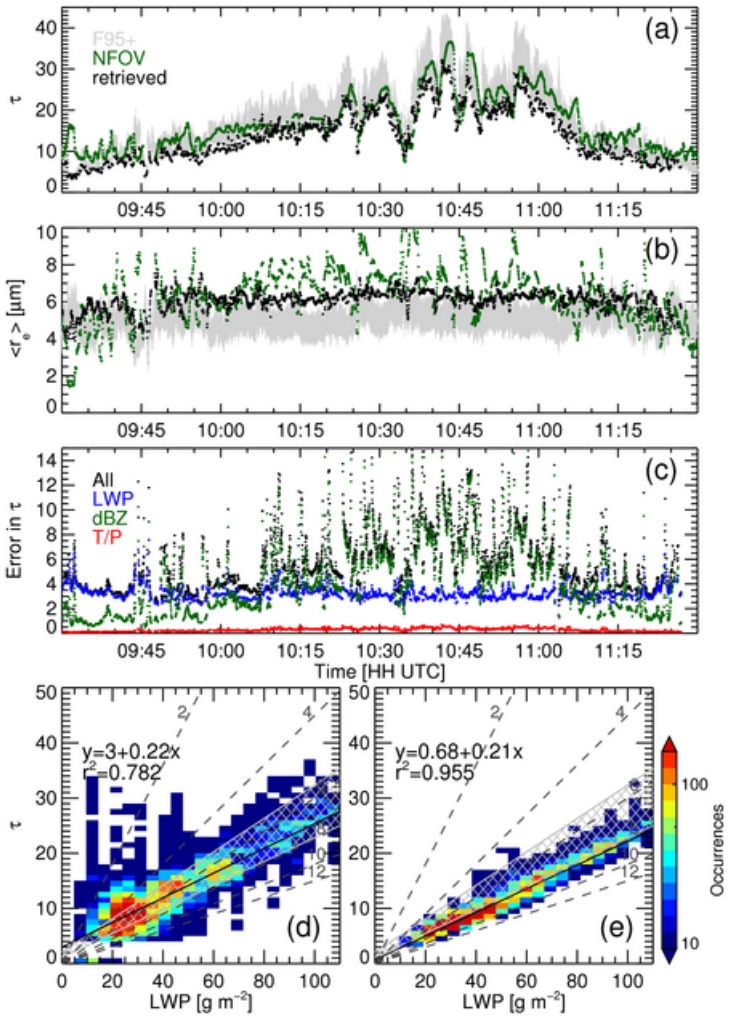

Figure 5–6: Comparison results for two hours on 29 June 2010: (a) cloud optical depth τ, and (b) cloud-layer averaged effective radius $\langle r_e \rangle$, as computed from the retrieved PSD parameters (black), and as retrieved from the NFOV and LWP measurements (green). (c) Errors in the retrieved optical depth, evaluated from the propagation of errors from each instrument and overall. The lower scatter plots show the relationship of τ as a function of the LWP values, as obtained (d) by the NFOV or (e) from the method described here. The black line represents the linear regression performed on the data (excluding those where LWP$<20\,\mathrm{g\,m^{-2}}$), with its equation and the goodness of the fit reported in the legend. The dashed lines depict the slopes expected for different values of $\langle r_e \rangle$. The gray shaded or hatched regions illustrate the range of results obtained when using the F95+ method with σ varied between 0.2 and 0.46 (the upper limit is the value reported by Frisch et al. (1998)).

methods), providing a larger error ($20\,\mathrm{g\,m^{-2}}$). Consequently, it becomes the most important factor for the thin parts of the cloud.

5.5 Summary

Nonprecipitating liquid phase boundary layer clouds are an important component of the Earth's energy budget. Ground-based cloud radars are capable of observing their vertical structure, dynamics and boundaries (Kollias et al., 2007a). However, the use of the radar observables for the retrieval of microphysical parameters is limited to the use of the radar reflectivity as the sixth moments of the cloud PSD. Empirical or theoretical relationships have been proposed to relate the radar reflectivity to the third moment of the PSD, i.e. the LWC. This is the category of radar-only based algorithms. If LWP measurements from a microwave radiometer are available, the radar reflectivity factor can be used as a weighting function to distribute the LWP in the cloud column and thus retrieve the LWC profile with reasonable uncertainty (Frisch et al., 2000). This is the category of the radar-radiometer based algorithms. Using additional constraints (e.g., number concentration and cloud dispersion parameter constant with height, or assuming a climatological value for the dispersion parameter), the cloud effective radius profile can be retrieved, and subsequently all other moments of the cloud PSD. However, these retrievals are subject to large uncertainties and generally do not agree with independent measurements of optical depth and/or solar transmission ratio (Dong et al., 1997; Mace and Sassen, 2000).

Here, a radar-radiometer based algorithm is proposed that is a considerable modification of the F95+ work. The proposed algorithm uses additional information from the radar observables to help to constrain the retrieval of cloud PSD parameters. A cloud condensational model is used to describe the profile of the radar reflectivity. It is demonstrated that the vertical gradient of the radar reflectivity combined with the steady-state supersaturation expression proposed by Korolev and Mazin (2003) can be used to constrain the

relationship between cloud number concentration and dispersion parameter. Consequently, we only assume that σ is constant with height. The cloud number concentration is height-dependent. However, it is required that variations of N_{cld} around its column average remain small. Moreover, the mean Doppler velocity is an estimator of the vertical air motion and it is used to estimate the cloud supersaturation using the relationship proposed by Korolev and Mazin (2003).

Observations from the recent deployment of the AMF at Graciosa are used to demonstrate the application of the technique in two nonprecipitating stratocumulus cloud examples. The new retrieval algorithm outputs profiles of effective radius, cloud number concentration, and supersaturation, and column cloud dispersion parameter. The temporal and spatial structure and magnitude of the retrieved parameters appear reasonable. However, without in situ observations, it is challenging to assess their accuracy. A dedicated aircraft campaign would help to assess the ability of the technique to retrieve the cloud PSD parameters. Such a campaign could also be aimed at determining the validity of the assumptions made for the technique (e.g., a column-constant lognormal width).

Using the retrieved cloud PSD parameters, the cloud optical depth is estimated (Eq. 5.17) and it is compared to the retrieved optical depth from the NFOV radiometer (Chiu et al., 2006). In both cases, the comparison between the two optical depth estimates is very good. In the first case, the difference between the time-averaged optical depths ($\langle\tau\rangle - \langle\tau_{NFOV}\rangle$) is less than -0.5. In the second case, the difference is larger (-3.0) however; the presence of a thin cirrus layer could explain the higher estimates of optical depth from the NFOV radiometer. Compared to the range of solutions for effective radius and τ retrieved using the F95+ technique, the proposed method clearly reduces

the uncertainty in the estimation of the cloud effective radius and column-average dispersion parameter. This illustrates that, under certain conditions, the modeling of cloud and precipitation processes can help in the utilization of additional information hidden in radar observations.

Chapter 6
Conclusions

Marine stratocumulus clouds play a key role in the earth's radiation budget. This is attributed to the large and persistent coverage over the eastern subtropical ocean and their high shortwave albedo. The details of their radiative properties are controlled by both large-scale meteorology and cloud-scale processes. The cloud macrostructure has been widely studied, and much of the variability of the cloudiness in stratocumulus regions can be explained by large-scale processes (e.g., low level tropospheric stability). Nevertheless, cloud-scales also contain appreciable complexity that impacts the cloud's life and environment, but the details that trigger their onset (e.g., drizzle production) and their relationship to the large-scale meteorology remain not well understood. For instance, aerosol loading effects and drizzle production are two challenging areas to accurately represent in models.

A typical ground-based instrumentation suite for cloud studies includes the following three remote sensors: a millimeter radar, a lidar, and a microwave radiometer (MWR). Ground-based millimeter radars are capable of observing the vertical structure, dynamics, and boundaries of cloud and precipitation, with a better sensitivity at low levels (Kollias et al., 2007a). The recording of the full radar Doppler spectrum is now a common approach in profiling millimeter radars, since it offers new opportunities for the study of cloud and precipitation microphysics and dynamics. A profiling lidar is useful to detect the actual cloud base, i.e. the lowest location of numerous small droplets, especially when precipitation is falling from the cloud. Finally, a MWR provides

the amount of liquid water present in the atmosphere, denoting the presence of liquid clouds.

The CAP-MBL campaign led to the collection of an extensive and well-documented ground-based data set of marine boundary layer (MBL) clouds. To highlight their occurrences, a radar-lidar algorithm was developed and applied to the 19 months of synergetic measurements. It illustrates the predominance of the MBL clouds over higher topped clouds in the Azores all year long. When breaking down the MBL clouds into subtypes, it was found that stratocumulus clouds occur preferably during transition seasons, while cumulus clouds were observed during all seasons.

6.1 Summary

In chapter 3, similarities were highlighted between the persisting stratocumulus clouds observed in the Azores and those found in South-East Pacific. In both regions, their diurnal cycle is marked by a decreased coverage in the afternoon, associated with a thinning of the cloud layer and a decrease in ground precipitation, which is maximized around sunrise and sunset. Also consistent with the Pacific decks is the likelihood for clouds deeper than 250 m with a liquid water path (LWP) above $60\,\mathrm{g\,m^{-2}}$ to precipitate.

Additional similarities between the two regions include the importance of nighttime cloud-top radiative cooling and daytime surface heating to the stratocumulus life cycle. Also as in the Pacific decks, greater turbulence is observed at night, and it is maximized in the bottom half of the cloud throughout the day. Finally, the updraft regions represent about 50 % of the stratocumulus throughout its depth, consistent with we expect.

Despite the aforementioned similarities, stratocumulus clouds in the Azores have some unique behavior. For instance, their coherent structures account for only 40 %–60 % of the total updraft mass flux, as opposed to the 75 % observed

elsewhere. Furthermore, the marine boundary layer in the Azores appears to be decoupled most of the time, even in the presence of stratocumulus. This explains the more frequent detection of shallow cumulus clouds underneath stratocumulus layers in the Azores than under the Pacific decks. It could also be linked to the short-lived character often observed for stratocumulus clouds in the Azores.

These results demonstrated that the stratocumulus clouds observed in the Azores are quite similar to those occurring elsewhere in the world. Consequently, more detailed studies done using the data collected during CAP-MBL could be generalized to all stratocumulus regions. First, it was necessary to assess the impact of drizzle particles in the observed clouds.

In chapter 4, the radar Doppler spectra moments (reflectivity factor, mean Doppler velocity, spectrum width, skewness, and kurtosis) were related to the cloud and drizzle particle size distributions (PSD) in various ways. First, analytical relations were developed assuming the PSDs have truncated lognormal shapes. The dynamics effects are also considered in these relations. Then, a forward model was built to explore the potential of the radar measurements to study cloud and precipitation microphysics and dynamics in simple liquid cloud systems. Finally, a simplified 1D drizzle growth model was exploited to better understand the radar observations in stratocumulus clouds.

A new approach was introduced to study liquid clouds that form drizzle using radar Doppler spectra. From observations and modeling, it was demonstrated that the skewness of the radar Doppler spectrum is a good indicator of the creation of drizzle droplets. It is more sensitive to the early presence of drizzle particles than parameters in use nowadays. This sensitivity is possible due to the low noise level of current millimeter radars that allow the detection of weak spectral bumps on either side of the main peak. Such a non-Gaussian

feature appears when drizzle forms as bigger liquid droplets have a greater fall velocity. Using the 1D model, it was shown that the autoconversion process responsible for the drizzle onset in warm clouds can cause a change in skewness as observed.

It can also be taken from chapter 4 that simplified models can help understand observations, and direct further studies toward more specific goals. For instance, differences in behavior of the continental and maritime clouds were successfully explored using the simplified 1D drizzle growth model, such as the importance of autoconversion in marine clouds even when drizzle is well developed. Feeding microphysical model output into a forward model to emulate radar observables provides a methodology for interpreting radar observations and for improving microphysical modeling. This closed loop process offers new venues for exploring cloud microphysics and dynamics at very small scale.

Finally, observations show that drizzle is ubiquitous in marine clouds. Its effects are visible even at reflectivity factors as low as $-40\,\mathrm{dBZ}$, which is not the case in continental clouds. Nevertheless, the visibility of the effects depend on the measurement considered. For instance, the reflectivity factor and mean Doppler velocity of a radar Doppler spectrum are clearly less affected by the early stages of drizzle production than the higher moments (e.g., the spectral width and skewness). Therefore, when the drizzle production is limited (i.e. when the drizzle particles' sizes remain small), the effects on these two radar measurements might be negligible, allowing for the testing of microphysical retrieval methods about the cloud particles directly.

Chapter 5 tackled the issue of the missing cloud PSD. Of the radar observables, only the reflectivity factor is relevant, representing the sixth moment of the PSD. The dynamics of the atmosphere dominates the Doppler spectrum velocity moments, rendering them useless for cloud PSD retrievals.

LWP measurements constrain the retrieval of the liquid water content (LWC; third moment of the PSD) profiles using the reflectivity factor as a weighting function (Frisch et al., 1998). This requires the absence of drizzle particles, as they dominate the reflectivity measurements when drizzle is well developed. On the other hand, the knowledge of the cloud contribution to the reflectivity would be sufficient to relate it to the cloud LWC.

The retrieval of actual cloud PSD parameters requires further constraints to be able to estimate the parameters of an analytical function. Here, we used a cloud condensational model to describe the reflectivity profile and get additional information hidden in the radar observations. Consequently, unlike Frisch et al. (2002), we allowed the number concentration to vary in the column, although only slightly, assuming only an height-independent dispersion parameter. It results that, when combined with a steady-state supersaturation expression proposed by Korolev and Mazin (2003), the vertical gradient of the radar reflectivity can be used to constrain the relationship between the cloud number concentration and the dispersion parameter. Finally, in the absence of significant drizzle particles, the observed mean Doppler velocity was used to estimate the vertical air motion, allowing the retrieval of the cloud supersaturation too.

Another major difference from Frisch et al. (2002) technique is that the dispersion parameter is actually retrieved as part of the algorithm, rather than estimate from a general or local climatology. As such, uncertainties on the retrieved quantities are rather small, especially for the dispersion parameter and characteristic sizes (typically $< 20\,\%$).

Assuming a lognormal distribution, the new algorithm retrieves three cloud PSD parameters at the time resolution of the millimeter radar. These are the profiles of characteristic radius and number concentration, and the

column-constant dispersion parameter. Two cases were chosen to evaluate the retrieval technique. These are stratocumulus coverages lasting a few hours over the Azores site, with a very limited drizzle production. Therefore, the drizzle particles contribution to the measurements is neglected in both cases.

From the retrieved parameters, the cloud optical depth is estimated and compared to the one retrieved independently by another instrument, the 2-channel Narrow Field of View Zenith Radiometer (NFOV; Chiu et al., 2006). The scales of variability of the retrieved cloud optical depth compare well in both cases. For its magnitude, the agreement is also very good, especially in the first case. The bigger discrepancies in the second case can be attributed to the presence of a cirrus layer above, as detected by the radar.

To suppress drizzle for such a long time, continental-like cloud PSDs were expected, and obtained: number concentration in the hundreds, and effective radius generally smaller than 10 µm. PSDs narrower than the climatological in situ average are also consistent with the lack of significant drizzle production. Both studied cases have supersaturation below 0.1 %, but the case with higher reflectivity factors has more area experiencing higher supersaturation. Its retrieved number concentrations are also lower and bigger radii are reached.

6.2 Future Work

Possible ways to further advance the work done in this project can be divided in various area. The development of a fixed ARM site in the Azores (ENA site) should provide continuous observations from the fall of 2013 and beyond. At the minimum, the longer observation record is expected to enable us to derive more robust climatology using the methods outlined in chapter 3.

Operations at the ENA site will also bring new cases of stratocumulus coverage, which will be useful to increase the confidence level of the results

presented here. For instance, it will be interesting to see if the seasonal preferences were only an anomaly that happened during the studied period. It would also be interesting to fortify the seasonal differences observed during the studied 19 months.

Another approach to the stratocumulus in the Azores is through the large-scale meteorology. This aspect was not touched directly in this work, although it was often mentioned briefly. Being located south of the midlatitude storm's track of the Atlantic ocean and near the Azores high pressure system, Graciosa Island can experience midlatitude systems as well as trade-wind conditions and everything in between. Consequently, it would be interesting to explore the synoptic conditions during stratocumulus cases, and see what situation(s) stands out. Depending on the results, this could help improve stratocumulus parameterization in models, dictating conditions that support the formation or breaking of stratocumulus, as well as their influence on its drizzle production.

Another area of future work is related to the cloud PSD retrieval technique developed here, and the need to perform additional testing and validation in diverse conditions (e.g., extend the analysis to continental clouds from the Southern Great Plains site). Once a reliable separation of the radar measurements into their cloud and drizzle contributions will be available, the technique could be applied to virtually all stratocumulus cases. This will allow a more robust characterization of the skills of the technique. It would also be interesting to see how it applies to actual continental cases. In addition, an aircraft campaign could be of great value to provide an actual comparison with in situ measurements, and thus supplying a stronger evaluation of the technique.

A final area of future research is related to the modeling of cloud-scale processes, especially in the models resolving those processes. Cloud-scale models

can be used to understand better the interaction between the various controlling factors. The observations presented here (e.g., profiles of Doppler spectra skewness and kurtosis) offer unique insights on drizzle production within the cloud layer and offer new ways of constraining numerical models.

Such studies would in turn help the effort to improve the parameterization of clouds in models at larger scale, by narrowing down the important factors and their main impacts. In global models, any improvement of the stratocumulus parameterization would be welcomed, as it might narrow down the uncertainties associated with these clouds. Finally, numerical weather prediction models could benefit from the inclusion of a drizzle category in their microphysics scheme, as it is the main precipitation produced by stratocumulus. It could influence the lifetime of clouds, as well as the amount of water reaching the surface and the timing of a precipitation event.

Appendix A: Addendum to Chapter 3

Collected here are supplemental comments on chapter 3 gathered during the revision of the thesis. They are presented in this addendum to preserve the published version of the paper making up chapter 3.

First, the campaign that provided the data set used in chapter 3 officially started in May 2009. However, not all instruments began operating at the same date. For instance, the ceilometer started collecting data in April 2009, while the radar was only functional in early June 2009. Nevertheless, most of the instruments were turned down around the same time, when the site was packed up in early January 2011. Therefore, the campaign officially spanned 20 months, but some would say that it actually lasted nearer to 21 months. On the other hand, the synergetic collection of data useful for chapter 3 covers only 19 months. This is why chapter 3 seems inconsistent on this part, but the duration mentioned depends on the context of the statement.

Second, although the Azores islands are small and isolated in the middle of the Atlantic ocean, the atmosphere encountered might not be fully marine, especially in the lower troposphere directly surrounding the islands. Choosing the north shore of Graciosa Island reduces the effects, as only the ocean is present further north, covering everything from the West to the East. With the mean wind coming from there, it is assumed that the island effects are greatly reduced. However, it is unlikely that the chosen location for the site is completely free of island effects. For instance, the development of a land-sea breeze cannot be prevented and is likely occurring even on such a small island as Graciosa (about $60\,\mathrm{km}^2$). The differential heating and cooling rates between the land and the sea would cause a local circulation of the winds, especially near the shore, that gets reversed during day and night. This occurs near the

surface, complicating the analysis of the winds (see Fig. 3–7 for an example of what it might look like). This breeze might also help to the formation or decay of low-level clouds. A more thorough analysis of the wind profiles and surface heating rates is needed to properly characterize these island effects.

Also note that, although the four instruments used in this analysis operated close to one another, they were not interacting in any way. For instance, their measurements were not synchronized. That is why it was necessary to match the time variable of each instrument for the analysis. It was desirable to preserve the native radar time resolution to retain its detail, as the radar provides most of the measurements. Since the ceilometer and the radiometer measurements used in this study are non-profile quantities that typically vary smoothly (on a scale smaller than their resolution), it is possible to argue that those measurements are also relevant within the time steps.

The following is a list of some supplementary notes about the analysis methods described in section 3.3:

- Only the radar and the ceilometer are used in the cloud and precipitation algorithm as they are known to be sufficient to obtain profiles under most conditions, especially those that interest us in the Azores (i.e. light drizzle at most).
- Although boundary layer clouds can produce drizzle echoes above 0 dBZ, this is rarely happening. And it is important to realize that this 0-dBZ criterion for intense precipitation capture most of the events, but not all. The remaining ones can still affect the results, as in Fig. 3–8. However, they are only removed for the analysis of the boundary layer clouds done in section 3.4.2 and subsequent.
- The unit used for reflectivity (dBZ) is a logarithmic scale similar to the decibel. It uses a reference of $1\,\mathrm{mm}^6\,\mathrm{m}^{-3}$, and thus negative dBZ values

simply represent reflectivity factors (which are related to the returned power) below this reference value.

- Throughout this work, droplets are considered to be good air tracers in the Doppler radar measurements. This is valid as long as the terminal velocity of the droplets remains smaller that the velocity resolution of the radar. For the WACR, this limit radius is around 23 µm, which is near the limit considered in our droplets size distributions (25 µm).
- Although smoothing the sounding data is not great to find sharp inversions, it is needed to remove the spurious variations that remained after the sounding software manipulations. It allows the detection of a main temperature inversion, rather than a noisy one, although its depth might now be slightly overestimated. Obviously, it is possible that multiple inversions were present (e.g., at the cloud base and top), but only the strongest one is noted to simplify the analysis.
- The transition layer is noticeable mostly in the humidity profile, and thus requires a different method to detect it. To simplify the analysis, only the strongest transition is noted, although multiple ones can be present.
- Up to five layers were considered in the sounding analysis, but fewer layers were possible. These cases were rare and not considered for the analysis associated with Fig. 3–7.
- Note that the variable M_c is often referred to as the updraft mass flux in the analysis, although it was defined as (and it is) the convective mass flux, which is not exactly the same thing.

It is understood that uncertainty estimates and significance assessments are needed to properly interpret the cloud statistics presented in the results. However, as the data covers a limited span of time with much embedded seasonal variability, the sample variance of the results is often rather high

for each situation. This creates overlap between the compared situations. Also, the actual values reported (except for occurrence fractions) might not be representative of any given situation. Instead, the emphasis should be put on the separation between the values reported for different conditions. A longer data set is needed to be able to reasonably populate more specific categories (e.g., specific seasonal synoptic conditions) before robust conclusions can be drawn here.

And finally, here are more random notes in support of the analysis done in section 3.4:

- Although the identification of cloud types is carried on an hourly basis, the analysis is done using the radar native 2-s resolution.
- The seasonal cycle of the cloud types is less present for low clouds (Fig. 3–3b), as they can also occur in association with midlatitude systems.
- Note that, in the single and multilayer conditions described in section 3.4.2, multiple clouds can be observed at the same level to form a layer (e.g., scattered cumulus).
- The horizontal extent mentioned in section 3.4.2 refers to the duration criterion in Table 3–2.
- The stability criterion introduced near the end of section 3.4.3.1 is a measure of the cloud-top stability under the entrainment of free-tropospheric air. Mathematically, it states that the cloud top is stable if $\Delta\theta_e > k\frac{L}{c_p}\Delta r$, with k being a dimensionless parameter whose value depends on the processes considered (typically between 0.23 and 0.7).
- Although never discuss in the paper, the island might have played a role in the diurnal evolution of the observed low-level clouds. For instance, as described earlier in this addendum, a land-sea breeze is likely occurring near the shore.

Appendix B: List of Expressions for Chapter 5

List of expressions used throughout the work, but left undefined, and some symbols (adapted from Korolev and Mazin (2003)).

Symbol	Description	Units
S_{qs}	$\dfrac{a_0 w_{air}\left[F_k + F_D\right]}{b_0 N_{cld} r_0 \exp\left(\sigma^2/2\right)}$	—
a_0	$\dfrac{g}{R_m T}\left(\dfrac{L_v R_m}{c_{pm} R_v T} - 1\right)$	m^{-1}
b_0	$\dfrac{4\pi\rho_w}{\rho_a}\left(\dfrac{1}{q_v} + \dfrac{L_v^2}{c_{pm} R_v T^2}\right)$	—
F_k	$\left(\dfrac{L_v}{R_v T} - 1\right)\dfrac{\rho_w L_v}{KT}$	$\mathrm{m}^2\,\mathrm{s}^{-1}$
F_D	$\dfrac{\rho_w R_v T}{e_s(T) D}$	$\mathrm{m}^2\,\mathrm{s}^{-1}$

c_{pm}	Specific heat capacity of moist air at constant pressure	$\mathrm{J\,kg^{-1}\,K^{-1}}$
D	Coefficient of water vapor diffusion in the air	$\mathrm{m^2\,s^{-1}}$
$e_s(T)$	Saturation vapor pressure over liquid water	Pa
g	Acceleration of gravity	$\mathrm{m\,s^{-2}}$
K	Coefficient of air heat conductivity	$\mathrm{J\,m^{-1}\,s^{-1}\,K^{-1}}$
L_v	Latent heat for liquid water evaporation	$\mathrm{J\,kg^{-1}}$
q_v	Water vapor mixing ratio	—
R_m	Specific gas constant of moist air	$\mathrm{J\,kg^{-1}\,K^{-1}}$
R_v	Specific gas constant of water vapor	$\mathrm{J\,kg^{-1}\,K^{-1}}$
T	Air temperature	K
w_{air}	Vertical air motion	$\mathrm{m\,s^{-1}}$
ρ_a	Density of dry air	$\mathrm{kg\,m^{-3}}$
ρ_w	Density of liquid water	$\mathrm{kg\,m^{-3}}$

Appendix C: List of Acronyms

AAF	ARM Aerial Facility
ACC	accretion process
ACRF	ARM Climate Research Facililty
AGL	above ground level
AMF	ARM Mobile Facility
ARM	Atmospheric Radiation Measurement
ASTEX	Atlantic Stratocumulus Transition Experiment
BBSS	Balloon-Borne Sounding System
BL	boundary layer
CAP-MBL	Clouds, Aerosol, and Precipitation in the Marine Boundary Layer
CCN	cloud condensation nuclei
CT	cloud top
Cu	cumulus
DSS	Doppler Spectra Simulator
ENA	Eastern North Atlantic
GRW	Graciosa Island
Ind/indeterm	inderterminate
LES	Large-Eddy Simulation
LTS	lower tropospheric stability
LWC	liquid water content
LWP	liquid water path
MBL	marine boundary layer
ML	multilayer conditions

MODIS	Moderate Resolution Imaging Spectroradiometer
MSL	mean sea level
MWR	Microwave Radiometer
NFOV	2-channel Narrow Field of View Zenith Radiometer
NSA	North Slope of Alaska
PDF	probability density function
PRC	process considered
PSD	particle size distribution
PWV	precipitable water vapor
Precip	precipitation
SGP	Southern Great Plains
SLa	single layer conditions at the inversion level
SLb	single layer conditions at the transition level
SNR	signal-to-noise ratio
Sc	stratocumulus
TWP	Tropical Western Pacific
UTC	Universal Time Coordinates
WACR	W-band ARM Cloud Radar
WMO	World Meteorological Organization

References

Abel, S. J., D. N. Walters, and G. Allen, 2010: Evaluation of stratocumulus cloud prediction in the Met Office forecast model during VOCALS-REx. *Atmos. Chem. Phys.*, **10**, 10 541–10 559, doi:10.5194/acp-10-10541-2010.

Ackerman, A. S., M. P. Kirkpatrick, D. E. Stevens, and O. B. Toon, 2004: The impact of humidity above stratiform clouds on indirect aerosol climate forcing. *Nature*, **432**, 1014–1017, doi:10.1038/nature03174.

Ackerman, T. P. and G. M. Stokes, 2003: The Atmospheric Radiation Measurement program. *Phys. Today*, **56**, 38–44, doi:10.1063/1.1554135.

Albrecht, B. A., 1989: Aerosols, cloud microphysics, and fractional cloudiness. *Science*, **245 (4923)**, 1227–1230, doi:10.1126/science.245.4923.1227.

Albrecht, B. A., 1993: Effects of precipitation on the thermodynamic structure of the trade wind boundary layer. *J. Geophys. Res.*, **98 (D4)**, 7327–7337.

Albrecht, B. A., C. S. Bretherton, D. Johnson, W. H. Schubert, and A. S. Frisch, 1995: The Atlantic Stratocumulus Transition Experiment—ASTEX. *Bull. Amer. Meteor. Soc.*, **76 (6)**, 889–904.

Albrecht, B. A., D. A. Randall, and S. Nicholls, 1988: Observations of marine stratocumulus clouds during FIRE. *Bull. Amer. Meteor. Soc.*, **69 (6)**, 618–626.

Atlas, D., 1954: The estimation of cloud parameters by radar. *J. Meteor.*, **11**, 309–317.

Augstein, E., H. Schmidt, and F. Ostapoff, 1974: The vertical structure of the atmospheric planetary boundary layer in undisturbed trade winds over the Atlantic ocean. *Bound.-Layer Meteor.*, **6**, 129–150.

Beheng, K. D., 1994: A parameterization of warm cloud microphysical conversion processes. *Atmos. Res.*, **33**, 193–206.

Bony, S. and J.-L. Dufresne, 2005: Marine boundary layer clouds at the heart of tropical cloud feedback uncertainties in climate models. *Geophys. Res. Lett.*, **32**, L20 806, doi:10.1029/2005GL023851.

Bretherton, C. S., et al., 2004: The EPIC 2001 stratocumulus study. *Bull. Amer. Meteor. Soc.*, **85 (7)**, 967–977, doi:10.1175/BAMS-85-7-967.

Caldwell, P., C. S. Bretherton, and R. Wood, 2005: Mixed-layer budget analysis of the diurnal cycle of entrainment in southeast Pacific stratocumulus. *J. Atmos. Sci.*, **62**, 3775–3791.

Carman, J. K., D. K. Rossiter, H. H. Jonsson, I. C. Faloona, and P. Y. Chuang, 2012: Observational constraints on entrainment and the entrainment interface layer in stratocumulus. *Atmos. Chem. Phys. Discuss.*, **12**, 817–868, doi:10.5194/acpd-12-817-2012.

Chin, H.-N. S., D. J. Rodriguez, R. T. Cederwall, C. C. Chuang, A. S. Grossman, J. J. Yio, Q. Fu, and M. A. Miller, 2000: A microphysical retrieval scheme for continental low-level stratiform clouds: impacts of the subadiabatic character on microphysical properties and radiation budgets. *Mon. Wea. Rev.*, **128**, 2511–2527.

Chiu, J. C., A. Marshak, Y. Knyazikhin, W. J. Wiscombe, H. W. Barker, J. C. Barnard, and Y. Luo, 2006: Remote sensing of cloud properties using ground-based measurements of zenith radiance. *J. Geophys. Res.*, **111**, D16 201, doi:10.1029/2005JD006843.

Clark, T. L., 1976: Use of log-normal distributions for numerical calculations of condensation and collection. *J. Atmos. Sci.*, **33**, 810–821.

Clothiaux, E. E., M. A. Miller, B. A. Albrecht, T. P. Ackerman, J. Verlinde, D. M. Babb, R. M. Peters, and W. J. Syrett, 1995: An evaluation of a 94-GHz radar for remote sensing of cloud properties. *J. Atmos. Oceanic Technol.*, **12 (2)**, 201–229.

Cohard, J.-M. and J.-P. Pinty, 2000: A comprehensive two-moment warm microphysical bulk scheme. I: Description and tests. *Quart. J. Roy. Meteor. Soc.*, **126**, 1815–1842.

Comstock, K. K., R. Wood, S. E. Yuter, and C. S. Bretherton, 2004: Reflectivity and rain rate in and below drizzling stratocumulus. *Quart. J. Roy. Meteor. Soc.*, **130**, 2891–2918, doi:10.1256/qj.03.187.

de Laat, A. T. J. and P. G. Duynkerke, 1998: Analysis of ASTEX-stratocumulus observational data using a mass-flux approach. *Bound.-Layer Meteor.*, **86**, 63–87.

de Roode, S. R. and P. G. Duynkerke, 1997: Observed Lagrangian transition of stratocumulus into cumulus during ASTEX: mean state and turbulence structure. *J. Atmos. Sci.*, **54 (17)**, 2157–2173.

de Szoeke, S. P., C. W. Fairall, and S. Pezoa, 2009: Ship observations of the tropical Pacific ocean along the coast of South America. *J. Climate*, **22**, 458–464, doi:10.1175/2008JCLI2555.1.

de Szoeke, S. P. and S.-P. Xie, 2008: The tropical eastern Pacific seasonal cycle: Assessment of errors and mechanisms in IPCC AR4 coupled ocean-atmosphere general circulation models. *J. Climate*, **21**, 2573–252 590, doi:10.1175/2007JCLI1975.1.

Dong, X., T. P. Ackerman, E. E. Clothiaux, P. Pilewskie, and Y. Han, 1997: Microphysical and radiative properties of boundary layer stratiform clouds deduced from ground-based measurements. *J. Geophys. Res.*, **102 (D20)**, 23 829–23 843.

Faloona, I., et al., 2005: Observations of entrainment in eastern Pacific marine stratocumulus using three conserved scalars. *J. Atmos. Sci.*, **62**, 3268–3285.

Fox, N. I. and A. J. Illingworth, 1997: The retrieval of stratocumulus cloud properties by ground-based cloud radar. *J. Appl. Meteor.*, **36**, 485–492.

Frisch, A. S., C. W. Fairall, and J. B. Snider, 1995: Measurement of stratus cloud and drizzle parameters in ASTEX with a Ka-band Doppler radar and a microwave radiometer. *J. Atmos. Sci.*, **52 (16)**, 2788–2799.

Frisch, A. S., G. Feingold, C. W. Fairall, T. Uttal, and J. B. Snider, 1998: On cloud radar and microwave radiometer measurements of stratus cloud liquid water profiles. *J. Geophys. Res.*, **103 (D18)**, 23 195–23 197.

Frisch, A. S., B. E. Martner, I. Djalalova, and M. R. Poellot, 2000: Comparison of radar/radiometer retrievals of stratus cloud liquid-water content profiles with in situ measurements by aircraft. *J. Geophys. Res.*, **105 (D12)**, 15 361–15 364.

Frisch, S., M. Shupe, I. Djalalova, G. Feingold, and M. Poellot, 2002: The retrieval of stratus cloud droplet effective radius with cloud radars. *J. Atmos. Oceanic Technol.*, **19**, 835–842.

Garstang, M. and A. K. Betts, 1974: A review of the tropical boundary layer and cumulus convection: structure, parameterization, and modeling. *Bull. Amer. Meteor. Soc.*, **55 (10)**, 1195–1205.

Geoffroy, O., J.-L. Brenguier, and F. Burnet, 2010: Parametric representation of the cloud droplet spectra for LES warm bulk microphysical schemes. *Atmos. Chem. Phys.*, **10**, 4835–4848, doi:10.5194/acp-10-4835-2010.

Gerber, H., 1996: Microphysics of marine stratocumulus clouds with two drizzle modes. *J. Atmos. Sci.*, **53 (12)**, 1649–1662.

Ghate, V. P., B. A. Albrecht, C. W. Fairall, and R. A. Weller, 2009: Climatology of surface meteorology, surface fluxes, cloud fraction, and radiative forcing over the southeast Pacific from buoy observations. *J. Climate*, **22**, 5527–5540, doi:10.1175/2009JCLI2961.1.

Ghate, V. P., B. A. Albrecht, and P. Kollias, 2010: Vertical velocity structure of nonprecipitating continental boundary layer stratocumulus clouds. *J. Geophys. Res.*, **115**, D13 204, doi:10.1029/2009JD013091.

Ghate, V. P., M. A. Miller, and L. DiPretore, 2011: Vertical velocity structure of marine boundary layer trade wind cumulus clouds. *J. Geophys. Res.*, **116**, D162 606, doi:10.1029/2010JD015344.

Gossard, E. E., R. G. Strauch, and R. R. Rogers, 1990: Evolution of drop-size distributions in liquid precipitation observed by ground-based Doppler radar. *J. Atmos. Oceanic Technol.*, **7**, 815–828.

Guo, H., Y. Liu, P. H. Daum, G. I. Senum, and W.-K. Tao, 2008: Characteristics of vertical velocity in marine stratocumulus: comparison of large eddy simulations with observations. *Environ. Res. Lett.*, **3**, 045 020, doi: 10.1088/1748-9326/3/4/045020.

Hasanean, H. M., 2004: Variability of the north Atlantic subtropical high and associations with tropical sea-surface temperature. *Int. J. Climatol.*, **24**, 945–957, doi:10.1002/joc.1042.

Hignett, P., 1991: Observations of diurnal variation in a cloud-capped marine boundary layer. *J. Atmos. Sci.*, **48 (12)**, 1474–1482.

Illingworth, A. J., et al., 2007: Cloudnet: continuous evaluation of cloud profiles in seven operational models using ground-based observations. *Bull. Amer. Meteor. Soc.*, **88 (6)**, 1–16, doi:10.1175/BAMS-88-6-xxx.

Intrieri, J. M., M. D. Shupe, T. Uttal, and B. J. McCarty, 2002: An annual cycle of Arctic cloud characteristics observed by radar and lidar at SHEBA.

J. Geophys. Res., **107 (C10)**, doi:10.1029/2000JC000423.

Kato, S., G. G. Mace, E. E. Clothiaux, J. C. Liljegren, and R. T. Austin, 2001: Doppler cloud radar derived drop size distributions in liquid water stratus clouds. *J. Atmos. Sci.*, **58**, 2895–2911.

Kim, B.-G., M. A. Miller, S. E. Schwartz, Y. Liu, and Q. Min, 2008: The role of adiabaticity in the aerosol first indirect effect. *J. Geophys. Res.*, **113**, D05 210, doi:10.1029/2007JD008961.

Kim, B.-G., S. E. Schwartz, M. A. Miller, and Q. Min, 2003: Effective radius of cloud droplets by ground-based remote sensing: Relationship to aerosol. *J. Geophys. Res.*, **108 (D23)**, 4740, doi:10.1029/2003JD003721.

Klein, S. A. and D. L. Hartmann, 1993: The seasonal cycle of low stratiform clouds. *J. Climate*, **6**, 1587–1606.

Kogan, Y. L., Z. N. Kogan, and D. B. Mechem, 2007: Assessing the errors of cloud liquid water and precipitation flux retrievals in marine stratocumulus based on Doppler radar parameters. *J. Hydrometeor.*, **8**, 665–677, doi:10.1175/JHM603.1.

Kollias, P. and B. Albrecht, 2000: The turbulence structure in a continental stratocumulus cloud from millimeter-wavelength radar observations. *J. Atmos. Sci.*, **57**, 2417–2434.

Kollias, P. and B. Albrecht, 2010: Vertical velocity statistics in fair weather cumuli at the ARM TWP Nauru climate research facility. *J. Climate*, **23**, 6590–6604, doi:10.1175/2010JCLI3449.1.

Kollias, P., B. A. Albrecht, R. Lhermitte, and A. Savtchenko, 2001: Radar observations of updrafts, downdrafts, and turbulence in fair-weather cumuli. *J. Atmos. Sci.*, **58**, 1750–1766.

Kollias, P., E. E. Clothiaux, M. A. Miller, B. A. Albrecht, G. L. Stephens, and T. P. Ackerman, 2007a: Millimeter-wavelength radars: New frontier in atmospheric cloud and precipitation research. *Bull. Amer. Meteor. Soc.*, **88 (10)**, 1608–1624, doi:10.1175/BAMS-88-10-1608.

Kollias, P., E. E. Clothiaux, M. A. Miller, E. P. Luke, K. L. Johnson, K. P. Moran, K. B. Widener, and B. A. Albrecht, 2007b: The Atmospheric Radiation Measurement program cloud profiling radars: second-generation sampling strategies, processing, and cloud data products. *J. Atmos. Oceanic Technol.*, **24**, 1199–1214, doi:10.1175/JTECH2033.1.

Kollias, P., C. W. Fairall, P. Zuidema, J. Tomlinson, and G. A. Wick, 2004: Observations of marine stratocumulus in SE Pacific during the PACS 2003 cruise. *Geophys. Res. Lett.*, **31**, L22 110, doi:10.1029/2004GL020751.

Kollias, P., J. Rémillard, E. Luke, and W. Szyrmer, 2011a: Cloud radar Doppler spectra in drizzling stratiform clouds: 1. Forward modeling and remote sensing applications. *J. Geophys. Res.*, **116**, D13 201, doi:10.1029/2010JD015237.

Kollias, P., J. Rémillard, W. Szyrmer, and E. Luke, 2011b: Cloud radar Doppler spectra in drizzling stratiform clouds: 2. Observations and microphysical modeling of drizzle evolution. *J. Geophys. Res.*, **116**, D13 203, doi:10.1029/2010JD015238.

Kollias, P., G. Tselioudis, and B. A. Albrecht, 2007c: Cloud climatology at the Southern Great Plains and the layer structure, drizzle, and atmospheric modes of continental stratus. *J. Geophys. Res.*, **112**, D09 116, doi:10.1029/2006JD007307.

Korolev, A. V. and I. P. Mazin, 2003: Supersaturation of water vapor in clouds. *J. Atmos. Sci.*, **60**, 2957–2974.

Krasnov, O. A. and H. W. J. Russchenberg, 2005: A synergetic radar-lidar technique for the LWC retrieval in water clouds: description and application to the Cloudnet data. *32nd Conference on Radar Meteorology*, Albuquerque, N. M., Amer. Meteor. Soc.

Kubar, T. L., D. L. Hartmann, and R. Wood, 2009: Understanding the importance of microphysics and macrophysics for warm rain in marine low clouds. Part I: Satellite observations. *J. Atmos. Sci.*, **66**, 2953–2972, doi:10.1175/2009JAS3071.1.

Kuo, H.-C. and W. H. Schubert, 1988: Stability of cloud-topped boundary layers. *Quart. J. Roy. Meteor. Soc.*, **114**, 887–916.

Laury-Micoulaut, C. A., 1976: The nth centred moment of a multiple convolution and its application to an intercloud gas model. *Astron. Astrophys.*, **51**, 343–346.

Lenschow, D. H., et al., 1988: Dynamics and Chemisty of Marine Stratocumulus (DYCOMS) Experiment. *Bull. Amer. Meteor. Soc.*, **69 (9)**, 1058–1067.

Lhermitte, R., 1990: Attenuation and scattering of millimeter wavelength radiation by clouds and precipitation. *J. Atmos. Oceanic Technol.*, **7**, 464–479.

Liljegren, J. C., 1994: Two-channel microwave radiometer for observations of total column precipitable water vapor and cloud liquid water path. *Fifth Symposium on Global Change Studies*, Nashville, TN, Amer. Meteor. Soc.

Liu, Y., B. Geerts, M. Miller, P. Daum, and R. McGraw, 2008: Threshold radar reflectivity for drizzling clouds. *Geophys. Res. Lett.*, **35**, L03 807, doi:10.1029/2007GL031201.

Liu, Y. and J. Hallett, 1998: On size distributions of cloud droplets growing by condensation: A new conceptual model. *J. Atmos. Sci.*, **55**, 527–536.

Liu, Z., et al., 2009: The CALIPSO lidar cloud and aerosol discrimination: Version 2 algorithm and initial assessment of performance. *J. Atmos. Oceanic Technol.*, **26**, 1198–1213, doi:10.1175/2009JTECHA1229.1.

Long, A. B., 1974: Solutions to the droplet collection equation for polynomial kernels. *J. Atmos. Sci.*, **31**, 1040–1052.

Lothon, M., D. H. Lenschow, D. Leon, and G. Vali, 2005: Turbulence measurements in marine stratocumulus with airborne Doppler radar. *Quart. J. Roy. Meteor. Soc.*, **131**, 2063–2080, doi:10.1256/qj.04.131.

Lu, M.-L., W. C. Conant, H. H. Jonsson, V. Varutbangkul, R. C. Flagan, and J. H. Seinfeld, 2007: The Marine Stratus/Stratocumulus Experiment (MASE): Aerosol-cloud relationships in marine stratocumulus. *J. Geophys. Res.*, **112**, D10 209, doi:10.1029/2006JD007985.

Lu, M.-L., A. Sorooshian, H. H. Jonsson, G. Feingold, R. C. Flagan, and J. H. Seinfeld, 2009: Marine stratocumulus aerosol-cloud relationships in the

MASE-II experiment: Precipitation susceptibility in eastern Pacific marine stratocumulus. *J. Geophys. Res.*, **114**, D24 203, doi:10.1029/2009JD012774.

Luke, E. and P. Kollias, 2012: Separating cloud and drizzle radar moments during precipitation onset using Doppler spectra. *J. Atmos. Oceanic Technol.*, in review.

Luke, E. P., P. Kollias, and M. D. Shupe, 2010: Detection of supercooled liquid in mixed-phase clouds using radar Doppler spectra. *J. Geophys. Res.*, **115**, D19 201, doi:10.1029/2009JD012884.

Mace, G. G. and K. Sassen, 2000: A constrained algorithm for retrieval of stratocumulus cloud properties using solar radiation, microwave radiometer, and millimeter cloud radar data. *J. Geophys. Res.*, **105 (D23)**, 29 099–29 108.

MacVean, M. K. and P. J. Mason, 1990: Cloud-top entrainment instability through small-scale mixing and its parameterization in numerical models. *J. Atmos. Sci.*, **47 (8)**, 1012–1030.

Markowicz, K. M., P. J. Flatau, A. E. Kardas, J. Remiszewska, K. Stelmaszczyk, and L. Woeste, 2008: Ceilometer retrieval of the boundary layer vertical aerosol extinction structure. *J. Atmos. Oceanic Technol.*, **25**, 928–944, doi:10.1175/2007JTECHA1016.1.

Martucci, G. and C. D. O'Dowd, 2011: Ground-based retrieval of continental and marine warm cloud microphysics. *Atmos. Meas. Tech.*, **4**, 2749–2765, doi:10.5194/amt-4-2749-2011.

Matrosov, S. Y., T. Uttal, and D. A. Hazen, 2004: Evaluation of radar reflectivity-based estimates of water content in stratiform marine clouds. *J. Appl. Meteor.*, **43**, 405–419.

McComiskey, A., G. Feingold, A. S. Frisch, D. D. Turner, M. A. Miller, J. C. Chiu, Q. Min, and J. A. Ogren, 2009: An assessment of aerosol-cloud interactions in marine stratus clouds based on surface remote sensing. *J. Geophys. Res.*, **114**, D09 203, doi:10.1029/2008JD011006.

Mead, J. B. and K. B. Widener, 2005: W-band ARM cloud radar. *32nd Int. Conf. on Radar Meteorology*, Albuquerque, N. M., Am. Meteorol. Soc., P1R.3, available online at `http://ams.confex.com/ams/pdfpapers/95978.pdf`.

Meneghini, R., 1978: Rain-rate estimates for an attenuating radar. *Radio Sci.*, **13 (3)**, 459–470, doi:10.1029/RS013i003p00459.

Miles, N. L., J. Verlinde, and E. E. Clothiaux, 2000: Cloud droplet size distributions in low-level stratiform clouds. *J. Atmos. Sci.*, **57**, 295–311.

Miller, M. A., M. P. Jensen, and E. E. Clothiaux, 1998: Diurnal cloud and thermodynamic variations in the stratocumulus transition regime: A case study using in situ and remote sensing. *J. Atmos. Sci.*, **55**, 2294–2310.

Münkel, C., N. Eresmaa, J. Räsänen, and A. Karppinen, 2007: Retrieval of mixing height and dust concentration with lidar ceilometer. *Bound.-Layer Meteor.*, **124**, 117–128, doi:10.1007/s10546-006-9103-3.

Nicholls, S., 1984: The dynamics of stratocumulus: aircraft observations and comparisons with a mixed layer model. *Quart. J. Roy. Meteor. Soc.*, **110**,

783–820.

Nicholls, S., 1989: The structure of radiatively driven convection in stratocumulus. *Quart. J. Roy. Meteor. Soc.*, **115**, 487–511.

Norris, J. R. and S. A. Klein, 2000: Low cloud type over the ocean from surface observations. part III: relationship to vertical motion and the regional surface synoptic environment. *J. Climate*, **13**, 245–256.

O'Connor, E. J., R. J. Hogan, and A. J. Illingworth, 2005: Retrieving stratocumulus drizzle parameters using Doppler radar and lidar. *J. Appl. Meteor.*, **44**, 14–27.

Ramanathan, V., R. D. Cess, E. F. Harrison, P. Minnis, B. R. Barkstrom, E. Ahmad, and D. Hartmann, 1989: Cloud-radiative forcing and climate: Results from the Earth Radiation Budget Experiment. *Science*, **243 (4887)**, 57–63.

Randall, D. A., J. A. Coakley, Jr., C. W. Fairall, R. A. Kropfli, and D. H. Lenschow, 1984: Outlook for research on subtropical marine stratiform clouds. *Bull. Amer. Meteor. Soc.*, **65 (12)**, 1290–1301.

Randall, D. A., Q. Shao, and C.-H. Moeng, 1992: A second-order bulk boundary-layer model. *J. Atmos. Sci.*, **49 (20)**, 1903–1923.

Rémillard, J., P. Kollias, E. Luke, and R. Wood, 2012a: Marine boundary layer cloud observations in the Azores. *J. Climate*, **25**, 7381–7398, doi:10.1175/JCLI-D-11-00610.1.

Rémillard, J., P. Kollias, and W. Szyrmer, 2012b: Radar-radiometer retrievals of number concentration and dispersion parameter in marine stratocumulus. *Atmos. Meas. Tech. Discuss.*, **5**, 7507–7533, doi:10.5194/amtd-5-7507-2012.

Rogers, R. R. and M. K. Yau, 1989: *A short course in cloud physics*, International Series in Natural Philosophy, Vol. 113. 3d ed., Butterworth Heinemann, Burlington, MA.

Rogers, R. R., I. I. Zawadzki, and E. E. Gossard, 1991: Variation with altitude of the drop-size distribution in steady light rain. *Quart. J. Roy. Meteor. Soc.*, **117**, 1341–1369.

Rozendaal, M. A., C. B. Leovy, and S. A. Klein, 1995: An observational study of diurnal variations of marine stratiform cloud. *J. Climate*, **8**, 1795–1809.

Saleeby, S. M. and W. R. Cotton, 2004: A large-droplet mode and prognostic number concentration of cloud droplets in the Colorado State University Regional Atmospheric Modeling System (RAMS). Part I: Module descriptions and supercell test simulations. *J. Appl. Meteorol.*, **43**, 182–195.

Sassen, K. and L. Liao, 1996: Estimation of cloud content by W-band radar. *J. Appl. Meteor.*, **35**, 932–938.

Sauvageot, H. and J. Omar, 1987: Radar reflectivity of cumulus clouds. *J. Atmos. Oceanic Technol.*, **4**, 264–272.

Serpetzoglou, E., B. A. Albrecht, P. Kollias, and C. W. Fairall, 2008: Boundary layer, cloud, and drizzle variability in the southeast Pacific stratocumulus regime. *J. Climate*, **21**, 6191–6214, doi:10.1175/2008JCLI2186.1.

Stevens, B., 2007: On the growth of layers of nonprecipitating cumulus convection. *J. Atmos. Sci.*, **64**, 2916–2931, doi:10.1175/JAS3983.1.

Stevens, B. and G. Feingold, 2009: Untangling aerosol effects on clouds and precipitation in a buffered system. *Nature*, **461 (7264)**, 607–613, doi:10.1038/nature08281.

Stevens, B., C.-H. Moeng, and P. P. Sullivan, 1999: Large-eddy simulations of radiatively driven convection: sensitivities to the representation of small scales. *J. Atmos. Sci.*, **56**, 3963–3984.

Stevens, B., et al., 2003: Dynamics and Chemisty of Marine Stratocumulus—DYCOMS-II. *Bull. Amer. Meteor. Soc.*, **84 (5)**, 579–593, doi:10.1175/BAMS-84-5-579.

Tampieri, F. and C. Tomasi, 1976: Size distribution models of fog and cloud droplets in terms of the modified gamma function. *Tellus A*, **28 (4)**, 333–347.

Turner, D. D., et al., 2007: Thin liquid water clouds: Their importance and our challenge. *Bull. Amer. Meteor. Soc.*, **88 (2)**, 177–190, doi:10.1175/BAMS-88-2-177.

Twomey, S., 1974: Pollution and the planetary albedo. *Atmos. Environ.*, **8**, 1251–1256.

Twomey, S., 1977: The influence of pollution on the shortwave albedo of clouds. *J. Atmos. Sci.*, **34**, 1149–1152.

Ulaby, F. T., R. K. Moore, and A. K. Fung, 1981: *Microwave remote sensing fundamentals and radiometry*, Vol. 1. Addison-Wesley, 456 pp.

vanZanten, M. C., B. Stevens, G. Vali, and D. H. Lenschow, 2005: Observations of drizzle in nocturnal marine stratocumulus. *J. Atmos. Sci.*, **62**, 88–106.

Wang, J. and B. Geerts, 2003: Identifying drizzle within marine stratus with W-band radar reflectivity. *Atmos. Res.*, **69**, 1–27, doi:10.1016/j.atmosres.2003.08.001.

Wang, J. and W. B. Rossow, 1995: Determination of cloud vertical structure from upper-air observations. *J. Appl. Meteor.*, **34**, 2243–2258.

Wood, R., 2000: Parameterization of the effect of drizzle upon the droplet effective radius in stratocumulus clouds. *Quart. J. Roy. Meteor. Soc.*, **126**, 3309–3324.

Wood, R., 2005a: Drizzle in stratiform boundary layer clouds. Part I: Vertical and horizontal structure. *J. Atmos. Sci.*, **62**, 3011–3033.

Wood, R., 2005b: Drizzle in stratiform boundary layer clouds. Part II: Microphysical aspects. *J. Atmos. Sci.*, **62**, 3034–3050.

Wood, R. and C. S. Bretherton, 2004: Boundary layer depth, entrainment, and decoupling in the cloud-capped subtropical and tropical marine boundary layer. *J. Climate*, **17**, 3576–3588.

Wood, R. and C. S. Bretherton, 2006: On the relationship between stratiform low cloud cover and lower-tropospheric stability. *J. Climate*, **19**, 6425–6432.

Wood, R., C. S. Bretherton, and D. L. Hartmann, 2002: Diurnal cycle of liquid water path over the subtropical and tropical oceans. *Geophys. Res. Lett.*, **29 (23)**, 2092, doi:10.1029/2002GL015371.

Wood, R. and D. L. Hartmann, 2006: Spatial variability of liquid water path in marine low cloud: The importance of mesoscale cellular convection. *J. Climate*, **19**, 1748–1764.

Wood, R., T. L. Kubar, and D. L. Hartmann, 2009: Understanding the importance of microphysics and macrophysics for warm rain in marine low clouds. Part II: Heuristic models of rain formation. *J. Atmos. Sci.*, **66**, 2973–2990, doi:10.1175/2009JAS3072.1.

Wood, R., et al., 2011: The VAMOS Ocean-Cloud-Atmosphere-Land Study Regional Experiment (VOCALS-REx): goals, platforms, and field operations. *Atmos. Chem. Phys.*, **11**, 627–654, doi:10.5194/acp-11-627-2011.

Xue, H., G. Feingold, and B. Stevens, 2008: Aerosol effects on clouds, precipitation, and the organization of shallow cumulus convection. *J. Atmos. Sci.*, **65**, 392–406, doi:10.1175/2007JAS2428.1.

Yamaguchi, T. and D. A. Randall, 2008: Large-eddy simulation of evaporatively driven entrainment in cloud-topped mixed layers. *J. Atmos. Sci.*, **65**, 1481–1504, doi:10.1175/2007JAS2438.1.

Yin, B. and B. A. Albrecht, 2000: Spatial variability of atmospheric boundary layer structure over the eastern equatorial Pacific. *J. Climate*, **13**, 1574–1592.

Yuter, S. E., Y. L. Serra, and R. A. Houze, Jr., 1999: The 1997 Pan American Climate Studies tropical eastern Pacific process study. Part II: Stratocumulus region. *Bull. Amer. Meteor. Soc.*, **81 (3)**, 483–490.

Zhang, G. J., A. M. Vogelmann, M. P. Jensen, W. D. Collins, and E. P. Luke, 2010: Relating satellite-observed cloud properties from MODIS to meteorological conditions for marine boundary layer clouds. *J. Climate*, **23**, 1374–1391, doi:10.1175/2009JCLI2897.1.

Zrnić, D. S., 1975: Simulation of weatherlike Doppler spectra and signals. *J. Appl. Meteorol.*, **14**, 619–620.

Zuidema, P., E. R. Westwater, C. Fairall, and D. Hazen, 2005: Ship-based liquid water path estimates in marine stratocumulus. *J. Geophys. Res.*, **110**, D20 206, doi:10.1029/2005JD005833.